OPTIMIZATION OF ZINC OXIDE BASED METAL - SEMICONDUCTOR JUNCTION INTERFACE PROPERTIES AND APPLICATIONS FOR OPTOELECTRONIC DEVICES

A Thesis Submitted to
the Graduate School of Engineering and Sciences of
İzmir Institute of Technology
in Partial Fulfillment of the Requirements for the Degree of

DOCTOR OF PHILOSOPHY

in Materials Science and Engineering

by
Abdurrahman Halis GÜZELAYDIN

January 2024
İZMİR

We approve the thesis of **Abdurrahman Halis GÜZELAYDIN**

Examining Committee Members:

Assoc. Prof Dr. Enver TARHAN
Department of Physics, İzmir Institute of Technology

Prof. Dr. Orhan ÖZTÜRK
Department of Physics, İzmir Institute of Technology

Assoc. Prof. Dr. Umut ADEM
Department of Materials Science and Engineering, İzmir Institute of Technology

Prof. Dr. Müslim Murat SAÇ
Institute of Nuclear Sciences, Ege University

Assist. Prof. Dr. Alper ÇETİNEL
Department of Physics, Ege University

17 January 2024

Assoc. Prof Dr. Enver TARHAN
Supervisor, Department of Physics,
İzmir Institute of Technology

Prof. Dr. Mustafa Muammer DEMİR
Co-Supervisor, Department of
Materials Science and Engineering,
İzmir Institute of Technology

Prof Dr. Yaşar AKDOĞAN
Head of the Department of
Materials Science and Engineering

Prof. Dr. Mehtap EANES
Dean of the Graduate School

ACKNOWLEDGEMENTS

I would like to express my gratitude to my advisor Assoc. Prof. Dr. Enver Tarhan for his invaluable encouragement, advice, guidance and patience throughout this study.

I would like to present my heartfelt thanks the thesis committee members for their devotion and participation during my thesis period.

I would also like to sincerely thank *all* of my countless friends for their encouragement, help and support along my journey.

I would like to thank Center for Materials Research staff at İzmir Institute of Technology for their help and support during the characterization part of my study.

I also would like thank all the clerks and staff across all departments for their invaluable help and support.

And last but not least, I am also grateful to my family for leading me to this stage and for their endless support throughout my life.

This thesis study was supported as part of Research University Support Programme project no. 2022İYTE-3-0023.

ABSTRACT

OPTIMIZATION OF ZINC OXIDE BASED METAL - SEMICONDUCTOR JUNCTION INTERFACE PROPERTIES AND APPLICATIONS FOR OPTOELECTRONIC DEVICES

This thesis manifests an experimental investigation on the optoelectronic characteristics of wide band gap thin film zinc oxide semiconductor – metal junction and performance enhancement of ultraviolet photo detectors fabricated utilizing this metal-semiconductor interface.

Pristine zinc oxide, aluminum doped zinc oxide and amorphous In-Ga-Zn-O thin film samples with thicknesses varying between 50-250 nm were fabricated from 2" ceramic targets via magnetron sputtering method. Surface properties and thus the zinc oxide – metal junction interface was optimized by altering sputtering parameters. Sputtering gas pressure, power and temperature was varied between 1.5 – 5 mTorr, 50 – 120 W and 25 – 500 °C, respectively. To determine the effects of energetic ion bombardment on the films' surface properties, biases ranging from 5 to 15 W were applied to the substrates during depositions. A 5 nm thick silicon dioxide passivation layer was deposited on zinc oxide thin films to suppress persistent photoconductivity effect. Furthermore, a thermal treatment under ultraviolet irradiation and was applied specifically to amorphous In-Ga-Zn-O thin films after device fabrication to improve their ultraviolet sensing capabilities.

Optoelectronic spectral responses of devices were assessed experimentally by using transient photocurrent spectroscopy method. An ultraviolet light source with a 275 nm peak wavelength at 500 µW power was used as illumination source. All devices exhibited photoconductor behavior with ohmic metal-semiconductor junctions under 5 V bias. Amorphous In-Ga-Zn-O Sample 10 attained a dark current of 140 nA and reached a photocurrent level of 3.8 µA with a photo-to-dark current ratio of 27, yielding a spectral response of 1830 A/W. The calculated external quantum efficiency for this device was 825000%.

ÖZET

ÇİNKO OKSİT TABANLI METAL – YARI İLETKEN KAVŞAK ARA YÜZEY ÖZELLİKLERİNİN ENİYİLENMESİ VE OPTOELEKTRONİK AYGIT UYGULAMALARI

Bu tez, geniş bant aralıklı ince film çinko oksit yarı iletken - metal birleşiminin optoelektronik özellikleri ve bu metal-yarı iletken ara yüzü kullanılarak üretilen ultraviyole foto dedektörlerin performansının artırılması üzerine deneysel bir araştırmayı ortaya koymaktadır.

Kalınlıkları 50-250 nm arasında değişen saf çinko oksit, alüminyum katkılı çinko oksit ve amorf In-Ga-Zn-O ince film örnekler, magnetron püskürtme yöntemiyle 2" seramik hedeflerden üretilmiştir. Yüzey özellikleri ve dolayısıyla çinko oksit - metal birleşim ara yüzeyi, püskürtme parametreleri değiştirilerek optimize edildi. Püskürtme gazı basıncı, gücü ve sıcaklığı sırasıyla 1,5 - 5 mTorr, 50 - 120 W ve 25 - 500 °C arasında değiştirildi. Enerjik iyon bombardımanının filmlerin yüzey özellikleri üzerindeki etkilerini belirlemek için, biriktirme sırasında alttaşlara 5 ila 20 W arasında değişen ön gerilim uygulanmıştır. Kalıcı fotoiletkenlik etkisini baskılamak için çinko oksit ince filmler üzerine 5 nm kalınlığında bir silikon dioksit pasivasyon tabakası biriktirilmiştir. Ayrıca, ultraviyole algılama yeteneklerini geliştirmek için cihaz üretiminden sonra amorf In-Ga-Zn-O ince filmlere özel olarak eşzamanlı ultraviyole ışıma altında termal işlem uygulanmıştır.

Cihazların optoelektronik spektral yanıtları, geçişli fotoakım spektroskopisi yöntemi kullanılarak deneysel olarak değerlendirilmiştir. Aydınlatma kaynağı olarak 500 µW gücünde 275 nm tepe dalga boyuna sahip bir ultraviyole ışık kaynağı kullanılmıştır. Tüm cihazlar 5 V öngerilim altında ohmik metal-yarı iletken bağlantıları ile fotoiletken davranışı sergilemiştir. Amorf In-Ga-Zn-O Örnek 8, 140 nA'lik bir karanlık akım değerinden 3,8 µA'lik bir foto-akım seviyesine ulaşarak, 27 katlık foto-karanlık akım oranıyla 1830 A/W'lık bir spektral yanıt vermiştir. Bu cihaz için hesaplanan harici kuantum verimliliği %825000'dir.

TABLE OF CONTENTS

LIST OF FIGURES

Figure **Page**

LIST OF TABLES

Table **Page**

CHAPTER 1

INTRODUCTION

Metal oxides are a major area of interest within the field of materials science with their metallic, semiconducting, insulating, ferromagnetic, ferroelectric, piezoelectric and superconducting behaviors. They are widely used as catalysts in chemical reactions, transparent and conducting layers in solar cells, electrolytes in batteries, active sensing layers in chemical or optical detectors, pigments in dyes, plastics, cosmetics, pharmaceuticals, and passivation layers in semiconductor manufacturing.

In thin film form, metal oxide are extensively used in surface processing (scratch-resistant, water-repellent coatings), bio-chemical sensors, and conductive, insulating or semiconducting layers for electronic and optoelectronic devices (Chen et al., 2009; Nistor et al., 2008; Znaidi et al., 2013).

Semiconductor metal oxide thin films are emerging as a key component of thin film transistor (TFT) devices with their wide band gaps and homo- or heterojunction structure forming abilities (Nomura et al., 2004; Kamiya et al., 2010). They can be deposited onto rigid and flexible substrates to fabricate solar cells, digital displays and light emitting diodes (LEDs) (Gautam et al., 2010; Eda et al., 2010). Due to their high refractive index values, these materials are utilized as reflective or anti-reflective coatings in optical applications. In an effort to increase the efficiency of solar cells, doped metal oxide semiconductor thin films are used as transparent and conducting window electrode layers (Muchuweni et al., 2017; Akazawa, 2009; pattini et al., 2015). Along with the widespread use of LEDs in lighting and flat panel display applications, they found new use cases and thus there has been a growing interest in research of metal oxides.

Semiconductor metal oxide thin films having band gaps higher than 3 eV are ideal candidates for fabricating ultraviolet (UV) photodetectors (Liu et al., 2010; Khokhra et al., 2011). Production of crystalline and bulk wide band gap semiconductors such as silicon carbide (SiC) and gallium nitride (GaN) involves complex crystal growth techniques that are not cost effective (Tekcan et al., 2014; Kim et al., 2011) . In addition to that, device manufacturing processes from those materials are also complex

and time consuming. Therefore, despite devices fabricated using these materials perform well, manufacturing costs prohibit widespread utilization of these products in civilian consumer products. Consequently, there is considerable interest in research and development of metal oxide thin films that are suitable for environmental pollution monitors, water sanitation, fire/flame sensors, personal wearable solar UV monitors where UV sensing is the prime requirement.

Zinc oxide (ZnO) is an "old" semiconductor that research has been carried out for a long time for its various application fields in science and industry. Piezoelectric transducers, optical waveguides, acousto-optic media, conductive gas sensors and transparent conductive electrodes are just a few examples for its broad application areas. It is a Group II-VI compound semiconductor with a wide, direct band gap of 3.36 eV at room temperature and an exciton binding energy of 60 meV. It crystallizes both in the hexagonal wurtzite and the cubic zinc-blende type structures. (Özgür et al., 2005)

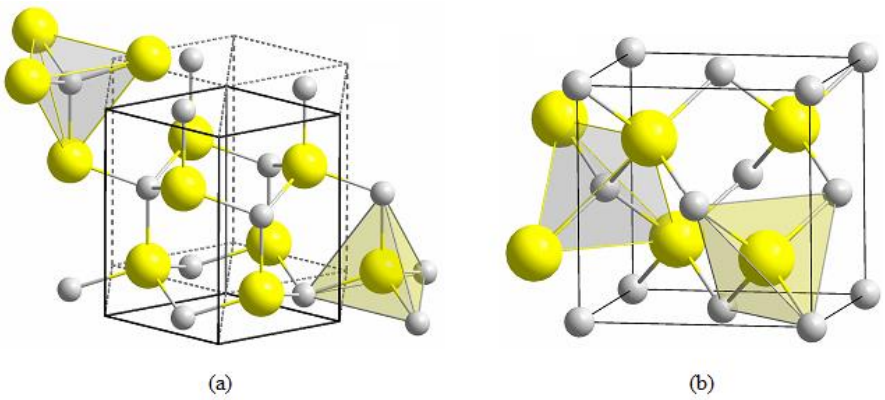

Figure 1.1. Hexagonal wurtzite (a) and cubic zinc-blende type structures of ZnO (Source: Özgür et al., 2005).

Table 1.1. Some important electronic parameters of ZnO (Source: Özgür et al., 2005).

Property	**Value**
Energy band gap	3.3 eV, direct
Intrinsic carrier concentration	$< 10^{-6}$ cm^{-3}
Exciton binding energy	60 meV
Electron effective mass	0.24
Electron Hall mobility	200 cm^2 V^{-1} s^{-1}
Hole effective mass	0.59
Hole Hall mobility	5-50 cm^2 V^{-1} s^{-1}

ZnO has recently been extensively investigated and shown great potential for UV photodetector applications because of its intrinsic properties such as a wide band gap, high UV absorption coefficient, and low cost. Therefore, ZnO thin films possess a considerable ability to be utilized in highly sensitive and fast response time UV sensors (Masuoka et al., 2006; Tian et al., 2014).

ZnO thin films can be successfully grown on solid substrates like glass, quartz and sapphire by various thin film deposition techniques such as RF magnetron sputtering (Doyan et al., 2017), pulsed laser deposition (PLD) (Ide et al., 2003; Rajendiran, 2014), and pulsed electron deposition (PED) (Yarmolich et al., 2011; Ali et al., 2016).

The surface and interface properties of ZnO are strongly dependent on the chemical structure defined by the adsorption of specific species on those sites. Physisorption and chemisorption reactions on ZnO surfaces influence the electronic behavior of ZnO due to formation of surface states inherent to the specific type of the adsorbed molecules (Schmidt et al., 2005). Here, a brief literature review will be presented addressing those phenomena and methods to overcome those issues in order to utilize ZnO in functional optoelectronic devices.

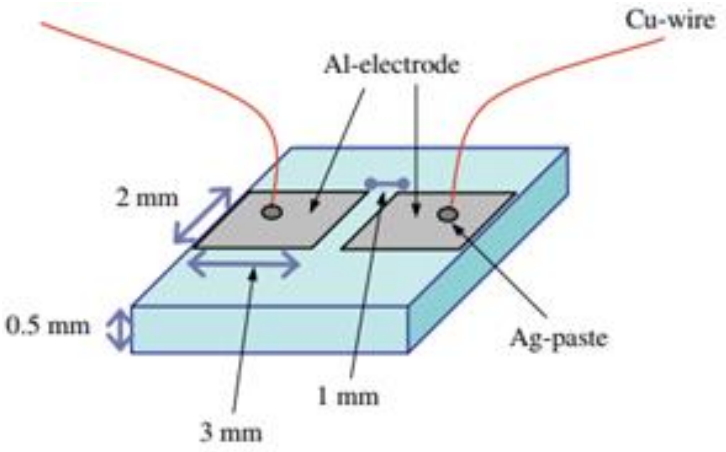

Figure 1.2. Al ohmic contacts on single crystal bulk ZnO (Source: Masuoka et al., 2006).

In a study (Masuoka et al., 2006) investigating the UV photo detection characteristics of ZnO, Al ohmic contacts were deposited on bulk ZnO single crystals and photoconductivity measurements were conducted.

It was found that the energy band structures and electronic states at the O and Zn surfaces of the ZnO single crystals were dramatically different and varied with the adsorbed species on these surfaces. Adsorbed molecules on the surfaces interact with the unbound electrons on the surface, resulting creation of new energy levels. Those levels were found to neutralize the photo generated electron-hole pairs at surface recombination centers, reducing the photocurrent intensity, thereby degrading the UV sensing performance of ZnO.

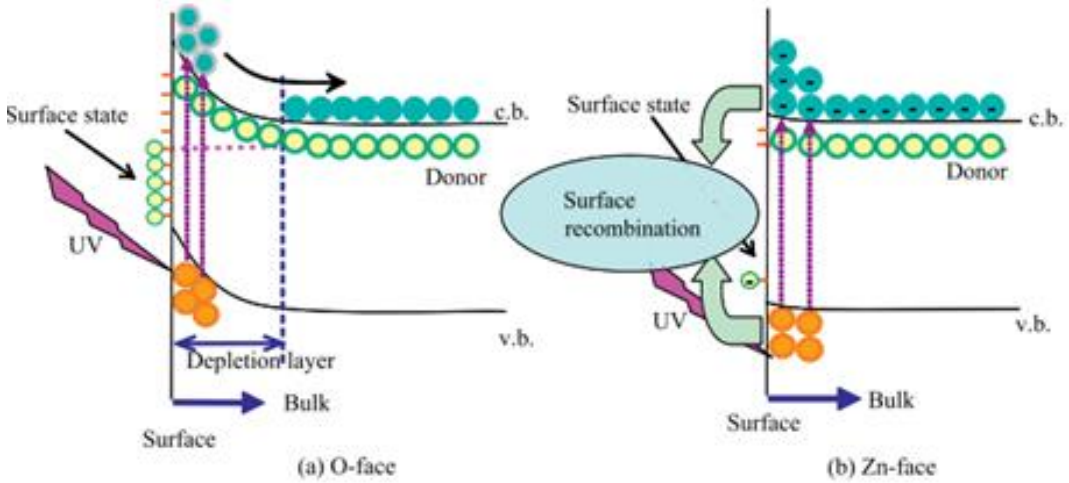

Figure 1.3. Energy band diagrams of (a) O and (b) Zn surfaces of bulk ZnO single crystal (Source: Zhou et al.; 2009).

In another study (Gautam et al., 2010), a hetero structure containing a ZnO-metal Schottky junction formed by ZnO nanowires was used to investigate the effects of surface functionalization on dark and photocurrent of the ZnO based photodetector. The study concluded that, surface functionalization to isolate the Schottky photodetector from ambient atmosphere caused improvement of the photodetector yield. This was tied to the effect of adsorbates on ZnO nanowires altering electronic properties of the surface. It was experimentally found that photo generated electron-hole pairs recombined at those surface states, hindering the photocurrent detection capabilities of the device. Figure 1.4 (b) and (c) clearly shows the reduction in relaxation times of unfunctionalized ZnO nanowire and functionalized ZnO nanowire by surface passivation.

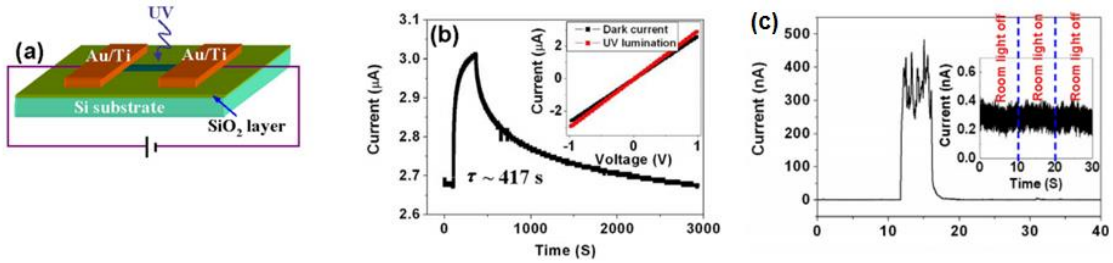

Figure 1.4. (a) Schematic view of the Schottky hetero structure with ZnO nanowire and gold electrodes. (b) Photocurrent-time plot of ZnO nanowires without surface functionalization. (c) Photocurrent-time plot of ZnO nanowires with surface functionalization (Source: Gautam et al., 2010).

A different study (Moazzami et al., 2006) investigated the time span required by ZnO thin-films to reach stable saturation with passivated and unpassivated surfaces under illumination. The findings were explained in terms of band-to-band transitions within the energy gap, electron and hole traps and recombination center models. The study concluded that adsorbates on the ZnO surface created new surface states affecting the photoconductivity values of the samples.

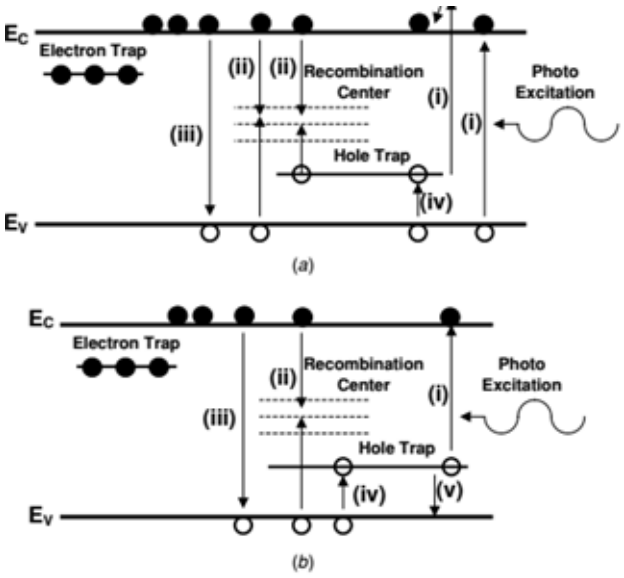

Figure 1.5. Band-to-band transition, electron and hole trap, recombination center models of transition resulting from adsorbed molecules on the surface (Source: Moazzami et al., 2006).

A study (Akazawa et al., 2009) investigating the effects of adsorbed layer on epitaxial ZnO film surface on photoconductivity revealed that, ZnO films treated with oxygen plasma in order to fill oxygen vacancies on the film surface showed an

experimentally observable improvement in photoconductivity. Experiments conducted in ambient atmosphere and under vacuum showed that oxygen plasma treatment caused changes in current-voltage (I-V) and photocurrent characteristics of the samples. Here, dark and photocurrent values of the samples decreased significantly and photocurrent transitions became much faster. This was explained as the limiting reaction being the slower sorption mechanism in contract to the faster electronic transition times.

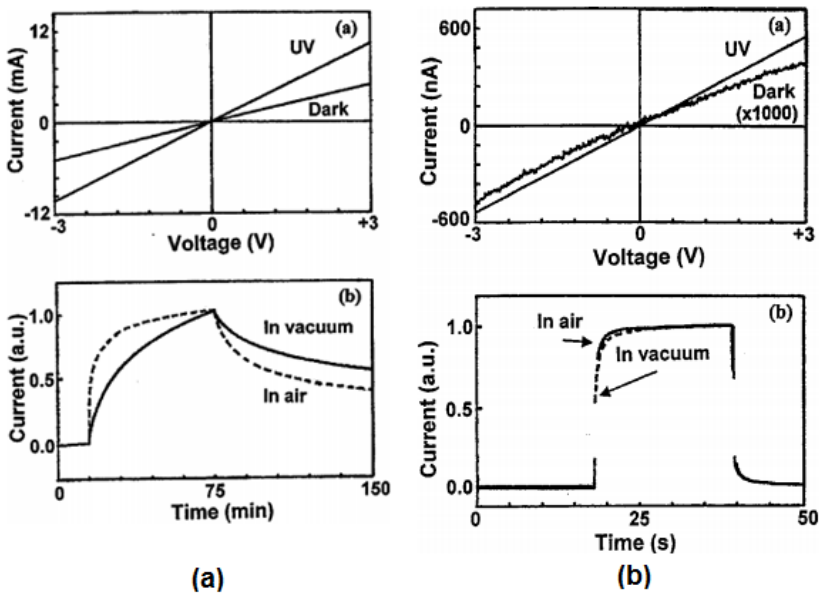

Figure 1.6. (a) I-V and photocurrent plots of epitaxial ZnO film with dangling bonds on its surface. (b) I-V and photocurrent plots of the same films after oxygen plasma treatment to fill the oxygen vacancies on the film surface (Source: Akazawa et al., 2009).

Lastly, in a study (Ali et al., 2016) investigating the insulating layer formed on copper doped ZnO sample during the transition from vacuum to ambient atmosphere and its impact on the electronic properties, the increase in surface resistivity of the sample throughout the transition was observed experimentally. Here, the study concludes that the more conductive ZnO surface under vacuum became more resistive because adsorbed molecules on the surface during exposure to ambient atmosphere trapped the unbound surface electrons, increasing the surface resistivity.

As it can clearly be seen from the literature studies; doped or undoped ZnO based materials which will be crafted for optoelectronic applications must be isolated from ambient atmosphere and kept away from common process chemicals such as

water, alcohol, acetone, photoresists etc., in order to have maximum attainable performance and stability.

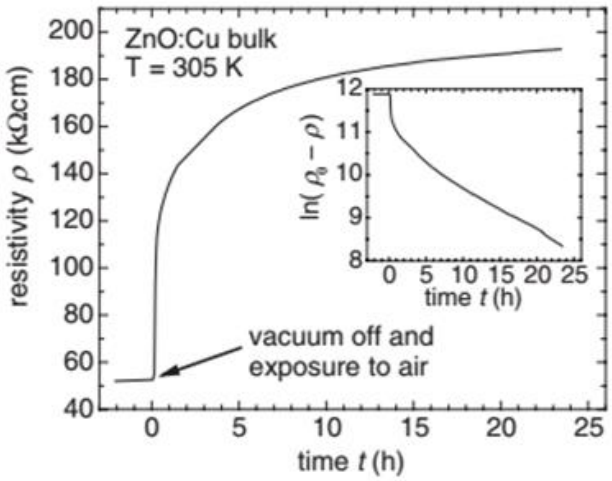

Figure 1.7. Increase in surface resistivity of ZnO sample during controlled exposure from vacuum to ambient atmosphere (Source: Ali et al., 2016).

CHAPTER 2

FOUNDATION

2.1. Metal/Semiconductor (MS) Junctions

When a metal with a workfunction Φ_M and Fermi energy E_{FM} contacts with an n-type semiconductor (with a workfunction Φ_S and electron affinity χ), whose Fermi level E_{FS} is closer to E_c in the band gap, free electrons in the conduction band of the semiconductor near the contact region move toward the metal side of the interface (due to lower Fermi level in the metal) causing a delta function-like negative charge distribution at the metal surface, while, the remaining positive charge distribution in the semiconductor near the interface, consisting entirely of immobile ionized donors, extends over a distance w inside the semiconductor creating the space charge (or depletion) region. Figure 2.1 depicts the idealized equilibrium band diagram for the MS junction.

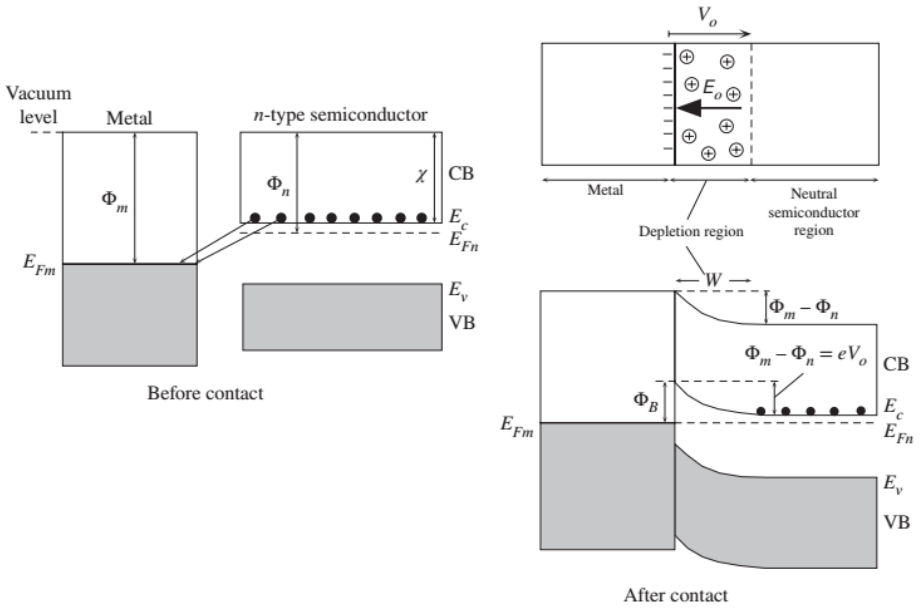

Figure 2.1. Representation of the electron energy band diagrams of a metal - n-type semiconductor junction according to the Schottky-Mott model (Source: Zhong et al., 2014)

The physical junction is set at x=0. Φ_B is the Schottky barrier height (SBH: the potential energy barrier for electrons) inhibiting the flow of electrons (black dots) from the metal to the semiconductor, while Φ_i is the potential energy barrier for the electron flow in the opposite direction. w is the extension of the depletion layer, and corresponds to the bent part of the energy bands.

A Schottky diode is formed at a metal-semiconductor junction and exhibits rectifier characteristics. This rectifier behavior stems from the electrostatic potential build-up at the junction interface between the metal and the semiconductor due to differences in the work functions of these two materials (Φ_M and Φ_S).

A photo detector requires a network of electrodes in its structure to harvest the photocurrent generated by the split charge carrier pairs. There is a variety of photo detector configurations. One of them is the metal-semiconductor-metal (MSM) photodiode which is comprised of two back-to-back Schottky diodes assembled together using an interdigitated electrode configuration on top of a photosensitive region. A schematic and SEM image of an MSM photodiode structure is shown in Figure 2.2.

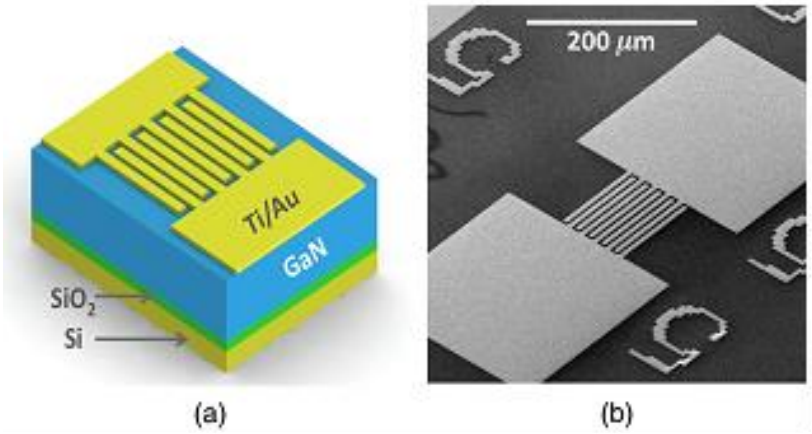

Figure 2.2. A schematic image of an MSM photodiode with a Ti-Au/GaN/Ti-Au configuration (a) and its SEM micrograph (b) (Source: Tekcan et al., 2014).

MSM photo detectors cannot operate at zero bias. They have low response times due to their low capacitance per unit area and are generally transport time limited, not RC time constant limited. By employing various lithography techniques, the electrode width and spacing can be adjusted with submicron precision which greatly shortens the response time improving the operational speed of such devices.

The biggest downside of MSM photo detectors is their intrinsic low responsivity. MSM detectors exhibit low photoresponsivity mainly due to the metallization for the electrodes blocks the active light collecting region by shadowing. But this shortcoming of the conventional MSM photo detector designs may be overcome by patterning the interdigitated electrodes that is used to harvest the photo-generated carriers at the bottom of the thin-film layer, thus taking advantage of the Schottky barrier formed at the interface of a metal and ZnO.

2.2. ZnO Thin Film Production Methods

ZnO thin films mostly suffer from poor crystal quality and various kinds of intrinsic defects, such as zinc interstices (Zn_i), zinc vacancies (V_{Zn}), oxygen interstices (O_i), and oxygen vacancies (V_o) which deteriorate the overall electrical and optical performance of the such films. Various growth techniques such as molecular beam epitaxy (MBE), metal-organic chemical vapor deposition (MOCVD), pulsed laser deposition (PLD), and physical vapor deposition (PVD) have been adopted to fabricate high quality ZnO thin films for use in a wide range of applications.

Magnetron sputtering has been proven to be a robust method for fabrication of high quality thin films, even for complex oxide materials. In this technique, a solid target material is bombarded with inert gas plasma ions (usually of argon) directed by electric and magnetic fields. The applied high voltage bias ionizes the inert gas at low pressures forming plasma. Whereas, the magnetic field accelerates electrons in plasma around spiral orbits increasing the collusion probability of electrons with the gas atoms in plasma, and thus increase the plasma yield. The gas ions gain high kinetic energies due to the electric field (from the applied high voltage) and are directed to a solid target and collide with it ejecting particles from the target surface. In this process, chemical bonds between the atoms of the solid target material are broken and the ejected species are composed of ions, molecules, neutral atoms and free radicals that belong to the target material. This complex “gas” of particles with varying velocity distribution expands out of the target surface. A portion of this gas is directed to a solid substrate positioned across the target on which it condenses forming a thin film.

Direct current (DC) plasma is adequate for sputtering from metallic targets. Because an electrically conducting metallic target can prevent positive charge build up

on the target and sustain DC plasma. But alternative current (AC) is needed for sputtering with dielectric targets such as ceramics. In insulating targets, positive charge builds up on the target and prevents Ar^+ ions from hitting the target. Therefore high DC voltages of the order of 10^{12} volts are required to sputter insulators. On the other hand, the RF plasma is mainly driven by ionization due to electrons which perform an oscillating motion in the plasma. At frequencies less than about 50 kHz, both electrons and ions in plasma are mobile and can follow the switching of the anode and cathode which results in basically DC sputtering of both surfaces. However, at frequencies above 50 kHz, heavier ions can no longer follow the switching and electrons can neutralize positive charge build up on the target. Furthermore, when electrons move back and forth in the plasma their probability of hitting Ar atoms and ionizing them increase. This kind of excitation is much more effective compared to the ionization by non-oscillating secondary electrons and leads to lower target voltages in an RF discharge. The low discharge voltages lead to significantly lower deposition rates for an RF magnetron discharge compared to a DC sputtering process under the condition of constant discharge power.

Figure 2.3 shows a simplified schematic drawing of a magnetron sputtering system.

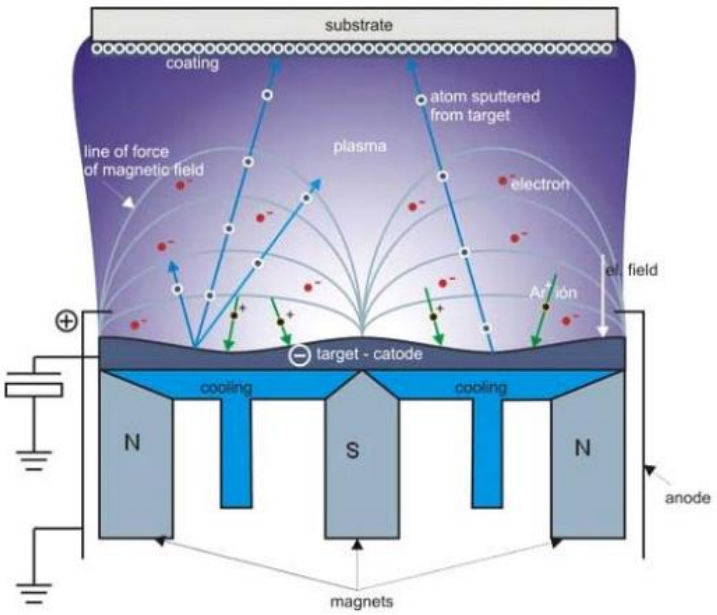

Figure 2.3. A schematic drawing of a magnetron sputtering system.

CHAPTER 3

EXPERIMENTAL METHODS

3.1. Materials and Method

3.1.1. Raw materials

Production of optoelectronic grade ZnO thin films require ultra-pure raw materials in bulk form. To meet this demand, 99,99% pure, 2” diameter, 0,250” thick ZnO target from CRM Co. (Figure 1.1) and a 99,99% pure, 2” diameter, 0,250” thick SiO_2 and Al_2O_3 targets from Kurt-Lesker Company were used for the deposition of intrinsic and Al-doped ZnO thin films and dielectric passivation/encapsulation layers to inhibit degradation of ZnO thin films in ambient atmosphere. (Figure 3.1)

Figure 3.1. New vacuum sealed Al_2O_3 target. The target is packed under argon gas atmosphere to eliminate and contamination during transport.

For use in high temperature thin film deposition conditions required for highly crystalline and textured ZnO thin films, 10 mm x 10 mm x 1 mm sized optical grade JGS1 standard quartz substrates were used from Haian Subei Optical Glass Company. (Figure 3.2)

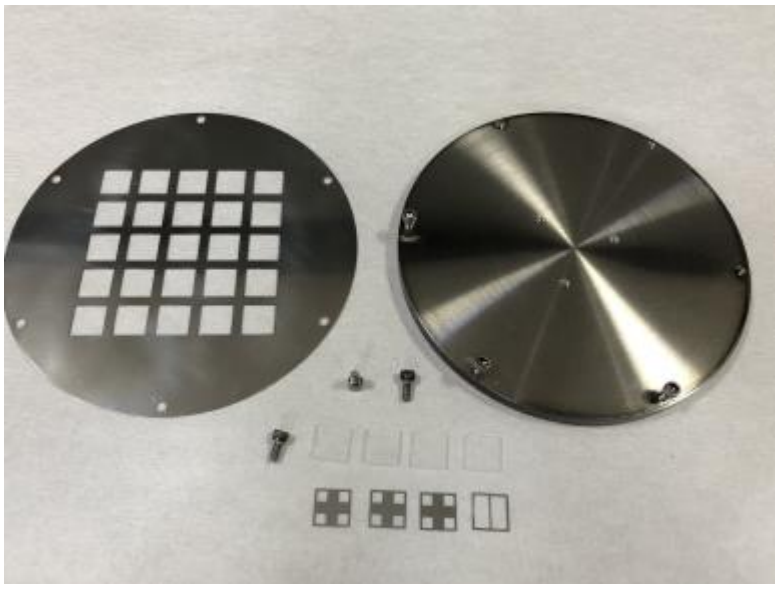

Figure 3.2. Quartz substrates next to sample holder plates and shadow masks for various metallization and thin film layers having different geometries.

3.1.2. Magnetron Sputtering System

ZnO and Al_2O_3 targets were installed on respective RF sputtering guns coupled with properly sized copper meshes. The copper meshes help protect the gun head and also improve thermal conductivity between the highly insulating oxide targets and the gun head improving cooling efficiency and preventing thermal cracking. (Figure 3.3)

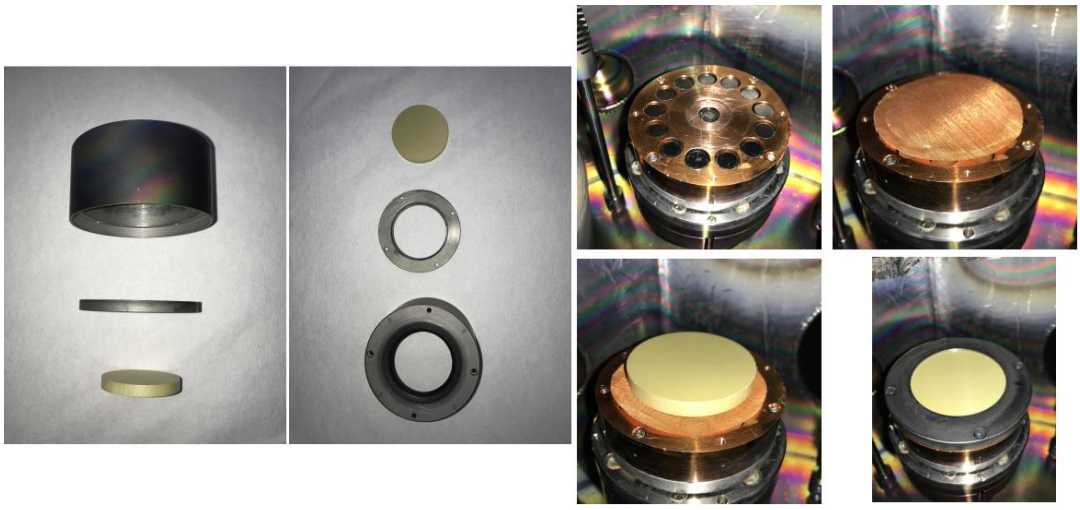

Figure 3.3. Step-by-step installation of ZnO target. Copper mesh is laid onto the gun head and aligned. Then ZnO target was laid. Finally, the target is fixed by the retention ring.

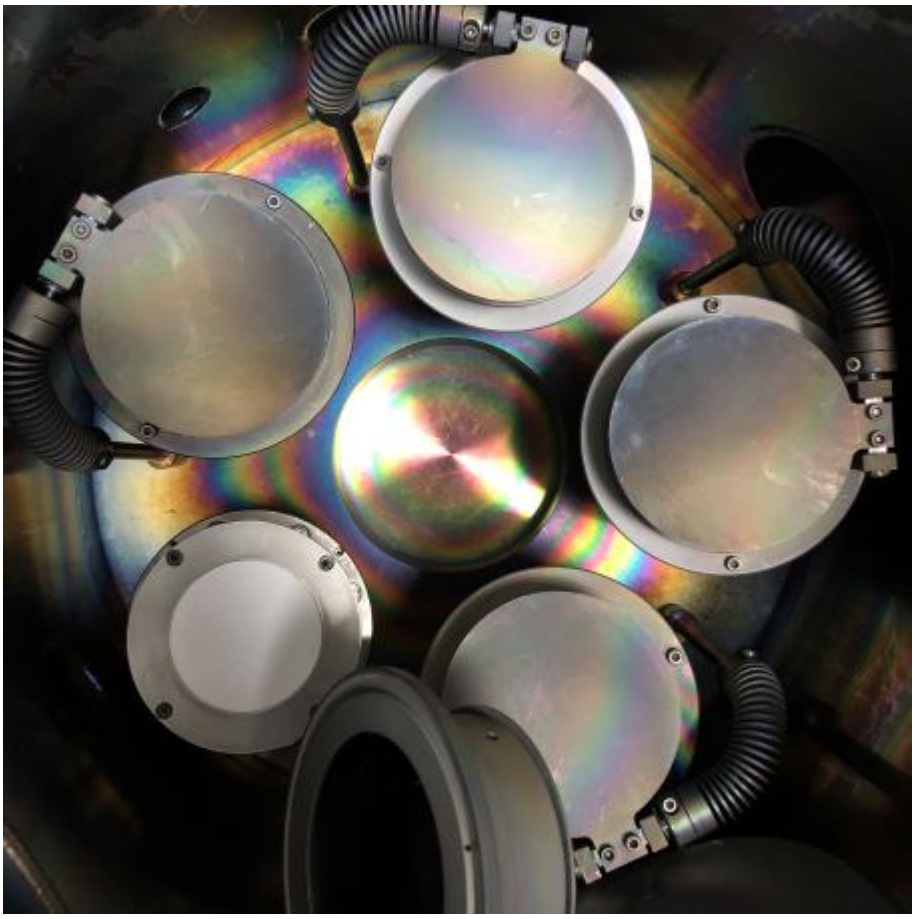

Figure 3.4. Top view of the main vacuum chamber. Scaffolds on the chamber walls and other components were properly cleaned to sustain an ultra-high vacuum environment.

One very important aspect of new target installation is the size of gap between anode and cathode. The manufacturer suggests 0,7 to 1 mm gap spacing at pressures under 10 mTorr. So the gap spacing must be adjusted very precisely. In addition to this, there must be no electrical contact between anode and cathode so that no short circuit occurs. Otherwise, it causes sparking or plasma ignition problems. (Figure 3.5)

Standard 10 mm x 10 mm square sample geometry is adopted at each step of production, assembly and characterization within the scope of this study for simplicity and flexibility reasons. So, a suitable sample holder became necessary to accommodate multiple samples and shadow masks in each production run simultaneously. To fulfill this demand, we designed and manufactured a centrally positioned 5 x 5 grid of square patterns coaxial with the 4” substrate holder plate which is capable of holding up to 25 quartz substrates at the same time. The grid was precisely machined onto a 2 mm thick SAE 304 stainless steel sheet via CNC milling. The holder can withstand temperatures

of up to 600 °C and it is chemically oxidation resistant at those temperatures, enabling thin film production processes at extreme conditions. (Figure 3.6)

Figure 3.5. After precise adjustment of cathode-anode shield gap, a short circuit check was done via a digital multimeter to confirm there is no conduction between the two pieces and the gap is totally insulating.

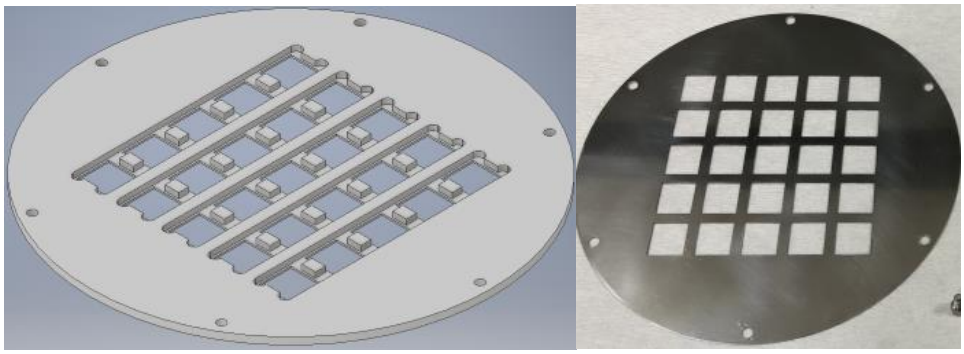

Figure 3.6. CAD design of the new substrate holder (left) and manufactured substrate holder (right).

3.2. ZnO Thin film Production Parameters and Method

In order to determine one of the crucial production parameters, such as sputtering power, plasma gas pressure and deposition rate, two initial production runs were made. Sputtering power was selected as the control variable. Intrinsic ZnO thin films were deposited at 50 W and 100 W RF powers for 100 minutes both. Parameters other than sputtering power, such as argon gas flow rate and pressure, target-substrate distance, substrate rotation speed and substrate temperature were kept constant in order to see the effects of sputtering power on deposition rate and thin film structure. Table 3.1 shows a comparative view of production parameters of the two samples.

Table 3.1. Comparative list of production parameters of the two intrinsic ZnO thin films

Sample Name	Sputtering Power	Ar Flow Rate	Ar Pressure	Working Distance	Rotation Speed	Substrate Temperature
BZO 1	**50 W**	10 SCCM	4,7 mTorr	10 cm	8 rpm	RT
BZO 2	**100 W**	10 SCCM	4,7 mTorr	10 cm	8 rpm	RT

3.3. Structural Characterization

Structural SEM, EDX, XRD and AFM analysis were made to determine fabricated thin films' surface morphology, chemical composition, crystal structure, surface topography and thickness properties at two different RF power levels, respectively.

3.3.1. Crystal Structure

Crystallinity, degree of crystallization and crystallite size of the thin films were evaluated by XRD. The instrument had a characteristic Cu Kα X-ray radiation source with a wavelength of $\lambda = 1.5444$ Å.

It is well known that the (0002) orientation of wurtzite ZnO structure is generally observed, implying that the surface free energy of (0002) plane is the lowest while forming ZnO thin films via magnetron sputtering technique. This results in the

favored formation of (0002) oriented texture in ZnO thin films which have a c-axis preferred crystal orientation on the (0002) plane, along the c-axis orthogonal to the substrate surface.

3.3.2. Surface Topography and Thickness

Topographic features of film surfaces were mapped and thicknesses of the thin films were measured via AFM.

3.3.3. Preparation of Gold and Aluminum Metallic Electrodes

Stainless steel shadow masks were used to pattern 2-point and 4-point contact metallic electrodes onto quartz substrates. (Figure 3.7)

Aluminum was used to obtain ohmic contacts with ZnO thin films, whereas gold was used to obtain Schottky type contacts. Gold was chosen because it yields the highest known value for the barrier height between ZnO and a metal (0.7 eV).

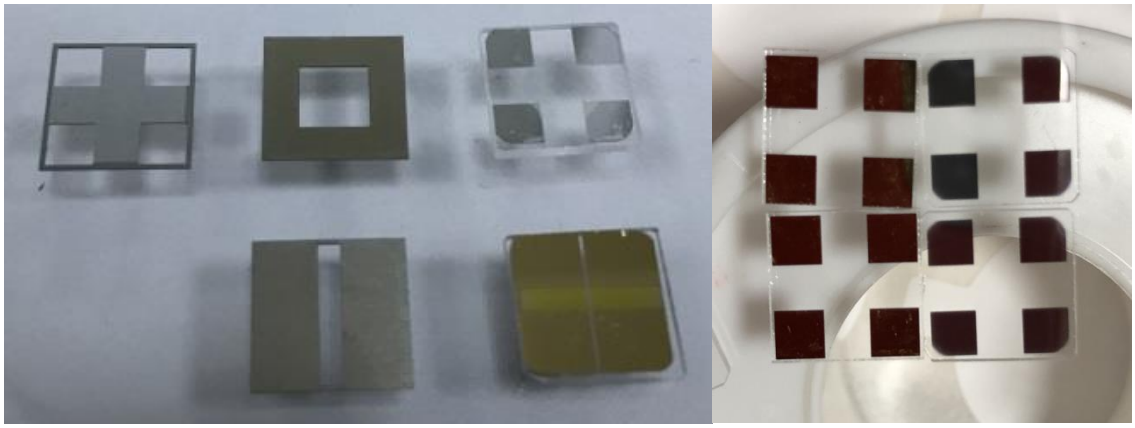

Figure 3.7. Shadow masks and electrode coated substrates designed for device fabrication and electrical measurements.

Aluminum metallization was made via DC sputtering from a metallic aluminum target, whereas gold was made via thermal evaporation.

3.4. Doped ZnO Thin film Production Parameters

Intrinsic and Al-doped ZnO thin films were fabricated on quartz substrates with the magnetron sputtering deposition parameters given in Table 3.2.

Table 3.2. Sputtering parameters for undoped and Al-doped ZnO thin films.

Sample Name	Sputtering Power	Ar Flow Rate	Ar Pressure	Working Distance	Rotation Speed	Substrate Temperature
ZNO-1	**100 W**	10 SCCM	4,7 mTorr	10 cm	10 RPM	RT
ZNO-2	**100 W**	10 SCCM	4,7 mTorr	10 cm	10 RPM	200
AZO-1	**100 W**	10 SCCM	4,7 mTorr	10 cm	10 RPM	RT
AZO-2	**100 W**	10 SCCM	4,7 mTorr	10 cm	10 RPM	RT
AZO-3	**100 W**	10 SCCM	4,7 mTorr	10 cm	10 RPM	200
AZO-4	**100 W**	10 SCCM	4,7 mTorr	10 cm	10 RPM	200
AZO-5	**100 W**	10 SCCM	4,7 mTorr	10 cm	10 RPM	200

Both undoped and Al-doped ZnO films were fabricated in 100% Ar gas plasma composition at room temperature and 200 °C for 100 min. Sputtering power was kept constant at 100 W determined from prior parameter optimization studies.

Blank, gold and aluminum electrode coated substrates were used in order to make 4-probe measurements with the devices to determine ZnO thin films' electronic characteristics.

Al doping was made in two different ways. First, the Al source DC target shutter was fully open during the 100 min deposition period. The DC power was set to 2.5 W, which is the lowest power value attainable. During other depositions, shutter intervals were used to modulate Al-doping levels in ZnO thin films.

For RT Al-doped AZO-1 and AZO-2 ZnO thin film sample depositions, fully open shutter and 50% shutter interval in 5 min period was used, respectively.

For 200 °C Al-doped AZO-3, AZO-4 and AZO-5 ZnO thin film sample depositions, fully open shutter, 50% and 20 % shutter intervals in 5 min period was used.

3.4.1. 4-Point Probe van der Pauw Measurements

A probe station setup shown in Figure 3.8 with 4-point van der Pauw configuration was used for electronic measurements to determine sheet resistance, carrier concentration and Hall mobility of intrinsic and Al-doped ZnO thin film samples.

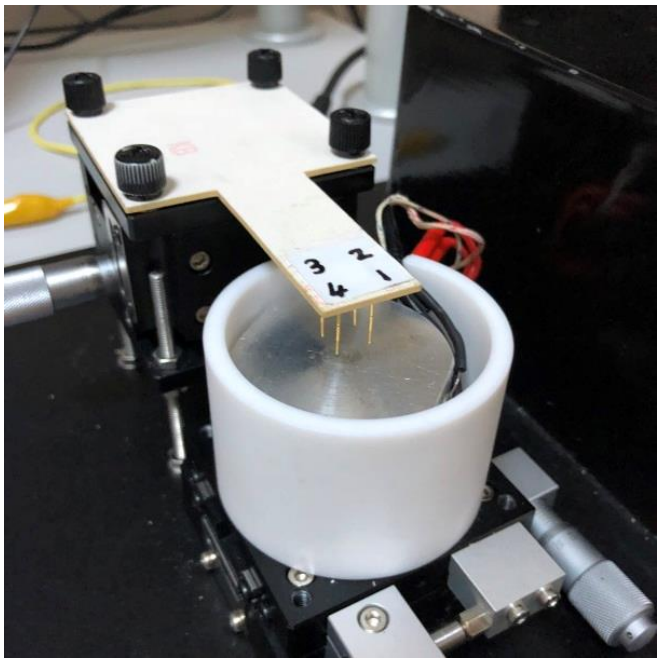

Figure 3.8. Probe station setup for 4-point van der Pauw measurements to determine sheet resistance, carrier concentration and Hall mobility.

In order to determine the metal – semiconductor junctions' electronic properties, and especially the contact type which is of prime interest in this study, I-V measurements were made. Those measurements revealed ohmic contacts for all samples with both gold and aluminum contact electrodes.

All I-V scans were made under 5 V bias potential to protect thin film samples from overheating and thermal damage.

3.5. Optical and Structural Characterizations

A set of six different undoped ZnO thin films was fabricated with varied deposition parameters given in Table 3.3.

These parameters were specifically selected to understand the effects and correlation of sputtering gas composition and substrate temperature with optical and structural characteristics of the fabricated ZnO thin films.

Table 3.3. Deposition parameters of ZnO thin films for "bottom-up" route.

Sample Name	Substrate Temperature (°C)	Flow Rate (SCCM)	Pressure (mTorr)	Sputtering Power (W)	Rotation Speed (RPM)	Working Distance (cm)
UZO-1	RT	Ar–10	4.7	100	10	10
UZO-2	RT	Ar–8 O_2–2	5.2	100	10	10
UZO-3	200	Ar–8 O_2–2	5.2	100	10	10
UZO-4	200	Ar–10	4.7	100	10	10
UZO-5	400	Ar–8 O_2–2	5.3	100	10	10
UZO-6	400	Ar–10	4.7	100	10	10

Table 3.4. Comparison matrix of 2 fundamental deposition parameters, temperature and sputtering gas composition for the undoped ZnO thin film samples.

SCCM	**RT**	**200 °C**	**400 °C**
Ar–10	***UZO-01***	***UZO-04***	***UZO-06***
Ar–8 O_2–2	***UZO-02***	***UZO-03***	***UZO-05***

Within the six sample set, two gas composition and three temperature values were selected as control variables where others kept constant as presented in the simple parameter matrix given in Table 3.4.

An extensive set of optical and structural characterizations were made for the undoped ZnO thin film samples fabricated with deposition parameters listed in Table

3.3 to determine their basic crystalline and defect structures and their correlation with those production parameters.

3.5.1. UV–Vis Spectroscopy

Transmission spectra of the fabricated undoped ZnO thin films were taken by a Perkin Elmer Lambda 950 UV–Vis/NIR Spectrometer between 200–800 nm wavelengths. Background correction was performed by taking air as the baseline for transmission measurements.

3.5.2. Photoluminescence Spectroscopy

Photoluminescence spectra of the fabricated undoped ZnO thin films were taken by a Perkin Elmer LS 55 Luminescence Spectrometer at an excitation wavelength of 365 nm with both 10 nm excitation and emission slit widths at room temperature.

3.5.3. High Resolution XRD

High resolution XRD patterns of the fabricated undoped ZnO thin films were taken by a Philips PANanalytical X'Pert x-ray diffractometer. The instrument had a characteristic Cu Kα X-ray radiation source with a wavelength of $\lambda = 1.5444$ Å.

Crystallinity, crystallite size, and lattice strain of the fabricated ZnO thin films were evaluated from $\theta-2\theta$ gonio and rocking curve scan data.

3.6. I-V and Transient Photocurrent Spectroscopy Measurements

I-V and TPS measurements of a select ZnO thin film sample assembled onto chip carrier were conducted. The measured device junctions showed ohmic characteristics as a result of the polycrystalline structure of the fabricated ZnO thin films.

Measurement results and their correlation with device behavior will be further discussed in detail.

3.6.1. Chip Carrier Assembly

Specially designed chip carrier units were used to construct the measurement devices by bonding ZnO thin film substrates onto them which can fit into a vacuum cryostat unit for I-V and TPS measurements. The chip carrier unit is comprised of a PCB with 4-wire connector pins bonded to a copper back plate. The ZnO thin films fabricated on quartz substrates were then assembled onto these chip carrier units with silver paste. 80 µm thick epoxy insulated wires bonded with indium metal were used for contact connections on the gold electrodes and the chip carrier pins. (Figure 3.9)

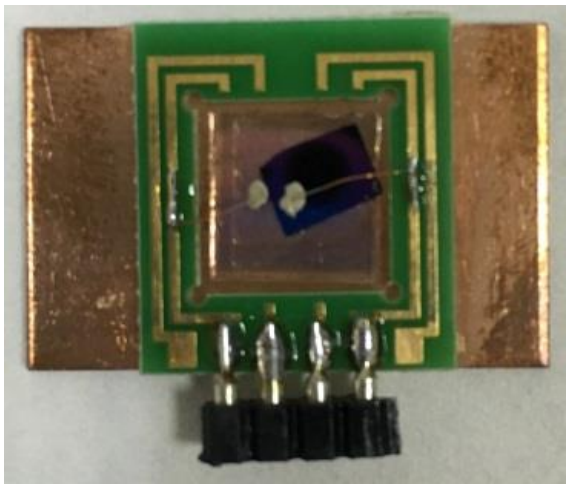

Figure 3.9. A device assembly on a chip carrier along with a ZnO thin film substrate bonded on it for electrical measurements.

CHAPTER 4

AMORPHOUS OXIDE SEMICONDUCTORS AND AMORPHOUS IGZO SYSTEM

In 1996, Hosono et al. published a paper putting forward a working hypothesis to explore novel wide bandgap electrically conducting amorphous oxides (Hosono et al., 1996). In this study he pointed out advantages of amorphous oxide semiconductors (AOSs) for TCO applications. Until then, the electrical performance of amorphous materials was thought to be inherently poor.

4.1. Inception of AOSs

Before the first AOS was proposed in 1996, it was believed that amorphous semiconductors have very low mobilities << 1 $cm^2\ V^{-1}s^{-1}$, as seen in a-Si:H and amorphous chalcogenides. Hosono et al. indicated that electronic transport in an AOS is distinctly different from that of silicon or of a similar covalent semiconductor because a covalent material has strongly-directed sp^3 bonds, in contrast to an AOS with post-transition metal cations whose conduction band minima are derived from isotropic and spatially expanded 4*s*, 5*s*, or 6*s* atomic states. In certain oxide materials containing p-block metal cations, the vacant metal s-orbital that predominantly makes up the conduction band minimum is spherical and spatially spread, making their overlap insensitive to bonding angle variation. (Figure 4.1) Thus, this difference in bonding leads to better electronic transport, with AOSs possessing mobilities in excess of 10 $cm^2\ V^{-1}s^{-1}$ compared to ~ 1 $cm^2\ V^{-1}s^{-1}$ for a-Si. The AOS concept proposed indicated that amorphous oxides composed of heavy metal cations (HMC) with electronic configurations $(n-1)d^{10}\ ns^0$ ($n \geq 4$) are promising candidates for high-mobility amorphous semiconductors because the lowest unoccupied states (conduction band minimum, CBM) is composed mainly of largely spread spherical metal ns^0 orbitals and is expected to have a small electron effective mass and a high electron mobility even in amorphous disordered structures. The first demonstrations of AOS were H^+-implanted

Cd_2GeO_4, $AgSbO_3$, and Cd_2PbO_4 that showed high electron mobilities for amorphous materials around 5–12 $cm^2 V^{-1}s^{-1}$.

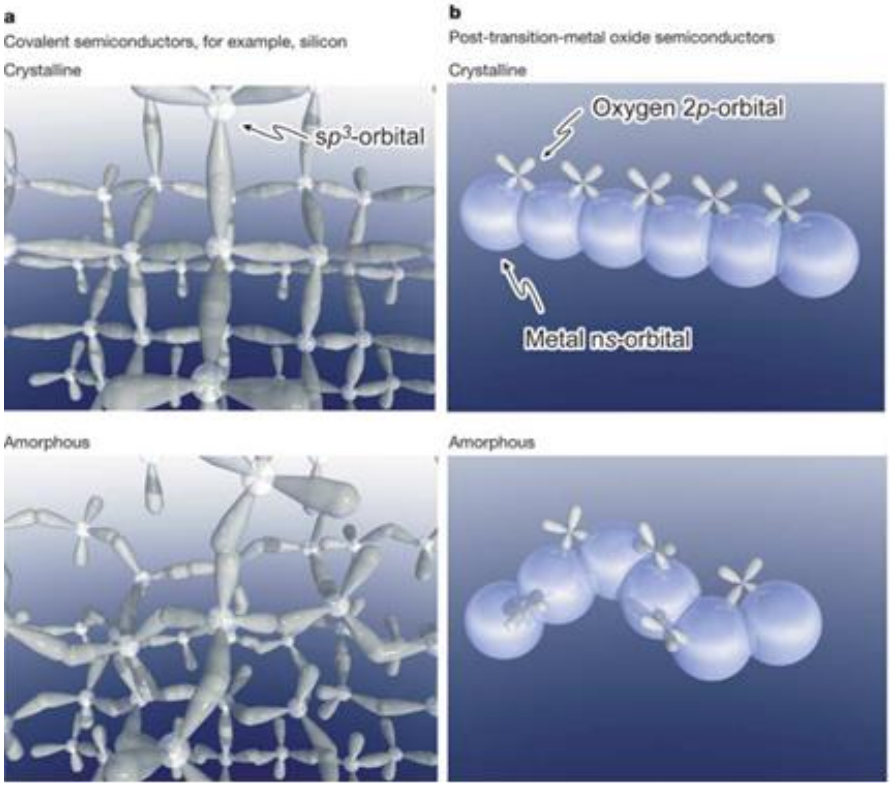

Figure 4.1. Schematic orbital drawings for the carrier transport paths (which are conduction band bottoms) in crystalline and amorphous semiconductors (Source: Nomura et al., 2004).

Thereafter, high mobility, heavily doped a-IGZO thin films were reported in 2000. Then, a-IGZO was came forward as a channel material for TFTs because it does not contain toxic elements (such as Cd, Sb, and Pb) and does not require H^+-implantation to increase its free electron density, N_e. By reducing N_e and defect density in a-IGZO thin films, the first AOS TFTs was reported in 2004 with good operating characteristics that can even be fabricated by a room temperature process on flexible PET sheets. An additional advantage of AOSs was their oxide nature, leading to air processability and thermodynamic stability (Nomura et al., 2004).

AOSs have attracted significant attention in optoelectonic industries and the academia. This is due to its favorable features such as high mobility, high uniformity, low process temperature, a wide flexibility of chemical composition, good controllability of carrier density, and transparency.

4.2. Multicomponent a-IGZO Properties and Advantages

Several aspects of a-IGZO are of general interest in the context of this study, as well as a specific interest to this material system as a high performance semiconducting active layer for optoelectronic applications.

First, concerning the multicomponent oxides, as-deposited IGZO films are found to be amorphous regardless of their composition, exhibiting only a broad peak centered at $2\theta \approx 32–34°$, typical of amorphous films as seen in Figure 4.2. By Scherrer analysis on this broad peak, possible crystallite sizes have only been around 2 nm, which is consistent with the values typically reported in the literature for multicomponent oxides, validating their designation as amorphous materials. This makes it possible to use magnetron sputtering method for large-area uniform deposition of a-IGZO thin films. Also, it is reported that the amorphous phase of IGZO is thermally stable in air up to ~ 500 ºC (Kamiya et al., 2010). This is important from a material/device stability point-of-view and also from the perspective of appreciating the value of an amorphous material and recognizing that many materials, e.g. ZnO, cannot be prepared as an amorphous phase.

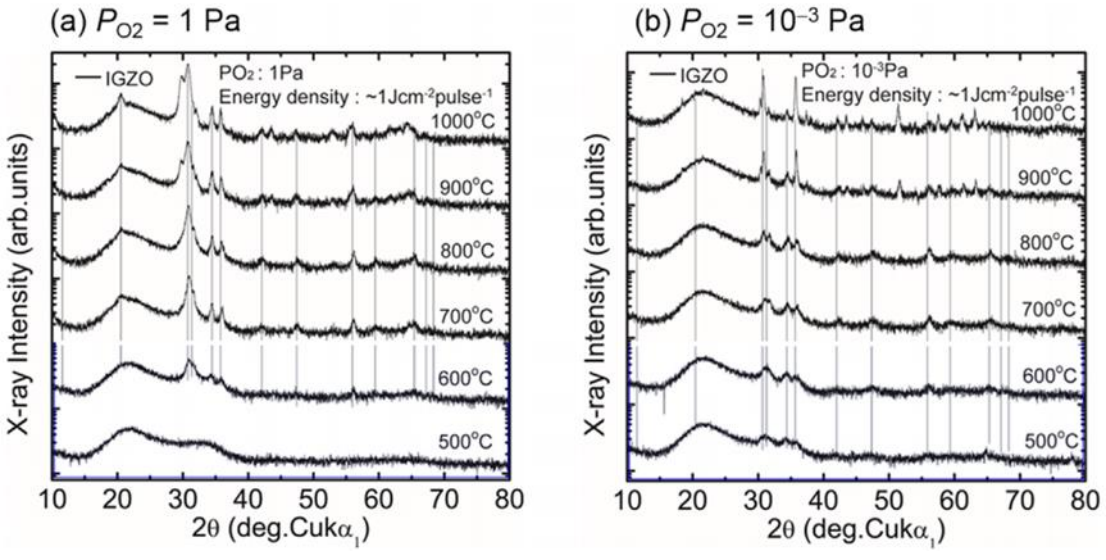

Figure 4.2. Crystallization behaviors as a function of annealing temperature for a-IGZO films deposited at (a) P_{O2} = 1 and (b) 10^{-3} Pa (Source: Kamiya et al., 2010).

The Hall mobility of a-IGZO increases with increasing carrier concentration. This trend is at first puzzling, since a higher doping concentration implies increased ionized impurity scattering which would lead to a decrease in the mobility.

However, this increasing mobility at higher doping concentration trend which is observed for a-IGZO is well known for polycrystalline semiconductors. It is attributed to a rise in the Fermi level position with increasing doping concentration. This result in a reduction in the potential barrier seen by conduction band electrons due to grain boundaries, which are modeled as back-to-back Schottky barriers depicted schematically in Figure 4.3.

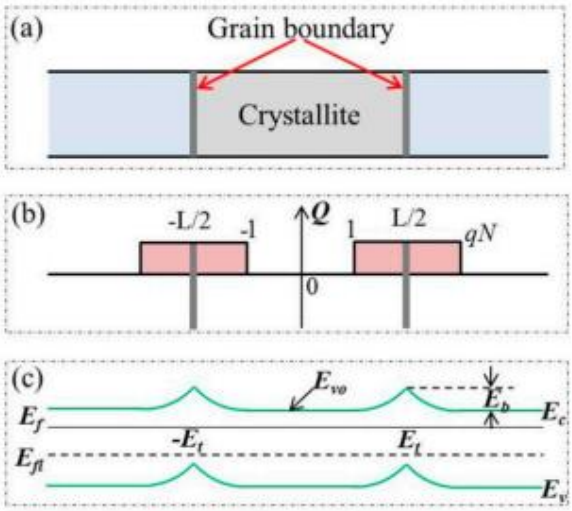

Figure 4.3. Schematic diagram of (a) crystal structure; (b) charge distribution; and (c) energy band structure of polycrystalline films (Source: McCluskey et al., 2009).

Remarkably, single crystal IGZO also exhibits this same tendency in which the mobility increases with increasing doping concentration. Nomura et al. explain this single crystal trend using a percolation conduction model in which the potential barriers impeding electron transport are not attributed to grain boundaries but, rather, are ascribed to conduction band edge barriers associated with the random distribution of Ga^{+3} and Zn^{+2} ions in the crystal since that a single crystal $InGaO_3(ZnO)_5$ lattice is envisaged as consisting of alternating stacked layers of InO_2^- and $GaO(ZnO)^{5+}$ blocks. (Figure 4.4)

In an analogous fashion, the observed a-IGZO trend in which the mobility increases with increasing doping concentration in an amorphous material is accredited

to a percolation conduction model in which tail state potential barriers arise from the random amorphous bonding structure. It is likely that this mobility versus carrier concentration trend has device consequences which have not yet been fully appreciated.

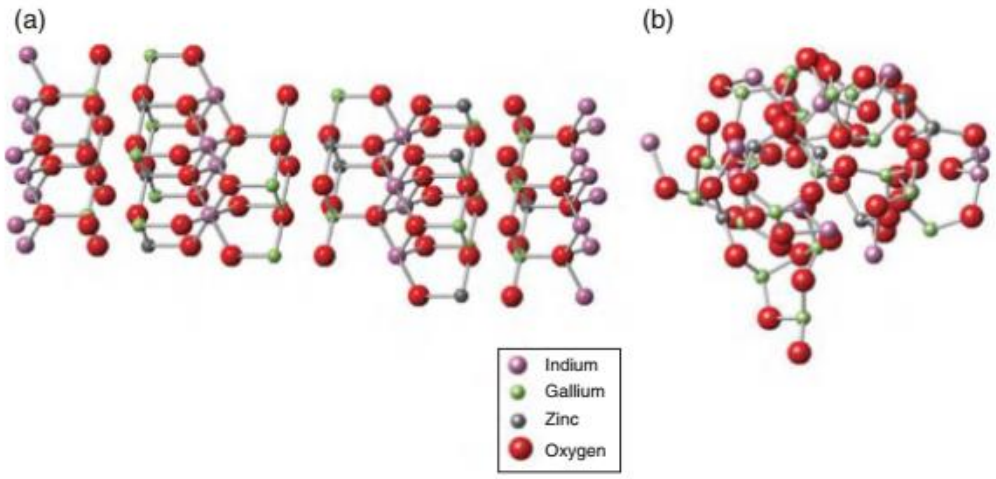

Figure 4.4. Schematic structures of (a) crystalline and (b) amorphous IGZO (Source: Nomura et al., 2004).

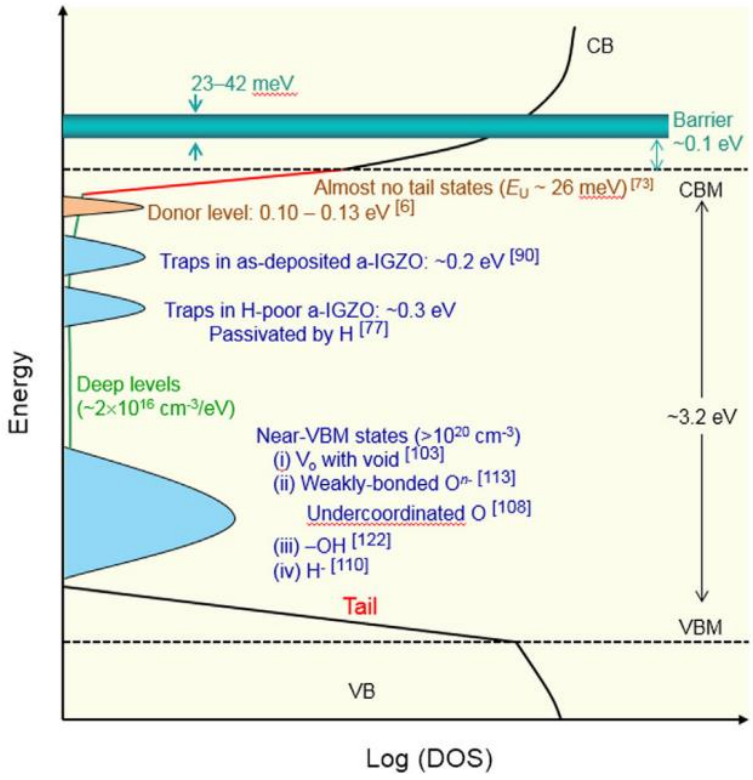

Figure 4.5. Known electronic structure of a-IGZO with subgap defects (Source: Moazzami, et al., 2006).

It is well worth to underscore the importance of choosing a semiconductor material in which the carrier concentration can be reduced to a very low level, down to < ~10^{14} cm^{-3}, in order to achieve fine control of subsequent junction formation with metals. With this objective in mind, the incorporation of Ga ions into a-IGZO is crucially important since this leads to a suppression of oxygen vacancies and serves as a stabilizer due to the formation of stronger Ga-O bonds than InO and Zn-O bonds. It also improves in films' insulation properties by widening bandgap E_g. (Table 4.1) This is a very important aspect of a-IGZO system to overcome the problems associated with ZnO until now.

Table 4.1. Band parameters of a-IGZO thin films with various compositions (Source Ide et al., 2019).

	IGZO(1:1:1)	IGZO(1:3:2)	IGZO(1:3:4)
Bandgap [eV]	3.2	3.5	3.4
Ionization potential (VBM) [eV]	8.1	8.3	8.2

In addition to this, increasing the amount of In promotes the electrical conduction by increasing the Hall mobility as seen in Figure 4.6, but the oxygen bonding strength of In–O is weaker than for the other elements (Ga and Zn). Therefore, In–O bonds are easily separated, causing defect states owing to oxygen vacancies.

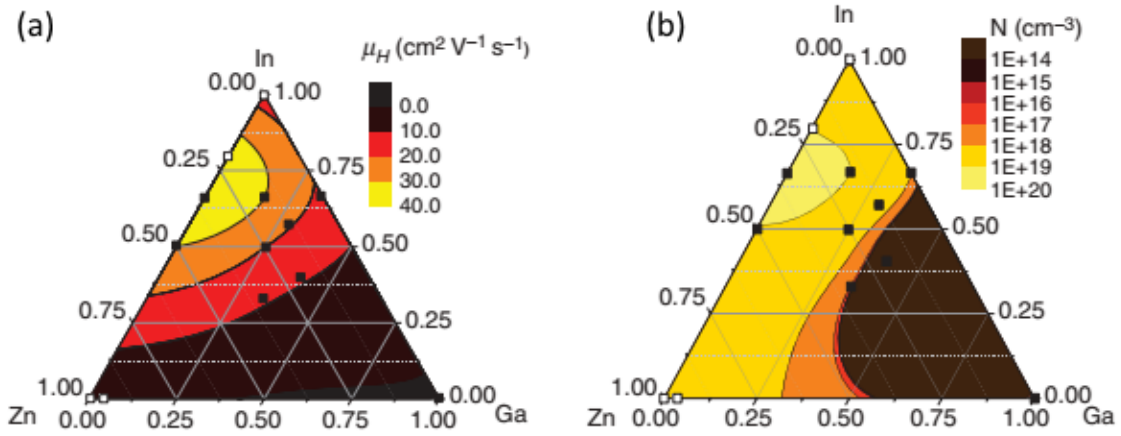

Figure 4.6. Ternary diagrams for indium-gallium-zinc oxide system, for films annealed at 500°C, showing (a) μ and (b) N, respectively (Source: Nomura et al., 2002).

Figure 4.7 shows the correlation of IGZO characteristics with different In, Ga, and Zn content.

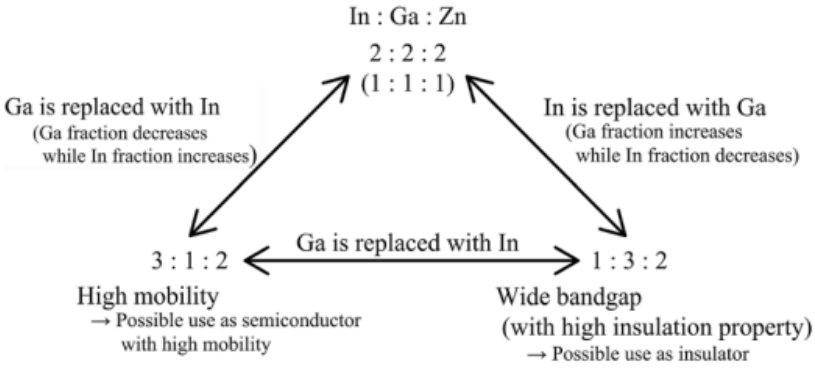

Figure 4.7. Estimated characteristics of IGZO with different In, Ga, and Zn content (Source: Sheng et al., 2019).

Figure 4.8 shows the effect of $O_2/(O_2+Ar)$ ratio during magnetron sputter deposition of a-IGZO thin films on electrical conductivity. This makes in situ optimization of electrical properties possible during thin film deposition.

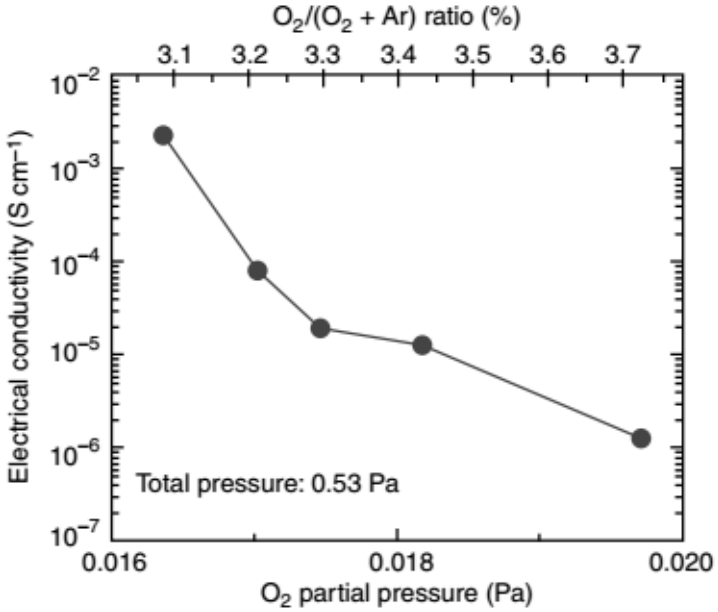

Figure 4.8. 'Conductivity-well' for $InGaZnO_4$ AOS RF magnetron sputter deposited at RT (Source: Kamiya et al., 2010).

CHAPTER 5

RESULTS AND DISCUSSION

5.1. Surface Morphology and Chemical Composition

Surface features of thin films such as morphology, roughness, pinholes, cracks and particulation was examined via SEM. Elemental and compositional analysis of the thin films were conducted by EDX.

The intrinsic ZnO thin film produced at 50 W showed smooth and intact surfaces even at relatively high magnifications. There were very few disruptions on the film surface, albeit existing ones possibly resulting from substrate defects. At higher magnifications, the film exhibited a very fine grain structure which is a sign of high homogeneity and superordinate degree of crystallinity. This can be correlated with the low sputtering power which induces mild erosion of the target, thus yielding refined sputtered species. This allows the fine sputtered particles to arrive at substrate surface with lower kinetic energies just enough to precipitate on it. Consequently, crystallites that grow at nucleation sites form a regular film surface. Figure 5.1 (a) and (b) shows SEM images of the film surface at different magnifications to indicate morphological features on the surface.

In contrast to the film deposited at 50 W, the intrinsic ZnO thin film produced at 100 W showed coarsely grained and highly defective surfaces even at low magnifications as depicted in Figure 5.2 (a). There were many disruptions on the film surface in the form of defects ranging from particulation to pinholes. At higher magnifications (Figure 5.2 (b)), the film exhibited a significantly coarser grain structure which is a sign of high irregularity and subordinate degree of crystallinity. This can be correlated with the high sputtering power which induces severe erosion of the target, thus yielding denser sputtered species precipitating on the substrate leading to both coarser grains and particulation having particle sizes ranging from 100 nm to 1 μm (Figure 5.3 (a), (b)).

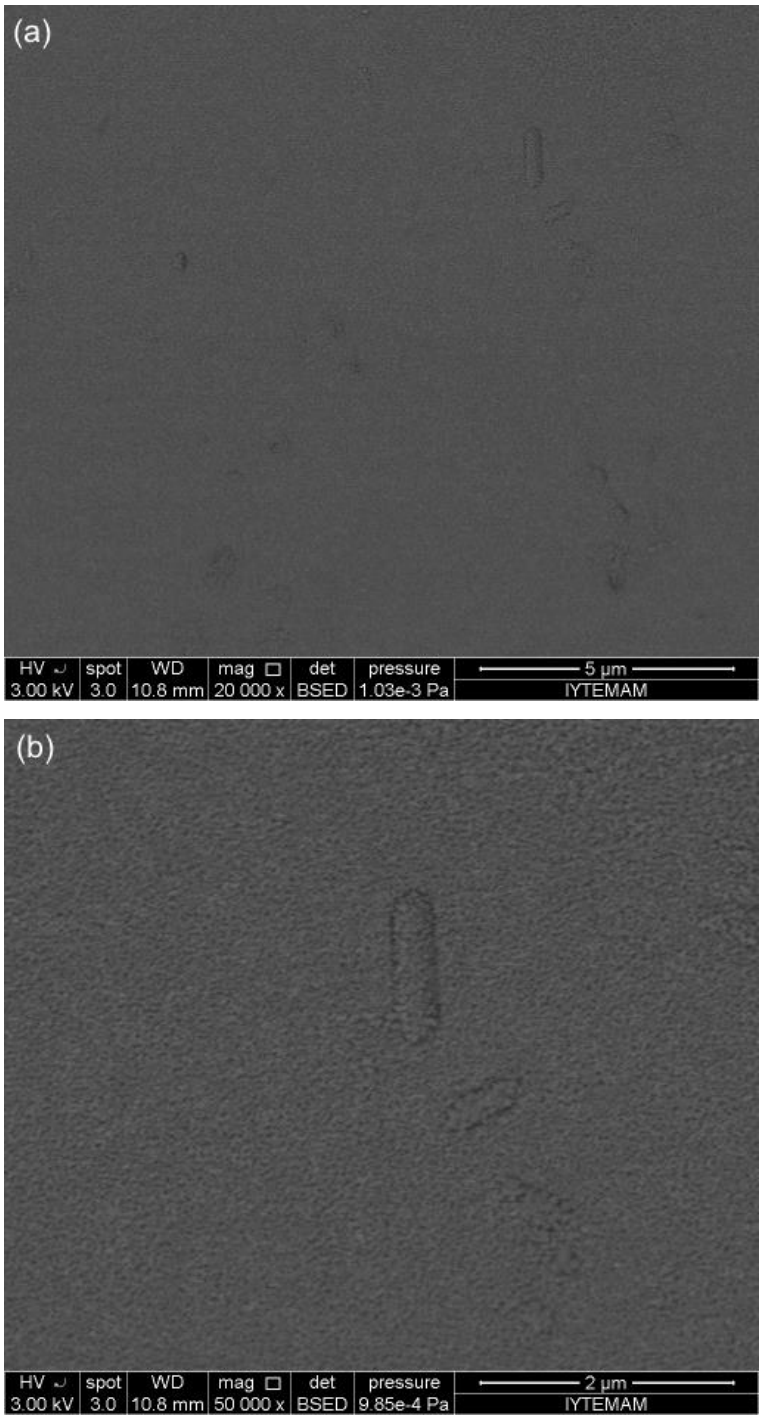

Figure 5.1. SEM images of intrinsic ZnO thin film surface deposited at 50 W (a) 20.000 x magnification (b) 50.000 x magnification

The high energy allows bulky sputtered particles to arrive at substrate surface with moderately high kinetic energies enough to precipitate on it but also causes already precipitated material to detach from the surface as a result of the high energy impact. This generates pinholes which cause prominent discontinuities on the film surface

(Figure 5.4 (a), (b)). Consequently, crystallites that grow at coarse nucleation sites, particulates and pinholes form an irregular film surface.

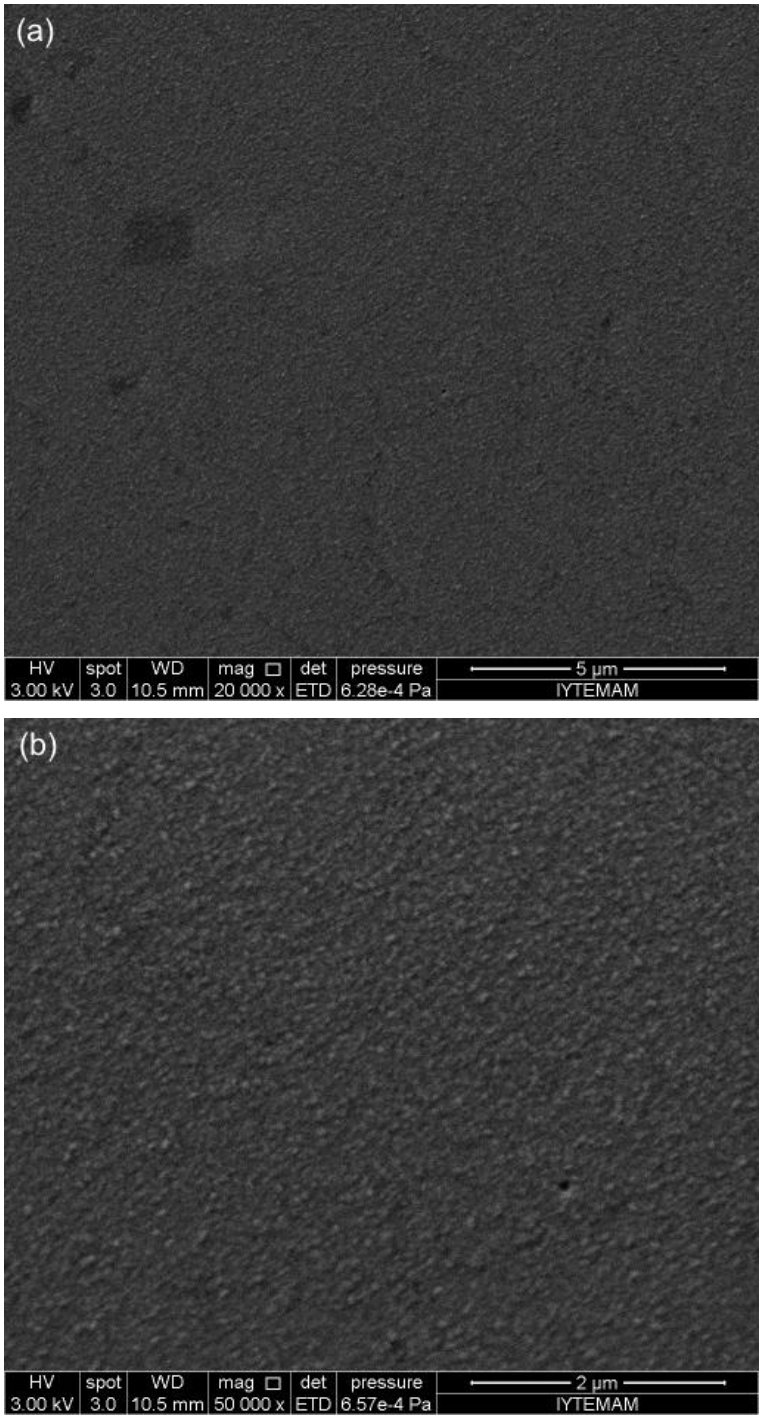

Figure 5.2. SEM images of intrinsic ZnO thin film surface deposited at 100 W. (a) 20.000 x magnification. (b) 50.000 x magnification.

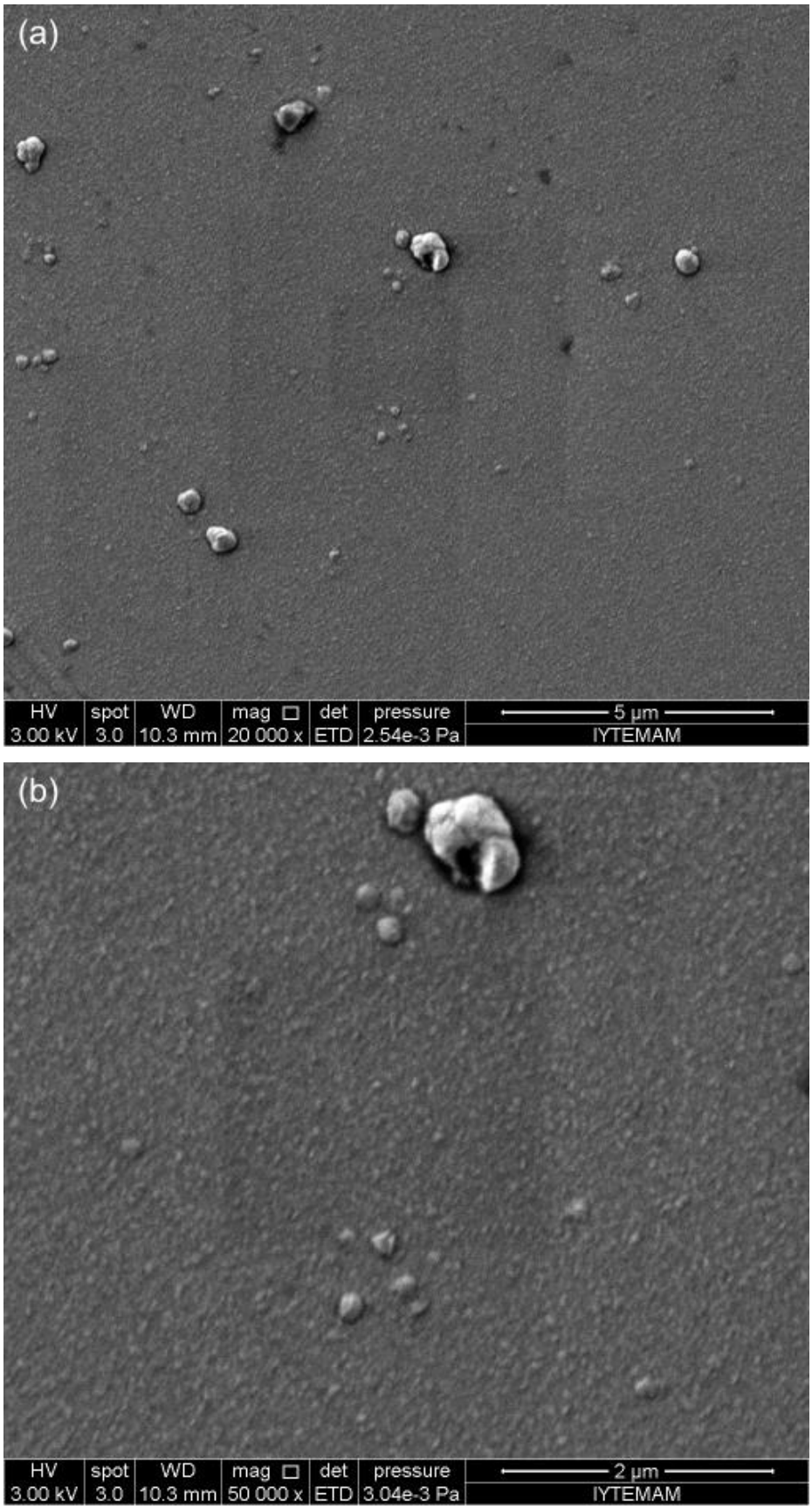

Figure 5.3. Detailed inspection of particulation on ZnO thin films produced at 100 W (a) 20.000 x magnification (b) 50.000 x magnification

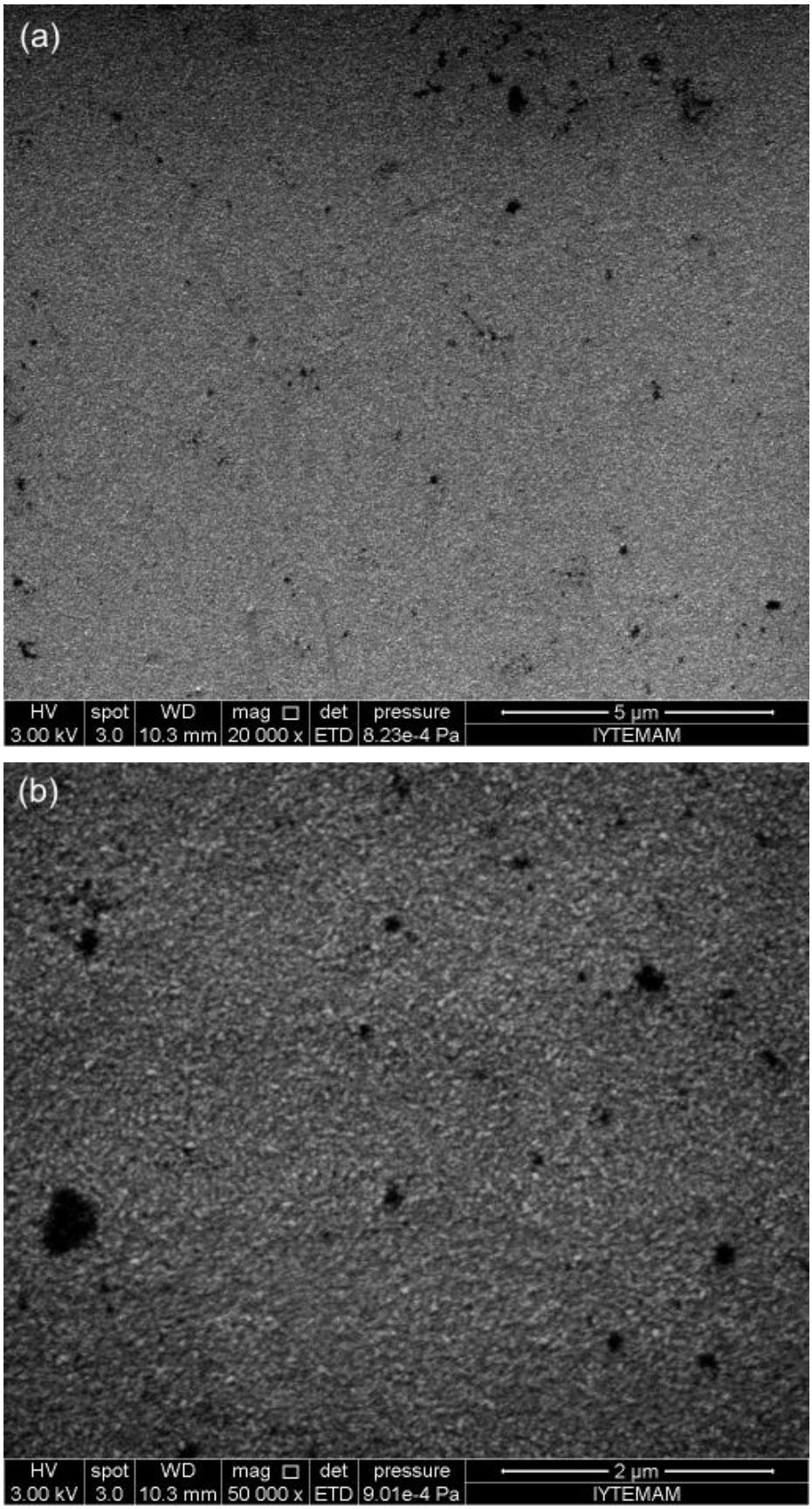

Figure 5.4. Detailed inspection of pinholes on ZnO thin films produced at 100 W (a) 20.000 x magnification (b) 50.000 x magnification

EDX spectra shows nearly stoichiometric ZnO compositions for both thin films produced at 50 W and 100 W.

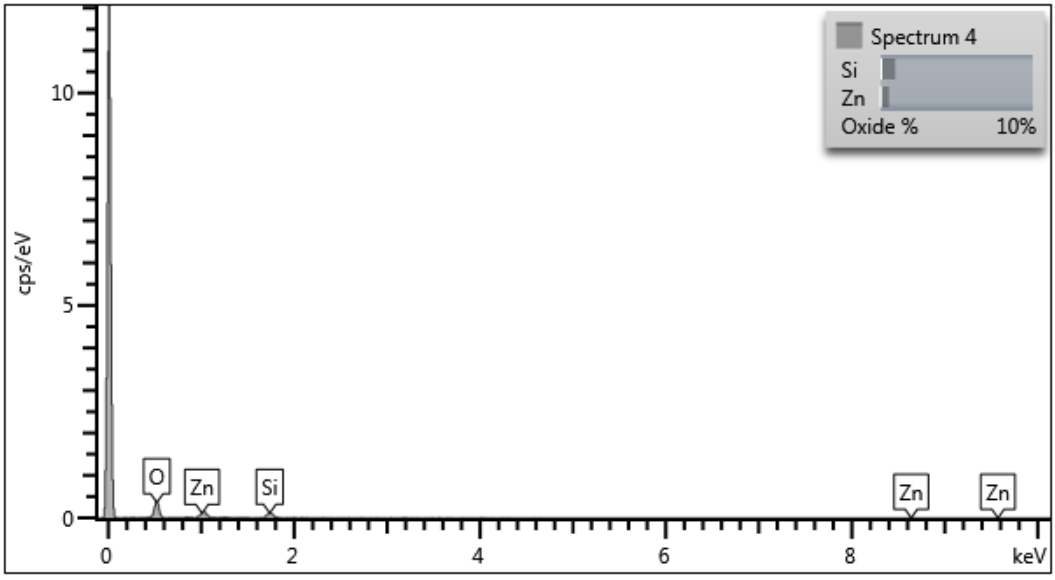

Figure 5.5. EDX spectrum lines of the intrinsic ZnO thin film deposited at 50 W.

Table 5.1. Elemental and compositional analysis of the intrinsic ZnO thin film deposited at 50 W.

Element	wt%	Oxide	Oxide %
O	0.67		
Si	0.48	SiO_2	1.03
Zn	0.50	ZnO	0.62
Total	1.65		1.65

The spectrum lines of the film deposited at 50 W is significantly low due to lower backscattered electron energies used during analysis. Silicon oxide lines in the spectrum result from the quartz substrates.

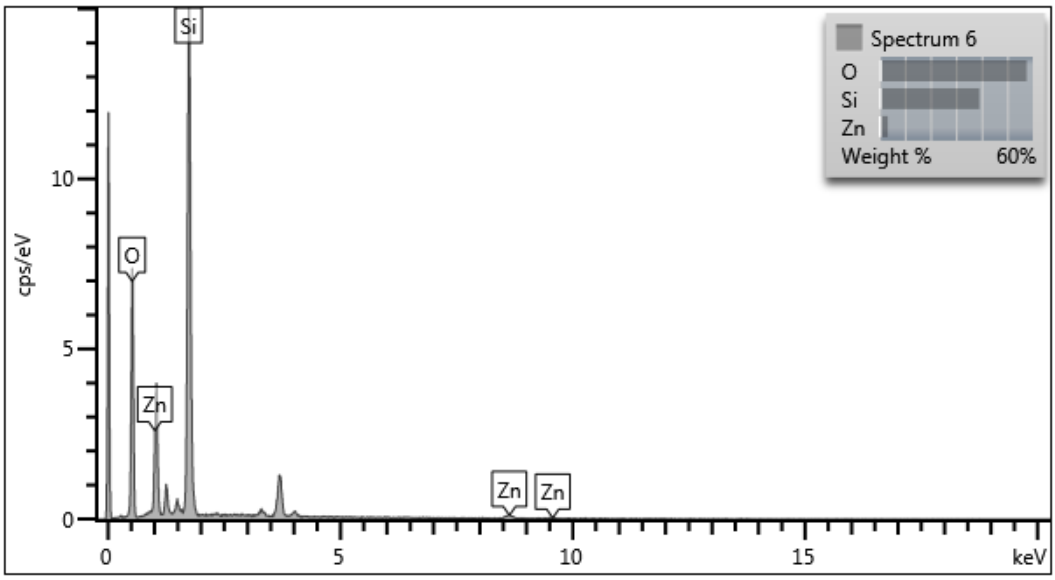

Figure 5.6. EDX spectrum lines of the intrinsic ZnO thin film deposited at 100 W.

Table 5.2. Elemental and compositional analysis of the intrinsic ZnO thin film deposited at 100 W.

Element	wt%	Atomic %
O	56.78	70.86
Si	39.30	27.94
Zn	3.91	1.20
Total	100.00	100.00

5.2. Crystal Structure

XRD analysis of the ZnO thin films revealed a highly (0002) oriented wurtzite ZnO crystal structure with a single strong reflection at 2θ angle of 34,3° for both films deposited at 50 W and 100 W. (Figure 5.7, Figure 5.8)

The Gaussian fits of the 2θ reflection peaks of the ZnO thin films deposited at 50 W and 100 W had a FWHM of 0,5933 and 0,6211 degrees, respectively. This indicated that the ZnO thin films are polycrystalline in nature and the crystallinity was found to be improved at the lower sputtering power of 50 W.

The mean crystallite size (D) was evaluated according to broadening of the highest intensity peak corresponding to (0002) diffraction plane using the Debye-Scherrer relation shown in Equation 5.1:

$$D = \frac{0{,}9\,\lambda}{\beta \cos\theta} \tag{5.1}$$

where, λ, β, and θ are the characteristic X-ray wavelength in Å, full width at half maximum (FWHM) in radians and Bragg's angle, respectively.

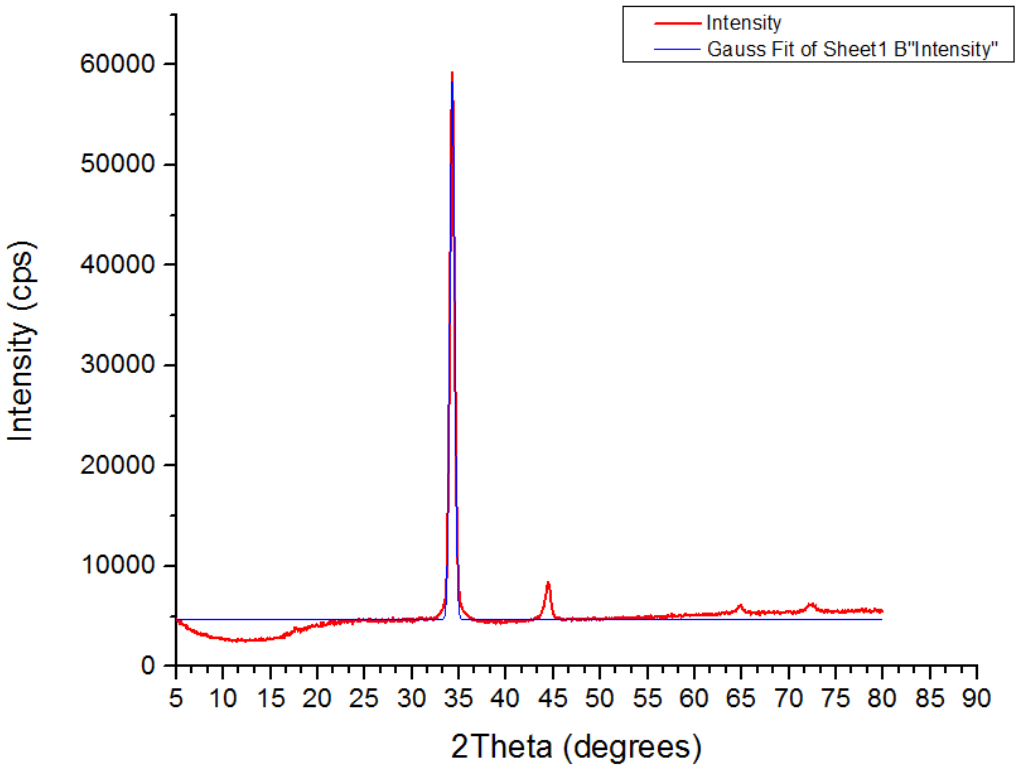

Figure 5.7. XRD data of the intrinsic ZnO thin film deposited at 50 W.

The mean crystallite sizes (D) of the ZnO thin films that were deposited at 50 W and 100 W were found to be approximately D_{50}=14 nm and D_{100}=13,4 nm, respectively. This indicates similar crystallite sizes for both ZnO thin films despite prominently different grain structures at the macro scale observed in SEM examinations. This finding suggests that sputtering power does not have a pronounced effect on crystallite size in this control experiment. But it provides evidence that the grain structure is heavily influenced by the twofold sputtering power increase. This result can be

harnessed to reduce grain sizes at low sputtering powers and increase crystallite sizes at elevated production or annealing temperatures to suppress XRD peak broadening. This will lead to polycrystalline ZnO thin films with larger crystals having less grain boundaries and defects, which are known to be natural electron current and light scattering centers in optoelectronic applications.

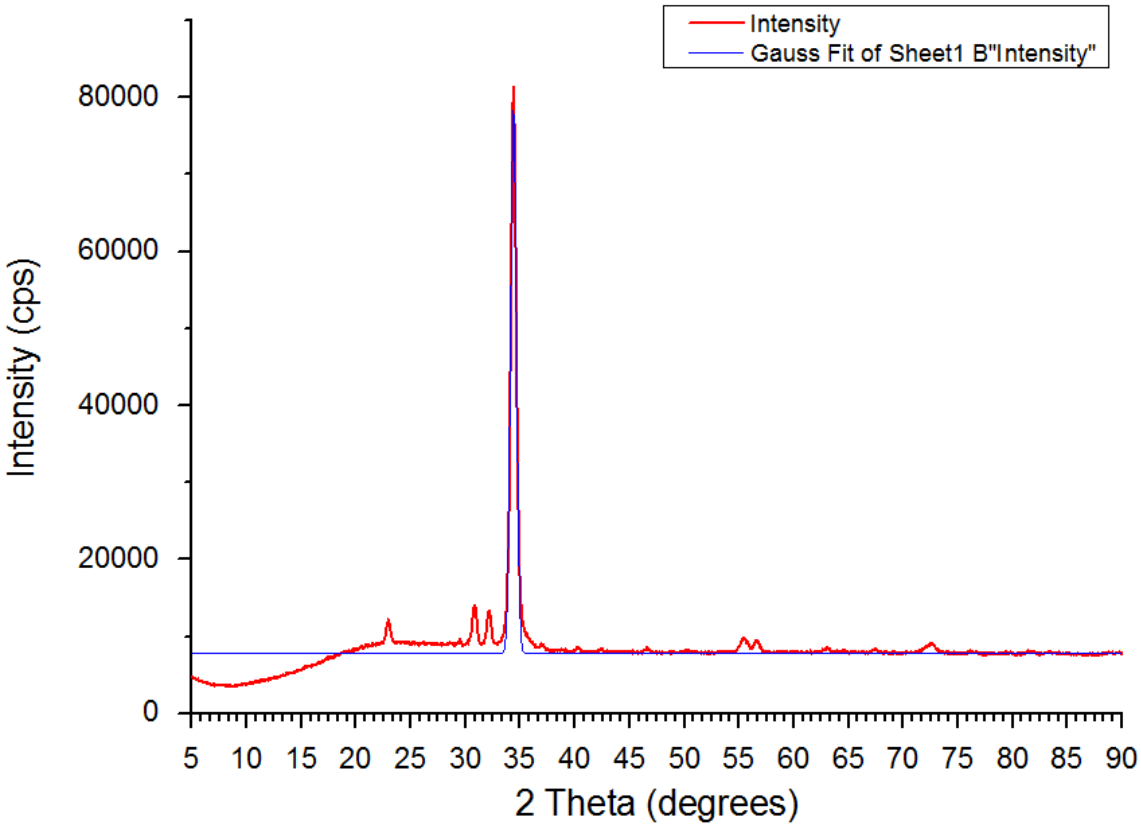

Figure 5.8. XRD data of the intrinsic ZnO thin film deposited at 100 W.

5.3. Surface Topography and Thickness

Three separate step measurements between the ZnO thin film and substrate surface was made from different sharply masked sites on the surface of the film. The average thickness values of the ZnO thin films produced at 50 W (BZO 1) and 100 W (BZO 2) were found to be approximately 110 nm and 220 nm, respectively. Deposition time being taken constant for the two samples at 100 minutes, a linear correlation was found between sputtering power and resulting film thickness. Double the sputtering power yielded twofold ZnO film thickness at the same deposition conditions denoted in

Table 5.3. To demonstrate the topographic features of ZnO thin films, 20 µm x 20 µm areal scans in tapping mode AFM were performed on the film surfaces.

Table 5.3. Separate AFM thin film thickness measurements and average AFM thickness of ZnO thin films deposited at 50 W and 100 W power.

Sample Name	AFM Thickness Measurement 1	AFM Thickness Measurement 2	AFM Thickness Measurement 3	Average AFM Film Thickness
BZO 1	109 nm	114 nm	107 nm	110 nm
BZO 2	217 nm	222 nm	221 nm	220 nm

The topographic features revealed by AFM showed details of the surface morphology previously generated via SEM inspections. In accordance with SEM results, AFM inspection of the ZnO thin film deposited at 50 W power exhibited fine grains on the film surface along with homogenous and continuous surface features. On the contrary, AFM inspection of the ZnO thin film deposited at 100 W power showed coarsely grained surfaces with numerous large disruptions on the film surface in the form of particulation. This result is consistent with the SEM inspection of the same film showing severe particulation due to high sputtering power.

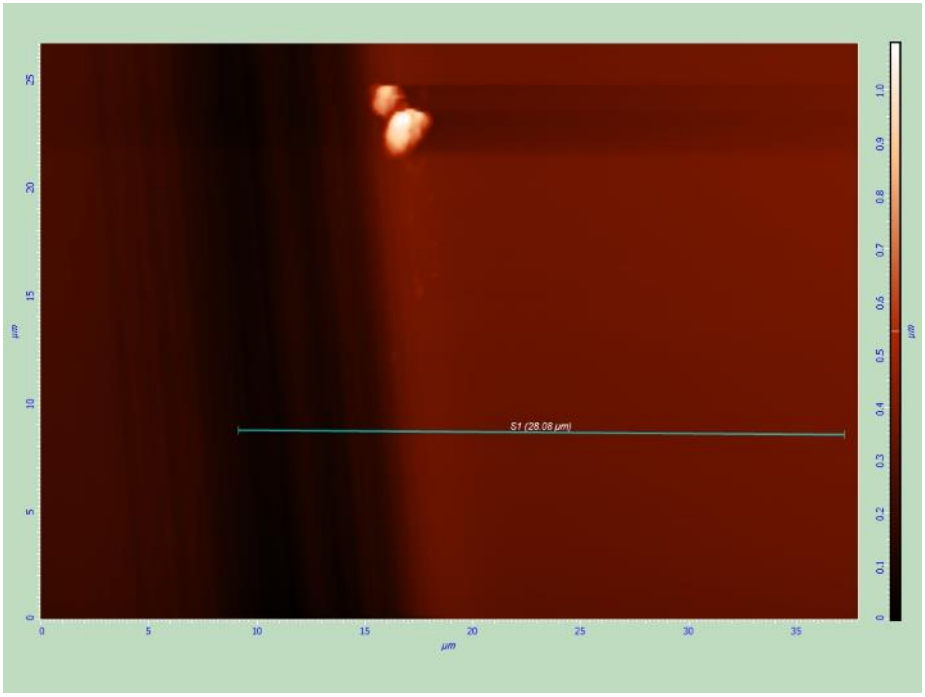

Figure 5.9. AFM image of one of three discrete step measurement sites on the intrinsic ZnO thin film.

Those results hint at lower sputtering powers are favorable for better thin film surfaces, which are more suitable for manipulation via elevated temperature production and in-situ or post-annealing processes to produce films with superior quality for optoelectronic applications.

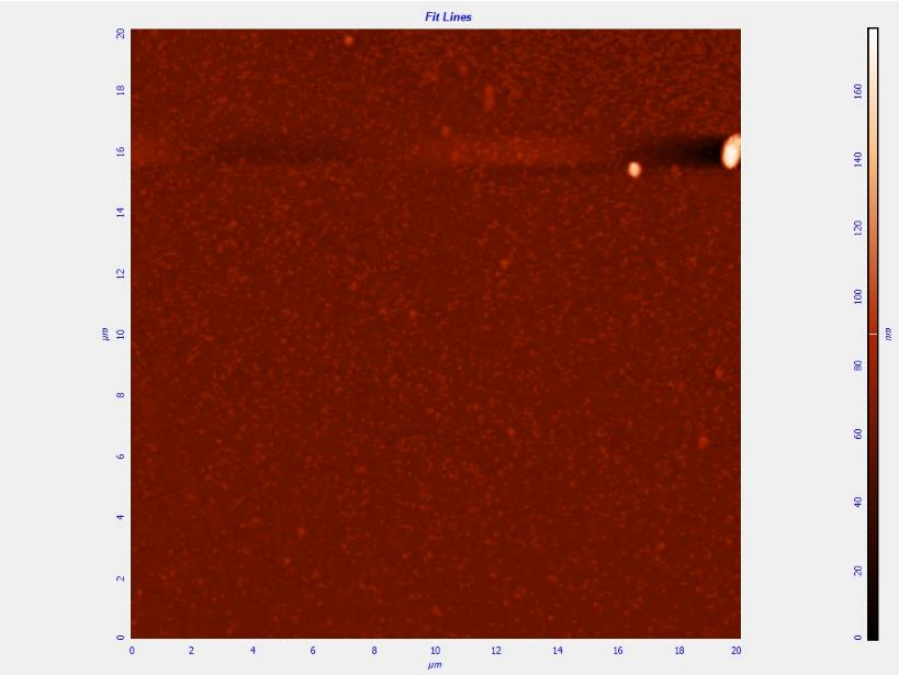

Figure 5.10. AFM image of the surface of intrinsic ZnO thin film deposited at 50W.

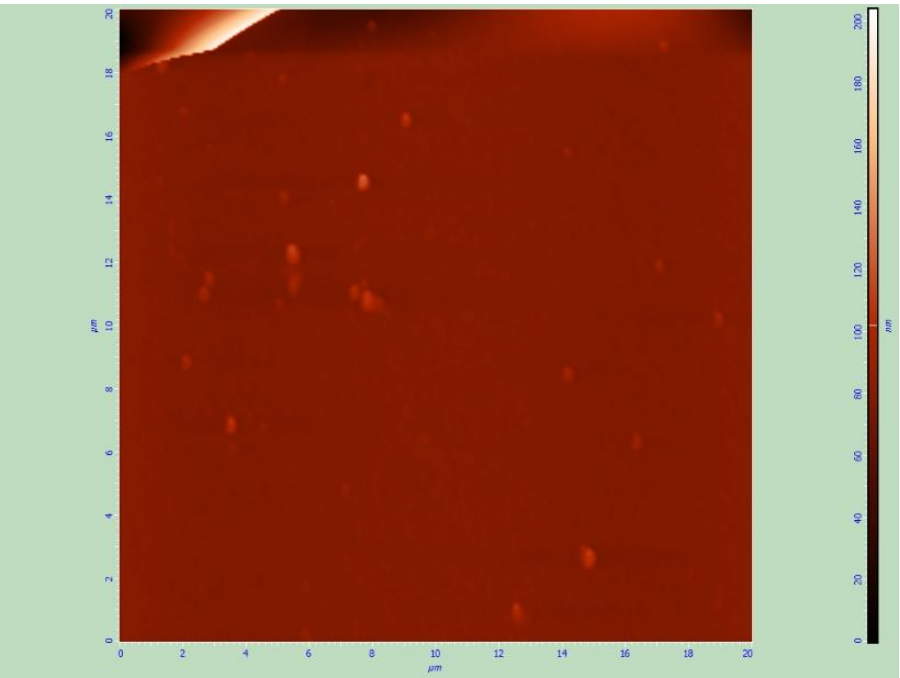

Figure 5.11. AFM image of the surface of intrinsic ZnO thin film deposited at 100W.

5.4. 4-Point Probe van der Pauw Measurements

Table 5.4 summarizes the electronic properties of all samples probed via van der Pauw method.

Table 5.4. Comparative list of production parameters of the two intrinsic and ZnO thin films in initial production runs.

Sample Name	Substrate Temperature (°C)	Sheet Resistance (Ω/□)	Carrier Concentration (cm^{-3})	Hall Mobility ($cm^2/V.s$)
ZNO-1	RT	N/A	N/A	N/A
ZNO-2	200	$6,34x10^3$	$5x10^{16}$	0,03
AZO-1	RT	$4,14x10^3$	$3x10^{20}$	0,2
AZO-2	RT	$2,62x10^3$	$2x10^{18}$	0,4
AZO-3	200	$7,6x10^3$	$2x10^{21}$	2,1
AZO-4	200	$5,84x10^3$	$6x10^{19}$	1,5
AZO-5	200	$7,58x10^3$	$7x10^{18}$	1,1

ZnO is already known as an intrinsic n-type semiconductor due to oxygen defects inherently present in its crystal structure. Those defects which are formed during production of ZnO materials induce n-type conductivity at room temperature for an otherwise insulating material having an energy band gap of 3.36 eV.

For the undoped sample ZNO-1, sheet resistance, carrier concentration and Hall mobility data could not be extracted from van der Pauw measurements which may be attributed to the high resistance of the sample which lies outside the measurement equipment's range. But as the deposition temperature was increased to 200 °C from RT, undoped ZnO film sample ZNO-2 yielded electrical measurement data. Electronic characterization results indicated a relatively high carrier concentration for the undoped ZnO sample ZNO-2 produced at 200 °C. This behavior is thought to be the result of the elevated deposition temperature. The elevated temperature increases intrinsic carrier concentration by introducing oxygen vacancy (V_O) defects into ZnO crystal structure. In literature, pure (intrinsic) zinc oxide is classified as inherently n-type due to those mentioned oxygen defects even in its bulk forms. Defect formation is

thermodynamically favorable at high deposition temperatures, since oxygen content of the ZnO thin films will be lower because of the smaller sticking coefficient during deposition and increased releasing tendency of O from ZnO lattice at higher temperatures. So, we concluded that oxygen gas must be introduced in the sputtering gas along with Ar to compensate for the non-stoichiometric elemental composition of ZnO, even though ZnO was already sputtered from and oxide target.

For the Al-doped samples, measured carrier concentration values ranged from 10^{18} to 10^{21} cm^{-3} for the specified deposition conditions.

One interesting aspect of these electronic measurement results was the relatively high carrier concentration of the ZNO-2 sample. A carrier concentration on the order of 10^{16} cm^{-3} is unexpectedly high to be only held accountable for oxygen vacancies. So a simple 2-point contact resistance measurement was made on the Al electrode and blank sample which was fabricated for optical measurements. Unwittingly, roughly a three orders of magnitude higher resistance value was recorded for the blank sample than the Al electrode sample. This result can be explained by aluminum diffusion in the ZnO thin films that were deposited at 200 °C. During deposition of ZnO thin films at elevated temperatures, Al diffusion from the contact points into the film caused unintentional n-type doping of the ZnO films.

5.5. UV–Vis Spectroscopy

Within the visible region, the average transmittance is about 60% except for the sample UZO-01. The absorption edge of the samples was around 385 nm, again except for the sample UZO-01. Figure 5.12 shows the transmission spectra of the fabricated undoped ZnO thin films.

Film thickness values of the samples were determined from the interference fringes according the equation below;

$$t = \frac{\lambda^2}{2n\Delta\lambda} \tag{5.2}$$

where t is the thickness of the thin film, λ is the wavelength of the nearest peak to the absorption edge, n is the refractive index of ZnO at λ and $\Delta\lambda$ is the difference between

the wavelengths of two neighboring peaks in the transmission spectrum. Table 5.5 shows the calculated thickness values of the samples.

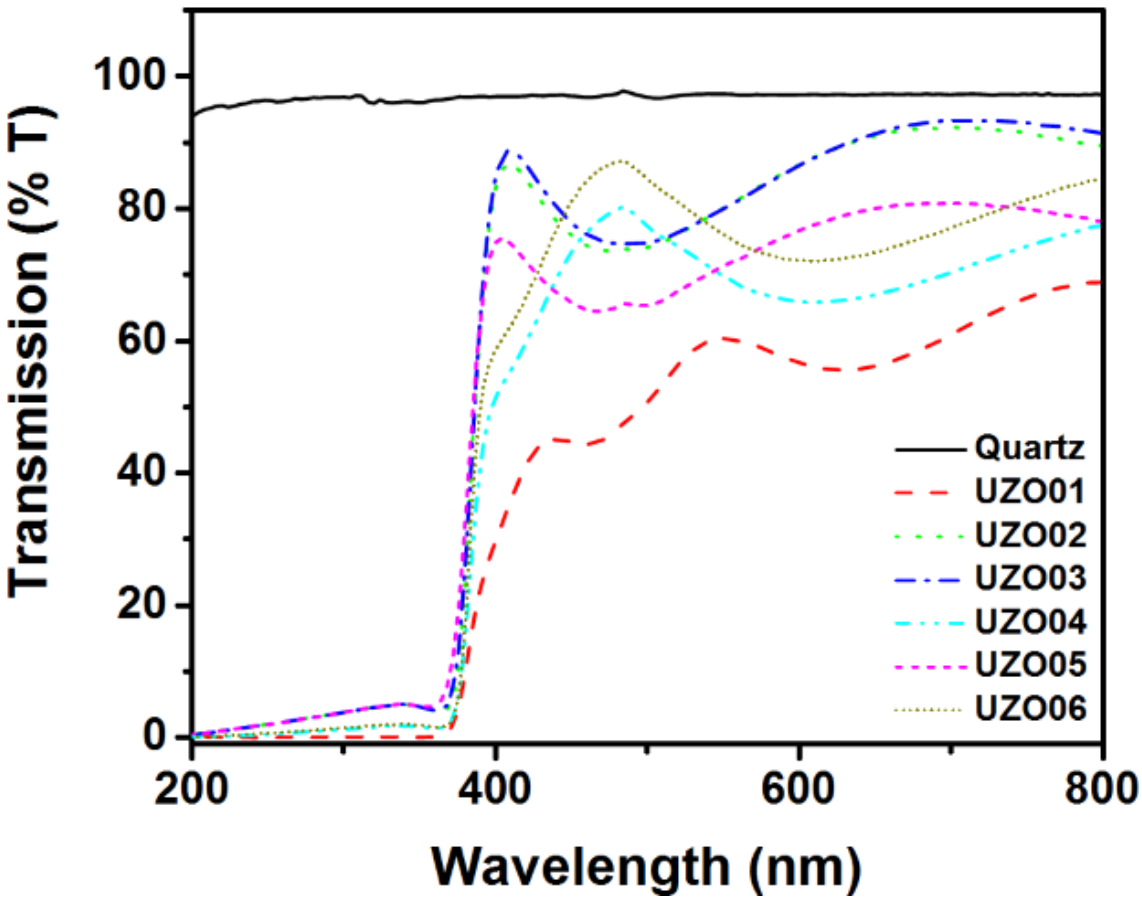

Figure 5.12. Transmission spectra of the fabricated undoped ZnO thin films.

Table 5.5. Thickness values of the samples calculated from transmission data.

Sample Name	UZO-1	UZO-2	UZO-3	UZO-4	UZO-5	UZO-6
Thickness	520 nm	170 nm	170 nm	190 nm	165 nm	190 nm

Inspection of thickness data reveals that, the samples fabricated with pure Ar are slightly thicker than the ones fabricated with Ar–O_2 mixture. It can be inferred that the difference in thickness values can be due to variations in the sputtering yields of Ar and O_2, where Ar has a greater yield than O_2 and hence the slightly thicker films deposited with pure Ar.

The optical bandgaps of fabricated thin films were evaluated by using a method Tauc et al. proposed for determining the bandgap using optical absorbance data plotted

appropriately with respect to energy. This method implies that the optical absorption strength depends on the difference between the photon energy and the band gap as follows:

$$(\alpha h\nu)^{1/n} = A(h\nu - E_g) \tag{5.3}$$

where h is Planck's constant, ν is the photon's frequency, α is the absorption coefficient, E_g is the bandgap, and A is a proportionality constant.

The value of the exponent denotes the nature of the electronic transition, whether allowed or forbidden and whether direct or indirect. For direct allowed transitions n = 1/2, for direct forbidden transitions n = 3/2, for indirect allowed transitions n = 2, and for indirect forbidden transitions n = 3. Typically, the allowed transitions dominate the basic absorption processes and since ZnO is a direct bandgap semiconductor the exponent was taken as n = 1/2.

When Tauc plots for ZnO where the absorption coefficient times the photon energy to the second power $(\alpha h\nu)^2$ is plotted versus the incident photon energy $(h\nu)$, their characteristic features become evident. At low photon energies the absorption approaches zero—the material is transparent; near the bandgap value the absorption gets stronger and shows a region of linearity in the squared-exponent plots. This linear region is used to extrapolate to the X-axis intercept to find the bandgap value. At even higher energies, the absorption processes saturate and the curve again deviates from linear. Figure 5.13 shows the Tauc plots of the fabricated undoped ZnO thin films.

Optical bandgap energies of the undoped ZnO thin film samples determined from Tauc plots are presented in Table 5.6. Average optical bandgap values of the undoped ZnO thin film samples were about 3,26 eV which is consistent with single crystal data.

Table 5.6. Optical bandgap energies of the undoped ZnO thin film samples determined from Tauc plots.

Sample Name	**UZO-1**	**UZO-2**	**UZO-3**	**UZO-4**	**UZO-5**	**UZO-6**
Optical Bandgap (E_g)	3,27 eV	3,25 eV	3,25 eV	3,25 eV	3,26 eV	3,26 eV

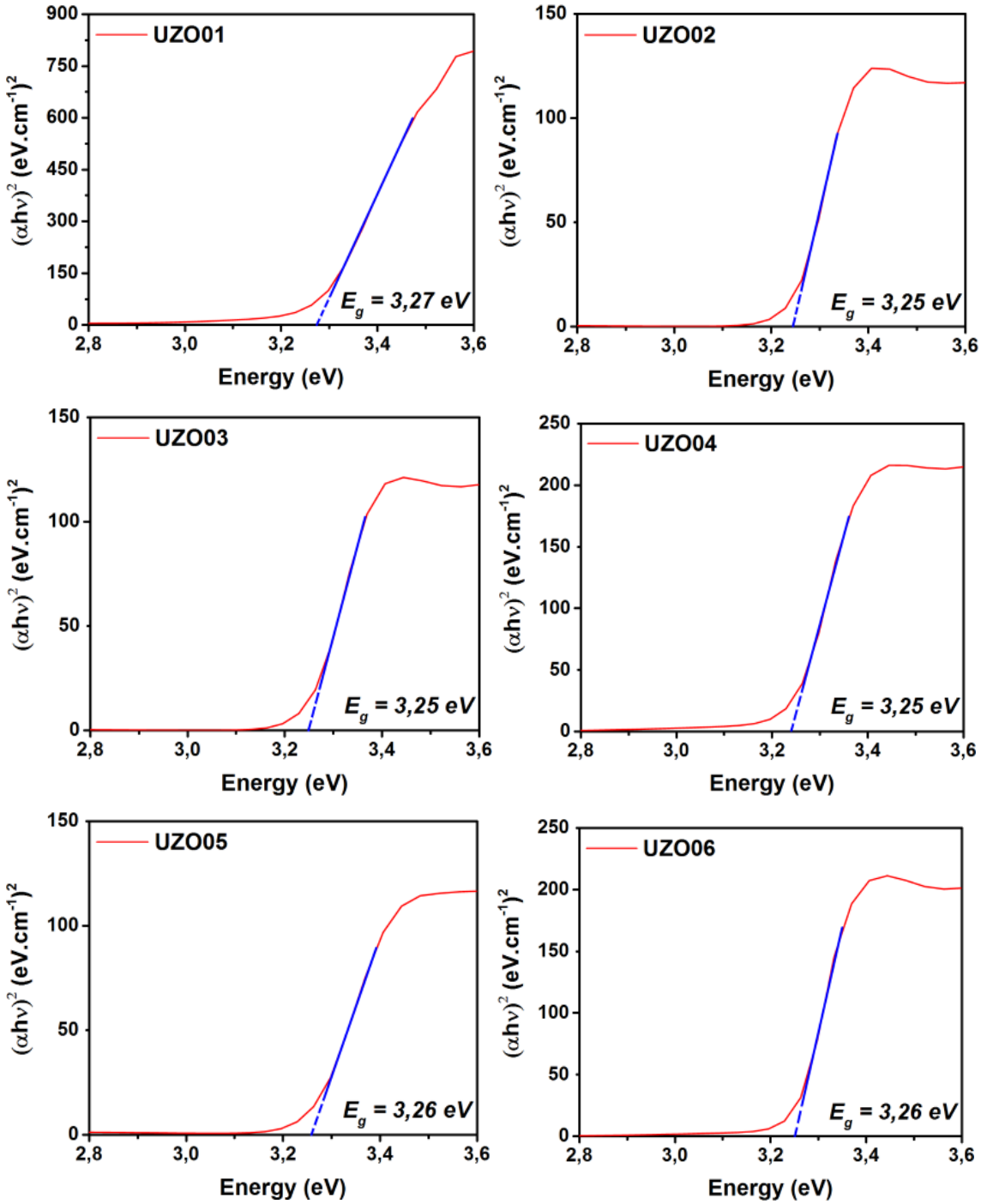

Figure 5.13. Tauc plots of the fabricated undoped ZnO thin films.

In the previous section, where a linear region was selected and justified for extrapolation, there were lower and upper deviations from linear behavior. On the low energy end, the deviation from linearity can be associated with defect absorption states that are near the band edge. This phenomenon has been investigated by Urbach and in subsequent years, identified as an “Urbach Tail”. These states are usually described by

an exponential function, corresponding to a typical distribution of density of states, evident in the absorption behavior seen in the low energy end of the Tauc plots in Figure 5.13.

The absorption coefficient can also be fit to the Urbach relation $\alpha \propto e^{E/E_0}$, where E_0 is called the Urbach slope and characterizes the width of exponential band-tailing into the gap and is frequently used as a measure of disorder and impurities in thin films. The Urbach slope is found from a linear fit to a plot of $\log(\alpha)$ versus photon energy $(h\nu)$. This linear region is used to extrapolate to the X-axis intercept to find the Urbach slope. The Urbach disorder parameter is the inverse of the Urbach slope. Figure 5.14 shows the Urbach slopes of the fabricated undoped ZnO thin films.

Average values of the Urbach disorder parameter E_0 are included in Table 5.7. This energy characterizes the width of exponential band tailing ("fuzziness") associated with sample impurities.

Table 5.7. Urbach disorder parameters E_0 of the undoped ZnO thin film samples.

Sample Name	**UZO-1**	**UZO-2**	**UZO-3**	**UZO-4**	**UZO-5**	**UZO-6**
Urbach Disorder Parameter (E_0)	317 meV	309 meV	309 meV	312 meV	307 meV	310 meV

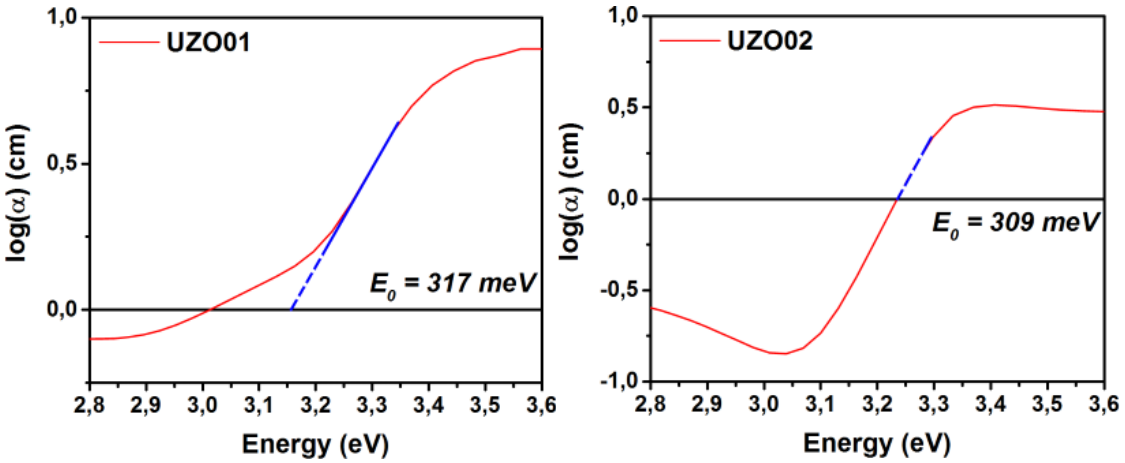

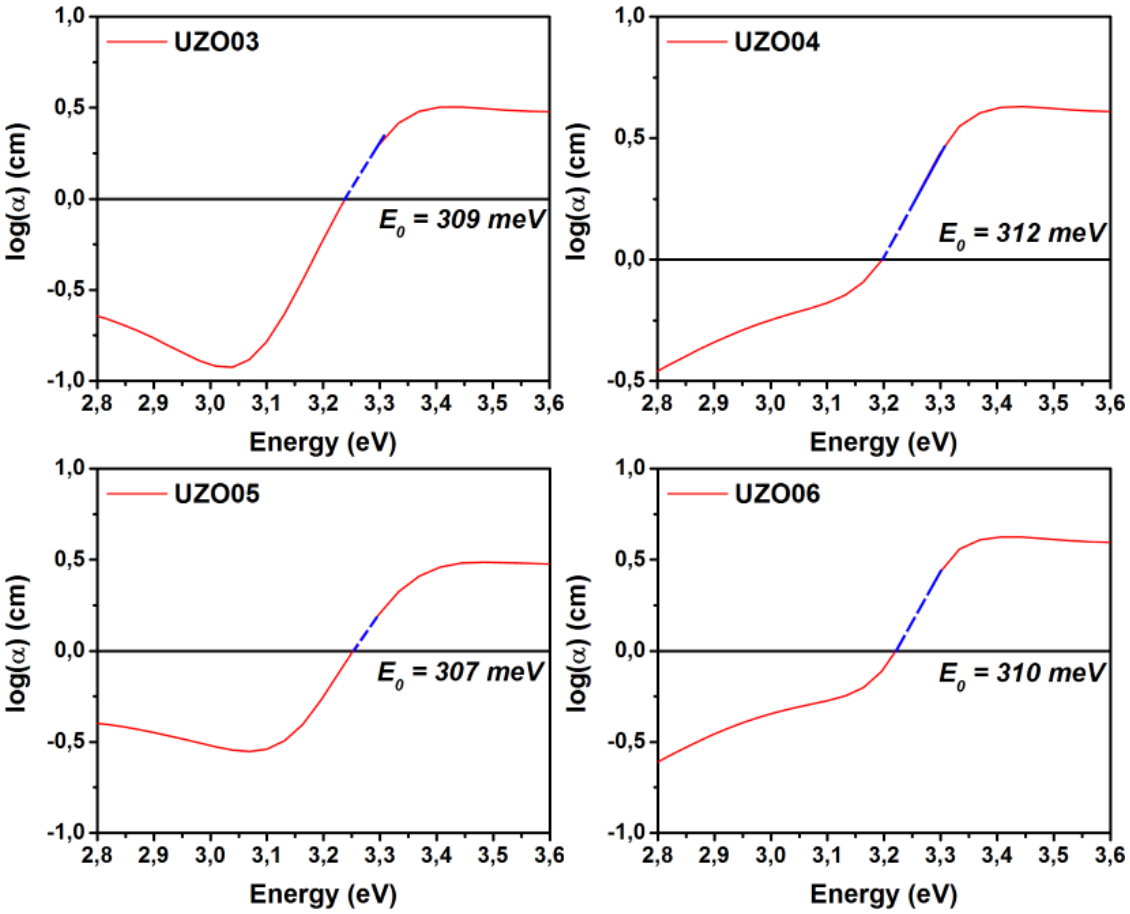

Figure 5.14. Urbach slopes of the fabricated undoped ZnO thin films.

5.6. Photoluminescence Spectroscopy

For the excitation energy of ~3,54 eV (350 nm) slightly above the ~3,36 eV (~370 nm) typical bandgap of ZnO, the photoluminescence spectra of the thin film samples fabricated with Ar–O_2 mixture (UZO-02, UZO-03, UZO-05) showed near-band emissions at 390 nm, 393 nm, and 392 nm, respectively. Whereas, the samples fabricated with pure Ar (UZO-01, UZO-04, UZO-06) showed emissions around 400 nm, 404 nm, and 404 nm, respectively.

Figure 5.15 shows the photoluminescence spectra of the fabricated undoped ZnO thin films.

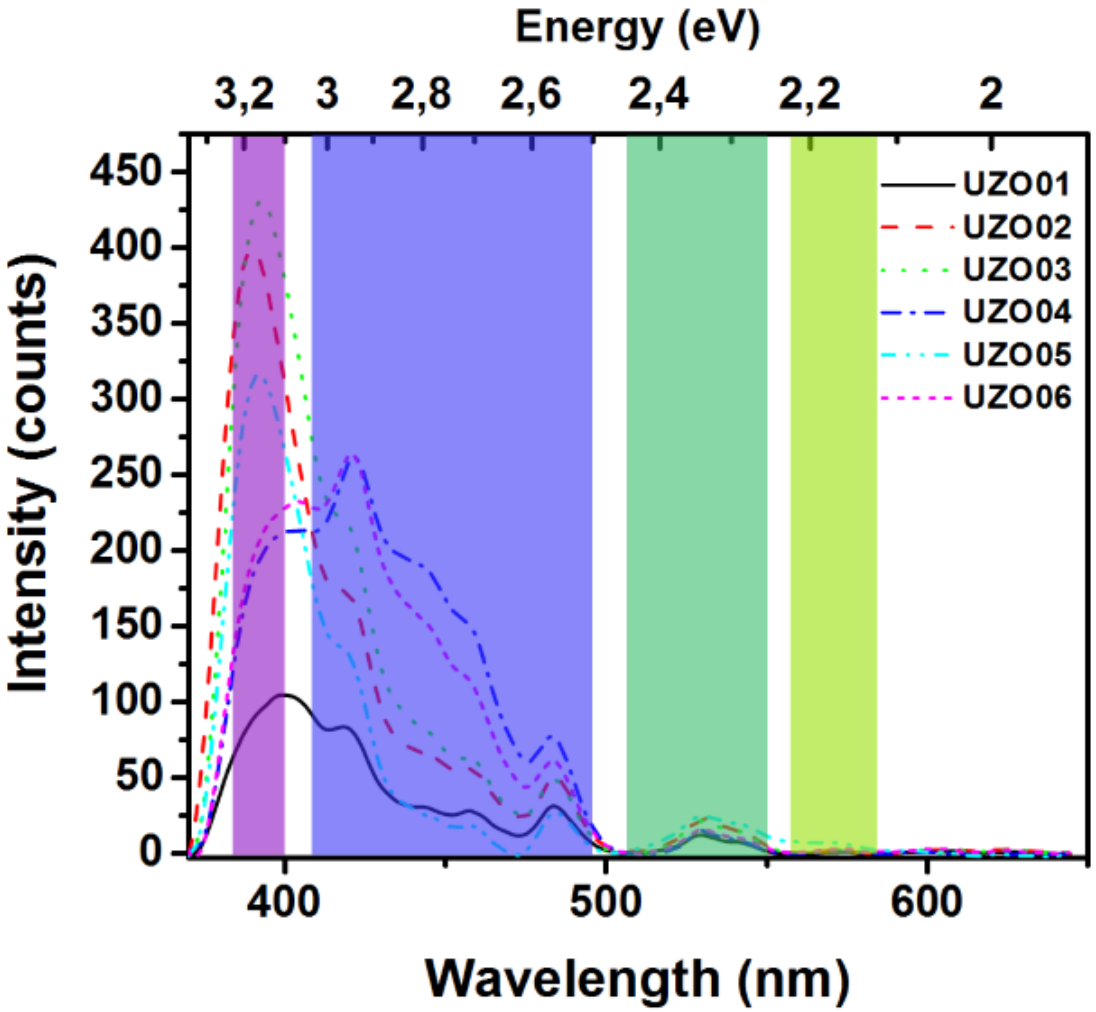

Figure 5.15. Photoluminescence spectra of the fabricated undoped ZnO thin films.

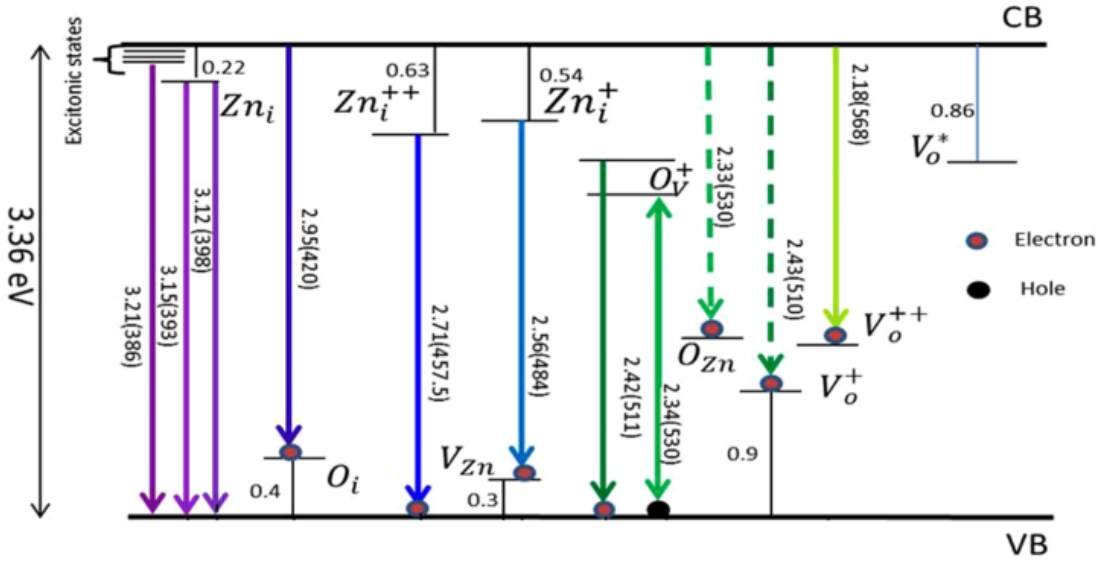

Figure 5.16. Schematic representation of emission schemes regarding the photoluminescence spectra of ZnO samples.

Figure 5.16 details the origins of the near-band and defect emissions of the fabricated undoped ZnO thin films which are attributed to transitions from excitonic levels and/or various defect states present in ZnO.

As widely reported in previous studies, ZnO possesses stable excitonic states just below (~60 meV) its CB minima, where transitions to VB give near-band violet emissions. The observed UV emission peaks at 390 nm, 392 nm, and 393 nm can be attributed to those transitions from excitonic levels to the valance band. Moreover, the violet emissions at 400 nm and 404 nm are close to electronic transitions from slightly lower energy excitonic states and/or zinc interstitials (Zn_i) lying ~0,22 eV below the conduction band to the valance band.

Along with these near-band emissions, all ZnO thin film samples exhibited visible emissions in the spectrum range spanning across ~420–570 nm, having distinct peaks at around 420 nm, 445 nm, 458 nm, 484 nm, 530 nm, 542 nm, and 570 nm.

In the visible region, the observed blue emission peak at ~420 nm correspond to transitions from CB to oxygen interstitials (O_i) located 0,4 eV above the VB. The other blue emission peak at ~457 nm can be assigned to transitions from extended Zn_i states to the valance band. The extended Zn_i states are generally classified as; localized Zn_i states, Zn_i^{++} and complex defects, whose energetic positions lie deep in the bandgap. The blue emission peaks at ~457 nm are in close agreement with the energy of transition Zn_i^{++} to VB (2,7 eV), indicating the presence of Zn_i^{++} states in the bandgap. The third blue emission peak located at ~484 nm corresponds to the transitions from Zn_i^{+} to V_{Zn}, as the energy difference between these levels (2.56 eV) is in close proximity to the observed emission energy. Furthermore, the general trend in the reduction of intensities of these peaks in the thin films fabricated with Ar–O_2 mixture at elevated temperatures confirms that their concentrations are closely dependent on the deposition parameters. By modifying these parameters, related emissions can be successfully suppressed, thereby eliminating these defects in the ZnO thin film structures.

Green emissions located in the 530–570 nm spectral region has three emission peaks located at 530 nm (2,34 eV), 542 nm (2,29 eV), and 570 nm (2,18 eV). The first green emission peak centered at 530 nm may come from the transitions $V_0^{+} \rightarrow$ VB or CB $\rightarrow O_{Zn}$.

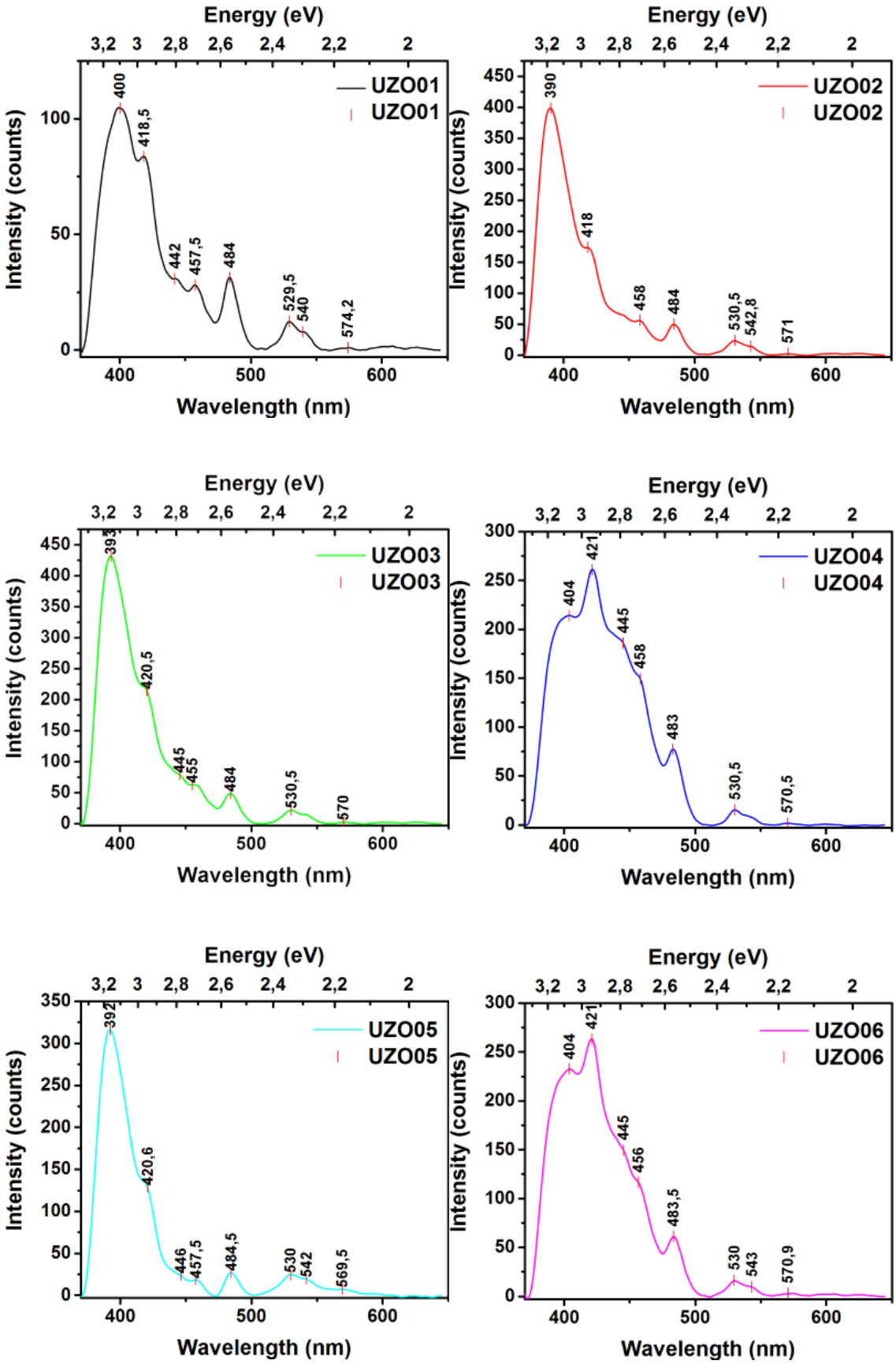

Figure 5.17. PL spectra of individual undoped ZnO thin film samples deposited at different substrate temperatures and sputtering gas compositions.

The first transition occurs due to the formation of unstable V_0^+ states by capturing electrons from CB. This unstable state, when recombined with a photogenerated hole in the valance band, generates green emission centered at 530 nm. The second transition CB → O_{Zn} also has a strong possibility, as the excitation energy is high enough to pump electrons into the CB. Subsequent relaxation of the excited electrons to the O_{Zn} states can yield green emission at 530 nm. The other green emission peak at 542 nm can be assigned to transitions from the neutralized oxygen vacancies V_0^* to the VB (V_0^* → VB). The third green emission peak located at 570 nm corresponds to the recombination of electrons from the conduction band with the doubly-ionized oxygen vacancies V_0^{++} (CB → V_0^+).

All these observations in the photoluminescence spectra of the fabricated ZnO thin films indicate that, all of the samples contain defect states such as; V_0^*, Zn_i, O_i, V_{Zn} , and O_{Zn} to some extent. And those defects can be manipulated by varying the fabrication parameters during thin film deposition and post-processing.

5.7. High Resolution XRD

It is well known that the (002) orientation of ZnO's wurtzite structure is generally observed in magnetron sputtered ZnO thin films, implying that the surface free energy of (002) plane is the lowest among others. This results in the favored formation of (002) oriented texture in ZnO thin films which grow along the c-axis of the (002) crystal plane orthogonal to the substrate surface.

Analysis of the XRD patterns revealed a preferentially (002) oriented wurtzite ZnO crystal structure with a single reflection peak at 2θ angle of ~34,4° for all deposited thin films. This indicated that the ZnO thin films are polycrystalline.

Figure 5.18 shows the XRD patterns of the fabricated undoped ZnO thin films. The peak intensities increased at elevated deposition temperatures, whereas FWHMs decreased. This trend indicates that crystallinity is strongly dependent on temperature. At elevated temperatures, sputtered species has more kinetic energy to relocate on the hotter substrate and subsequently can diffuse into equilibrium position not only with the incident kinetic energy it has gained from Ar sputtering but also with the "thermal kick" supplied by the hot substrate. This also affects grain sizes as indicated by the slight decrease in FWHM values of the peaks. Increasing the substrate

temperature promotes grain growth by intergranular diffusion through ZnO grains as evidenced by the decrease in peak FWHMs at elevated temperatures.

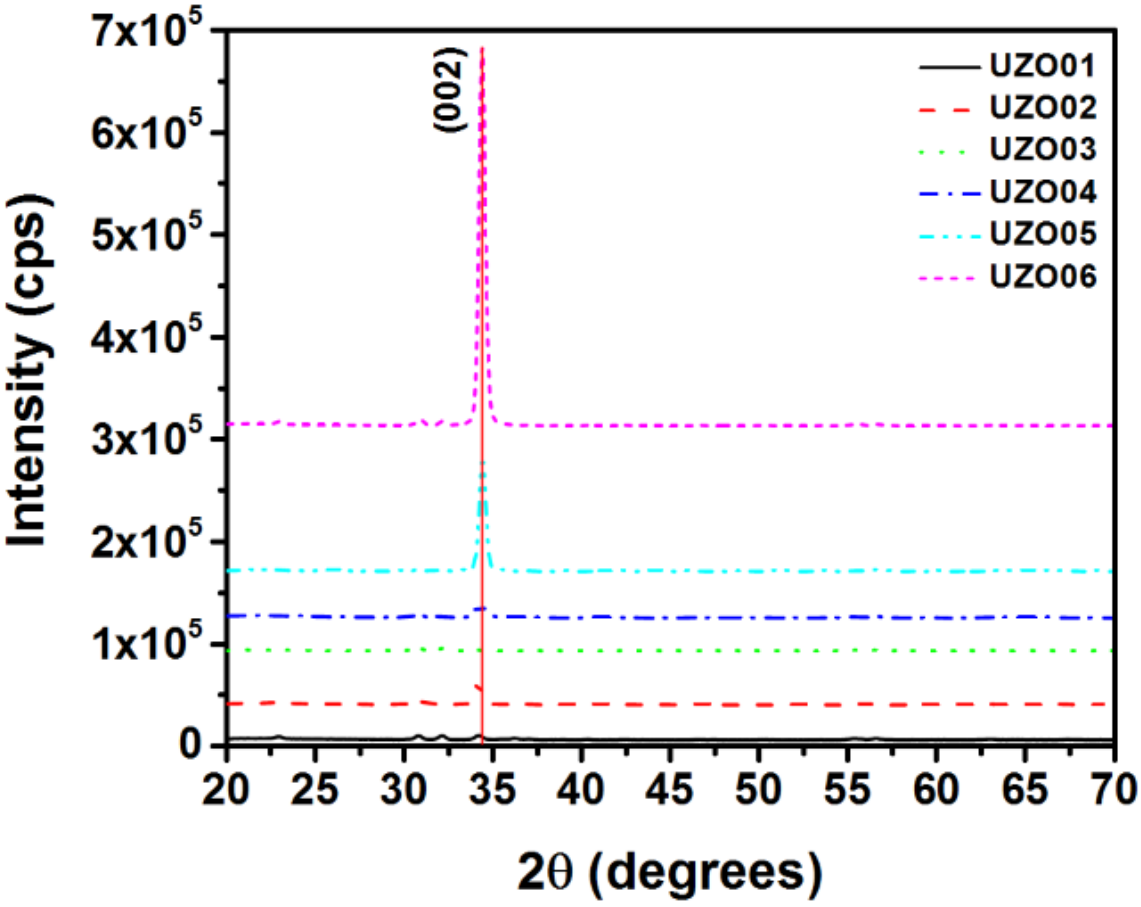

Figure 5.18. XRD patterns of the undoped ZnO thin film samples deposited at different substrate temperatures and sputtering gas compositions.

Especially the two samples that were fabricated at 400 °C (UZO-05 and UZO-06) showed relatively intense and sharp peaks with respect to the samples fabricated at 200 °C and room temperature.

Table 5.8 shows the FWHM values corresponding to (002) peaks of undoped ZnO thin film samples.

Table 5.8. FWHM values of the (002) peaks of the undoped ZnO thin film samples.

Sample Name	UZO-1	UZO-2	UZO-3	UZO-4	UZO-5	UZO-6
FWHM	0,50°	0,44°	0,45°	0,63°	0,42°	0,42°

The (002) peaks of samples UZO-05 and UZO-06 were further inspected by rocking curve scans around half the Bragg peak at 2θ angle (17,2°). Rocking curves can hold detailed information about the gonio scan peaks such as any convoluted peaks and higher resolution look into the peak's breadth. Figure 5.19 shows the rocking curves of samples UZO-5 and UZO-06 which were deposited at 400 °C.

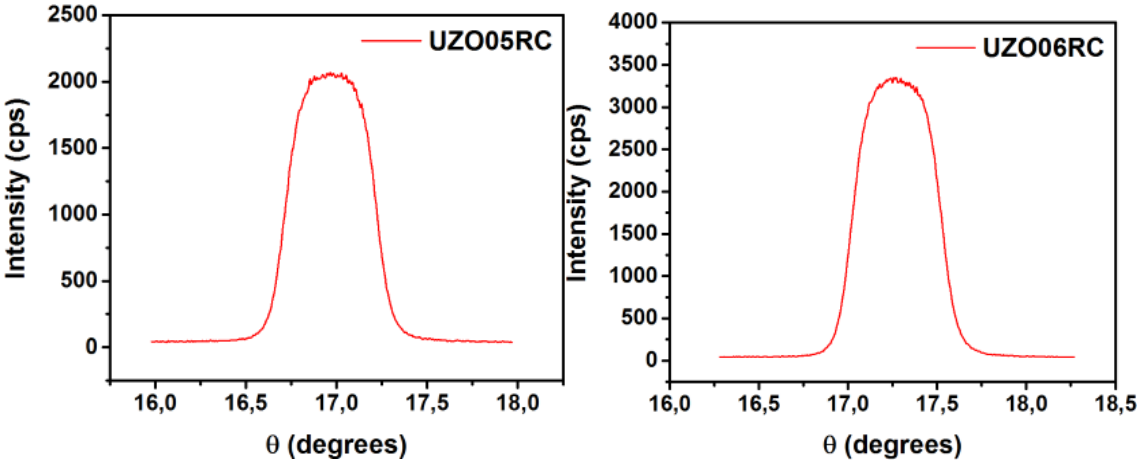

Figure 5.19. Rocking curve scans of the (002) peaks of samples UZO-05 and UZO-06.

The FWHM values of the Gaussian fits to the rocking curves of the samples were 0,45° for both samples. The bluntness and raggedness seen at the peaks is a measure of mosaicity, which is the degree of minor orientation deviations among the textured grains. The rocking curves suggest that the sample UZO-06 has slightly less mosaicity than UZO-05.

The mean crystallite size (D) of the (002) oriented grains was evaluated according to broadening of the highest intensity peak corresponding to (002) diffraction plane using the Debye-Scherrer relation shown below;

$$D = \frac{0{,}9\,\lambda}{\beta \cos\theta} \tag{5.4}$$

where, λ, β, and θ are the characteristic X-ray wavelength in Å, full width at half maximum (FWHM) of the peak and Bragg's angle in radians, respectively. Table 5.9 shows the mean crystallite sizes (D) of the (002) oriented grains of undoped ZnO thin film samples.

Table 5.9. Mean crystallite sizes (D) of the (002) oriented grains of the undoped ZnO thin film samples.

Sample Name	**UZO-1**	**UZO-2**	**UZO-3**	**UZO-4**	**UZO-5**	**UZO-6**
Mean Crystallite Size (D)	16,49 nm	18,74 nm	18,32 nm	13,09 nm	19,63 nm	19,63 nm

These results can be harnessed to modify grain sizes at elevated production or annealing temperatures to suppress XRD peak broadening. Moreover, epitaxial substrates such as sapphire can be used for ZnO growth to further improve the crystallinity of the thin films. This will lead to polycrystalline ZnO thin films with larger crystals having less grain boundaries and defects, which are known as natural defect formation, oxygen adsorption, electron and light scattering centers that degrade device performance in optoelectronic applications.

Finally, lattice strains induced in the thin films were calculated by the Scherrer formula below;

$$\varepsilon = \frac{\beta}{4\tan\theta} \tag{5.5}$$

where, ε, β, and θ are the lattice strain, full width at half maximum (FWHM) of the peak and Bragg's angle in radians, respectively. Table 5.10 shows the lattice strains in the undoped ZnO thin film samples.

Table 5.10. Lattice strains in the undoped ZnO thin film samples.

Sample Name	**UZO-1**	**UZO-2**	**UZO-3**	**UZO-4**	**UZO-5**	**UZO-6**
Lattice Strain	0,71%	0,62%	0,63%	0,89	0,59	0,59

5.8. I-V Measurements

Figure 5.20 shows the I-V measurement plots of undoped ZnO thin film sample UZO-02 and SiO_2 encapsulated sample UZO-02E fabricated on quartz substrates with the magnetron sputtering.

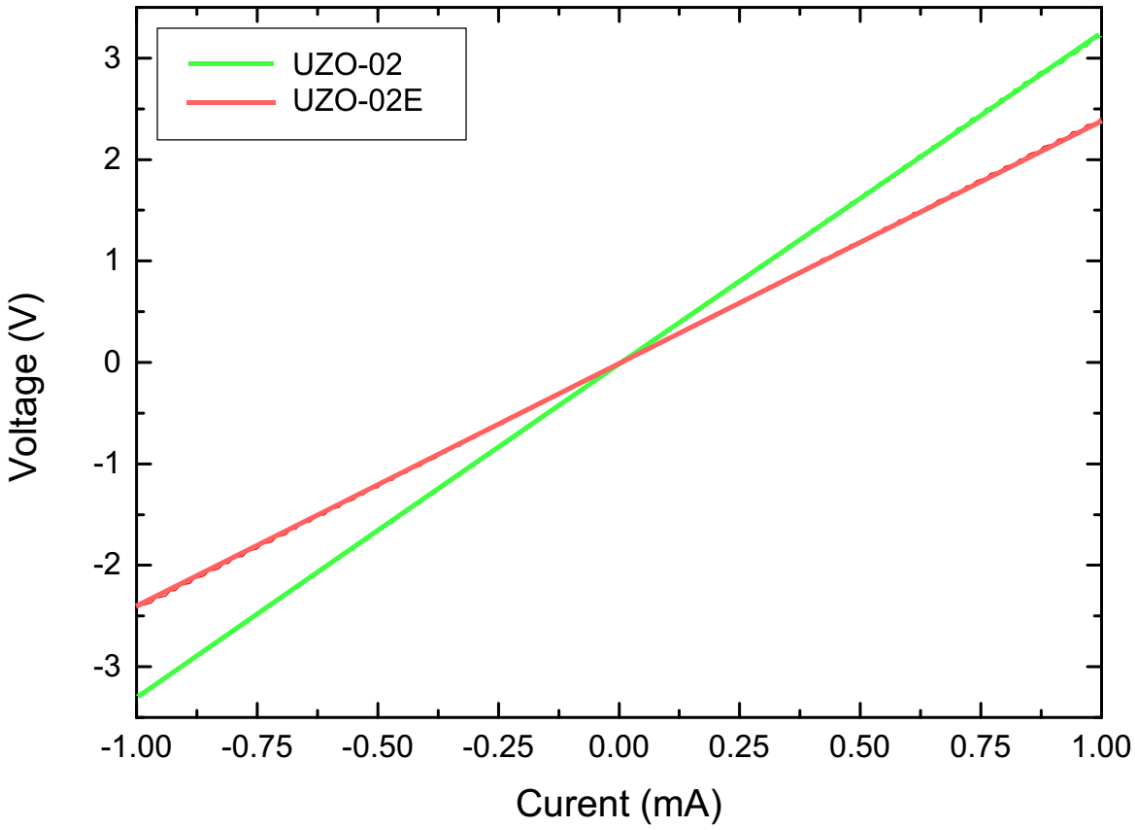

Figure 5.20. I-V plots of samples UZO-02 and UZO-02E.

I-V measurements revealed ohmic contacts for both samples. UZO-02 had a resistance of 3,2 kΩ whereas the SiO_2 encapsulated sample had a resistance of 2,3 kΩ.

The reduction in resistance values is attributed to the passivation effect of the encapsulation layer. This layer partially prevents atmospheric adsorbates such as O_2 and water vapor molecules to get physisorbed and/or chemisorbed onto the thin films' surface by depleting the free conduction electrons. Therefore, there is a decrease in the resistance value of the encapsulated films which has fewer adsorbates on them. Figure 5.21 illustrates this adsorption mediated depletion mechanism on the air-exposed surfaces of the ZnO thin films.

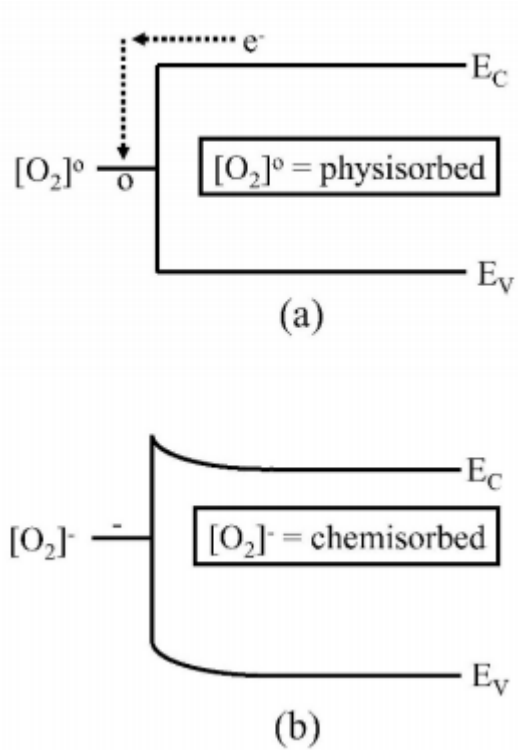

Figure 5.21. Air-exposed ZnO thin film layer depletion mechanism.

The adsorption of oxygen onto an n-type ZnO surface can be described in the context of acceptor-like surface state behavior. As indicated in Figure 5.21 (a), when molecular oxygen is physisorbed (weakly bonded) onto a ZnO surface, it is electrically neutral. However, if an electron from the ZnO conduction band is captured by the physisorbed molecular oxygen (dashed arrows of Figure 5.21 (b)) this electronic charge transfer process results in the formation of strong bonding (chemisorption) of the oxygen to the surface. This electron trapping process results in a depletion or loss of conduction band electrons from the ZnO surface. As a result, the chemisorbed oxygen is now negatively charged. Thus, physisorbed and chemisorbed surface oxygen constitute the empty and filled states, respectively, of an acceptor-like surface state.

In addition to that, observation of ohmic contacts in all n-type ZnO samples can be attributed to lower work function of the metal than the degenerately n-type doped ZnO semiconductor ($\Phi_M < \Phi_S$) resulting in an accumulation layer within the metal-semiconductor junction region.

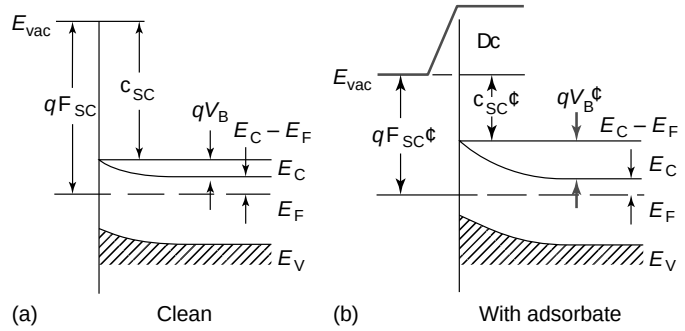

Figure 5.22. Schematic energy band diagram of (a) clean and (b) adsorbed semiconductor surface. With adsorption, both band bending and effective electron affinity change.

5.9. Transient Photocurrent Spectroscopy

Transient photocurrent spectroscopy measurements of undoped ZnO thin film sample UZO-02 and SiO_2 encapsulated sample UZO-02E were performed under 1 V bias. Prior to the measurements, the samples were brought under 10^{-3} Pa vacuum and irradiated under 254 nm (~ 4,9 eV) UV light for 3000 seconds to promote desorption of adsorbates. Variation of the photocurrent was determined as "normalized current" or photo-to-dark current ratio which is calculated as the ratio of the change in photocurrent to the dark current using the expression;

$$\left(\frac{\Delta I}{I_0}\right) = \left(\frac{I - I_0}{I_0}\right) \tag{5.6}$$

where I is the photocurrent and I_0 is the dark current.

Responsivity R is defined as the ratio of photo-to-dark current to the power of the illumination source P_λ and the effective area S_{eff} of the sensing element. It is represented in A/W.

$$R = \frac{I - I_0}{P_\lambda . S_{eff}} \tag{5.7}$$

The external quantum efficiency (*EQE)* is also a quantitatively assessed key figure of merit for a photo detector. It is defined as the ratio of responsivity to the wavelength λ of incident irradiation.

$$EQE = \frac{hc}{q\lambda} R \times 10^2\% \tag{5.8}$$

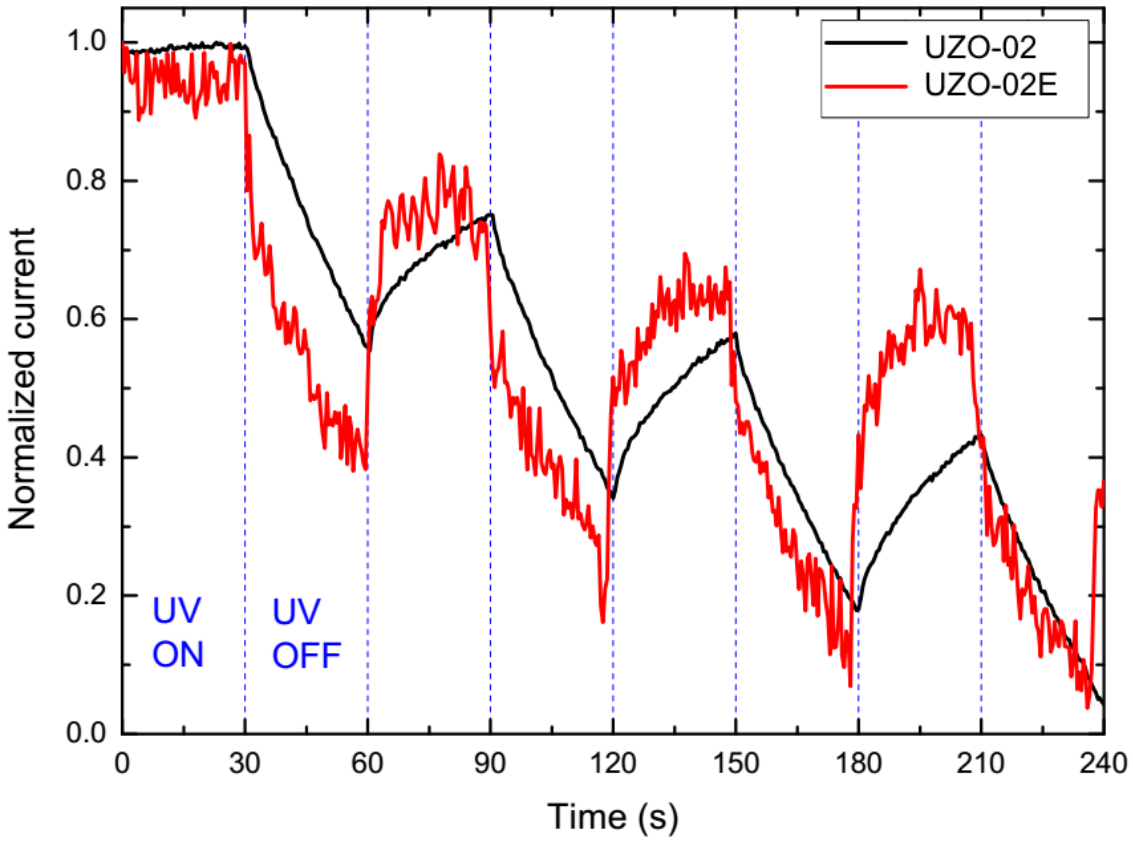

Figure 5.23. TPS plots of samples UZO-02 and UZO-02E.

Figure 5.23 shows the TPS response of samples UZO-02 and UZO-02E under UV light illumination with 30 s intervals.

It can clearly be seen that SiO_2 encapsulation effectively suppressed the adsorbate induced persistent photoconductivity in n-type ZnO thin film samples to some extent. The decreased photocurrent fluctuations between illumination cycles indicates significantly lower adsorption affecting the charge carrier concentration of the ZnO thin films via the electron trapping process explained before.

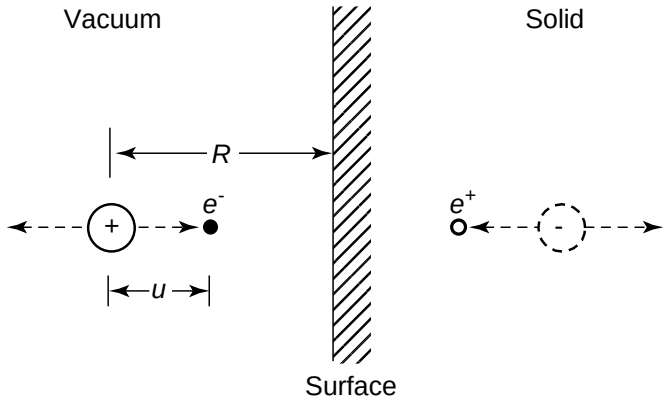

Figure 5.24. Schematic illustration of physisorbed atom consisting of a positive ion and valence electron and the resulting image charge formation in the solid.

But despite the improvement in the photo sensing capability of SiO_2 encapsulated device, the photoresponsivity is still largely mediated by photoelectrochemical reactions rather than electronic transitions between the semiconductor's valance and conduction bands. The unsaturated signal interval of 30 seconds is much higher than average electron-hole pair creation and recombination process times on the order of pico- to nanoseconds. For a sensor device to be classified as a solid-state photo detector, the response times must be much lower.

This non ideal behavior of n-type ZnO thin films has long been studied and is largely attributed to their polycrystalline nature. When binary oxides such as ZnO, In_2O_3, or SnO_2 are employed as active sensing materials in thin film form, they invariably are nanocrystalline. Such semiconductor materials with a high density of grain boundaries will function as poor sensing layers. Because these films will have inherently inferior charge carrier mobility relative to that observed in single crystals and epitaxial films because of the dominance of grain boundary inhibited transport.

Grain boundary transport in polycrystalline materials may be understood with the aid of an energy band diagram, such as the one given in Figure 5.25 for an n-type material, where electron transport is dominant.

The basic idea here is that a grain boundary can be treated as an internal surface that traps charge. If this trapped charge at the grain boundary is considered as a discrete acceptor trap with energy E_T, as shown in Figure 5.24, charge neutrality conditions indicate that negative charge trapped at the grain boundary, qN_{GB}, will be balanced by positive charge associated with donor doping, qN_D, in the depletion region surrounding

the grain boundary, thereby giving rise to an energy barrier, E_B. Thus, the boundary can be considered to be a back-to back Schottky barrier from an inter-grain transport perspective. As a result, electron transport between grains will be inhibited by the energy barrier indicated as E_B which will subsequently reduce the mobility of electrons within a grain that cannot surmount the inter-grain energy barrier.

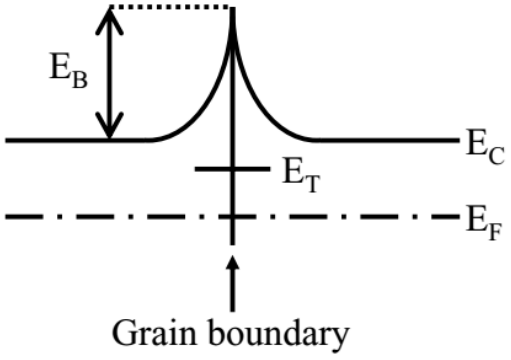

Figure 5.25. One-dimensional energy band diagram model for an n-type polycrystalline material.

Furthermore, the excess amount of grain boundaries constitutes preferential paths for atmospheric adsorbates such as oxygen to penetrate in the film, increasing the oxygen concentration in the film, which is reflected as higher resistivity (ρ) and lower charge carrier concentration (N). Moreover, this diffusion process promotes oxygen adsorption through the thin film and starts electron trapping processes that modulates the inter-grain boundary barrier height, aggravating the already severe implications of low charge carrier mobility (μ).

To overcome these shortcomings of nanocrystalline oxide semiconductors, Hosono et al. laid the theoretical foundations and proposed amorphous oxide semiconductors (AOSs). Amorphous materials are very attractive from a manufacturing point-of-view because their preparation can typically be accomplished at relatively low temperatures, they tend to have very smooth surfaces, which are advantageous for process integration, and they possess no grain boundaries and their associated pitfalls mention here previously.

With these structural and optical data in hand, the next sections will cover metal–semiconductor junction fabrication of the multi-component AOS indium-gallium-zinc oxide (a-IGZO) and optoelectronic characterization of fabricated devices by 4-point probe and transient photocurrent spectroscopy measurements.

5.10. a-IGZO Thin film Production Parameters

a-IGZO thin films were fabricated from IGZO 1:1:1 target on quartz substrates with the DC magnetron sputtering deposition parameters given in Table 5.11.

Table 5.11. Sputtering parameters for a-IGZO thin films.

Sample Name	Sputtering Power	Ar Flow Rate	Ar Pressure	Working Distance	Rotation Speed	Substrate Temperature
IGZO-1	**60 W**	2 SCCM	1.2 mTorr	107 mm	10 RPM	RT
IGZO-2	**60 W**	4 SCCM	2.1 mTorr	107 mm	10 RPM	RT
IGZO-3	**60 W**	6 SCCM	3.2 mTorr	107 mm	10 RPM	RT
IGZO-4	**60 W**	8 SCCM	4.1 mTorr	107 mm	10 RPM	RT

In this set of samples, a-IGZO thin films were deposited at increasing sputtering gas pressures while maintaining a fixed DC power level of 60 W along depositions.

5.10.1. Reactive Sputtering with Substrate Bias

To investigate the effects of substrate biasing, a-IGZO thin films were deposited with radio frequency (RF) bias power applied to the substrates in a reactive sputtering environment.

Table 5.12. Reactive sputtering parameters for a-IGZO thin films.

Sample Name	Sputtering Power	Ar Flow Rate	O_2 Flow Rate	Substrate Bias	Working Distance	Substrate Temperature
IGZO-5	**50 W**	3.5 SCCM	1.5 SCCM	5	107 mm	RT
IGZO-6	**50 W**	3.5 SCCM	1.5 SCCM	10	107 mm	RT
IGZO-7	**50 W**	3.5 SCCM	1.5 SCCM	15	107 mm	RT
IGZO-8	**50 W**	3.5 SCCM	2 SCCM	10	107 mm	RT
IGZO-9	**50 W**	3.5 SCCM	3 SCCM	10	107 mm	RT
IGZO-10	**50 W**	3.5 SCCM	4 SCCM	10	107 mm	RT

a-IGZO thin films were deposited from IGZO 1:1:1 target on quartz substrates with the DC magnetron sputtering deposition parameters given in Table 5.12. In this set of samples, oxygen gas was admitted into the chamber while applying RF power to facilitate the incorporation of atomic oxygen into the deposited films.

5.11. Thermal Treatment under Ultraviolet Irradiation

A thermal treatment at 160 °C for 1 hour was applied at ambient atmosphere under UV illumination to improve the optoelectronic properties of a-IGZO thin film samples. This process facilitates the rearrangement of elements in the as-deposited a-IGZO thin films as well as oxygenation of the thin film surface due to ozone formation during the process.

5.12. Hall Effect and I-V Measurements

Hall effect and I-V measurements of the a-IGZO thin film samples were conducted. Electronic properties of these thin films deposited under different sputtering gas flows and pressures were investigated. In these experiments, we wanted to examine the effects of sputtering gas flow rate and pressure on the resistivity, carrier concentration and mobility of the thin films.

5.12.1. Hall Effect Measurements

The measurement results were presented in four main groups differentiated by the sputtering pressure of the samples in the groups. The sample in the each group was deposited at 60 W DC power.

In each aforementioned group, a-IGZO thin films were deposited at four different sputtering gas flow rates with their corresponding pressures. And in each of these sub-groups, samples were deposited for 100 minutes.

Table 5.13 summarizes the electronic properties of all samples probed via van der Pauw method.

Table 5.13. Comparative list of electronic properties of a-IGZO thin films

Sample Name	Substrate Temperature (°C)	Sheet Resistance (Ω/□)	Carrier Concentration (cm^{-3})	Hall Mobility ($cm^2/V.s$)
IGZO-1	RT	1250	$4x10^{17}$	3
IGZO-2	RT	980	$6x10^{18}$	2,3
IGZO-3	RT	755	$7x10^{18}$	1,4
IGZO-4	RT	530	$2x10^{19}$	1,1

Sheet resistance values of the samples decrease with increasing Ar flow rate and sputtering pressure. Carrier densities of the films increase in accordance with decreasing sheet resistance which is proportional in the conductivity relation. Contrary to increasing conductivity values, Hall mobilities decrease with increasing carrier concentrations. This is attributed to increasing number of electron-electron scattering interactions due to increased carrier numbers. Compared to ZnO thin film samples, a-IGZO has much superior Hall mobility values owing to its inherent amorphous structure and conduction mechanism mentioned previously.

5.12.2. I-V Measurements

I-V relations of the a-IGZO thin film samples were extracted by scanning -1 to +1 V voltage range with 50 mV intervals. Aluminum contact pads were deposited on the corners of all samples in the van der Pauw geometry to conduct measurements. A specially designed van der Pauw (vdP) probe head was used to apply voltages and measure corresponding currents on the samples. The probe head unit is comprised of a PCB with 4 spring-loaded pins arranged in the vdP geometry. These pins are connected to the SMUs by connector slot-plug assemblies. Figure 5.26 shows the probe head PCB and one of the thin films samples investigated by this assembly.

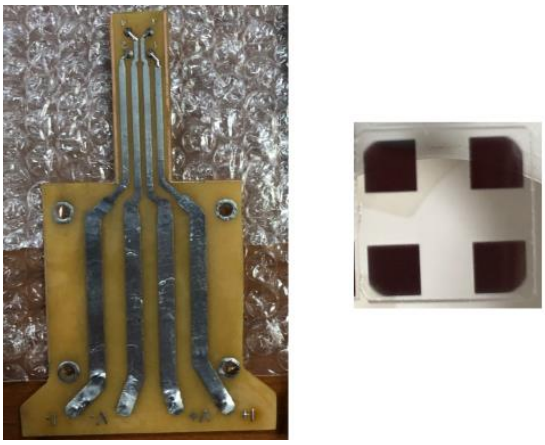

Figure 5.26. The van der Pauw probe head for electronic measurements along with an a-IGZO thin film on quartz substrate with aluminum electrodes in the corners

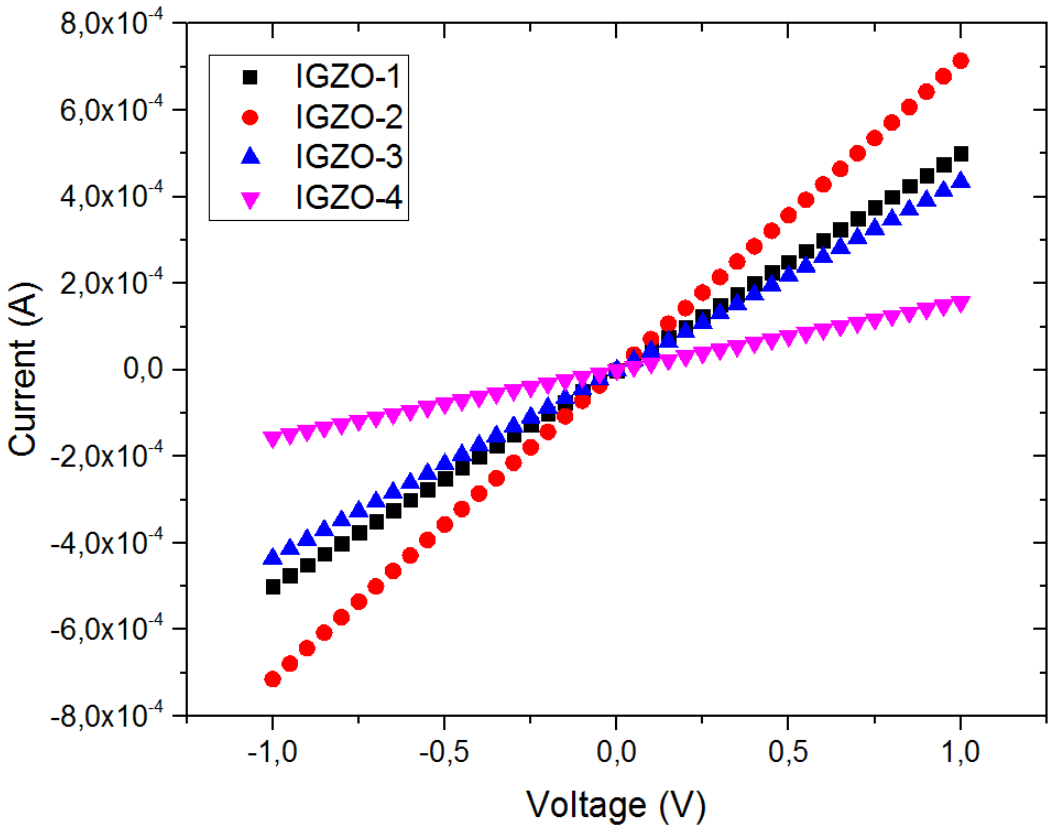

Figure 5.27. I-V plots of a-IGZO thin film samples

a-IGZO thin films exhibited linear (ohmic) I-V behaviors. The slope of the I-V line tended to decrease with increasing sputtering pressure with the exception of IGZO-1 sample. This discrepancy can be attributed to uneven contact with the metallic

electrodes deposited on the film or uneven contact pressure of the probing pins touching the metallic electrodes. In each case, the deviation is in the acceptable error margins.

5.13. Transient Photocurrent Spectroscopy

Figure 5.28 and Figure 5.29 shows TPS data for samples IGZO-1 and IGZO-2 respectively.

The IGZO-1 sample had significantly improved response times with respect to the ZnO based samples covered in the previous sections. The sample had 59 sec. rise time under 250 mW 254 nm UV light irradiation. The fall time of the sensor was recorded approximately 50 sec. which is also a great improvement over the ZnO samples. These enhancements on the rise-fall times of the a-IGZO based devices can be attributed to the lack of negative impacts of the polycrystalline nature of ZnO elaborated earlier.

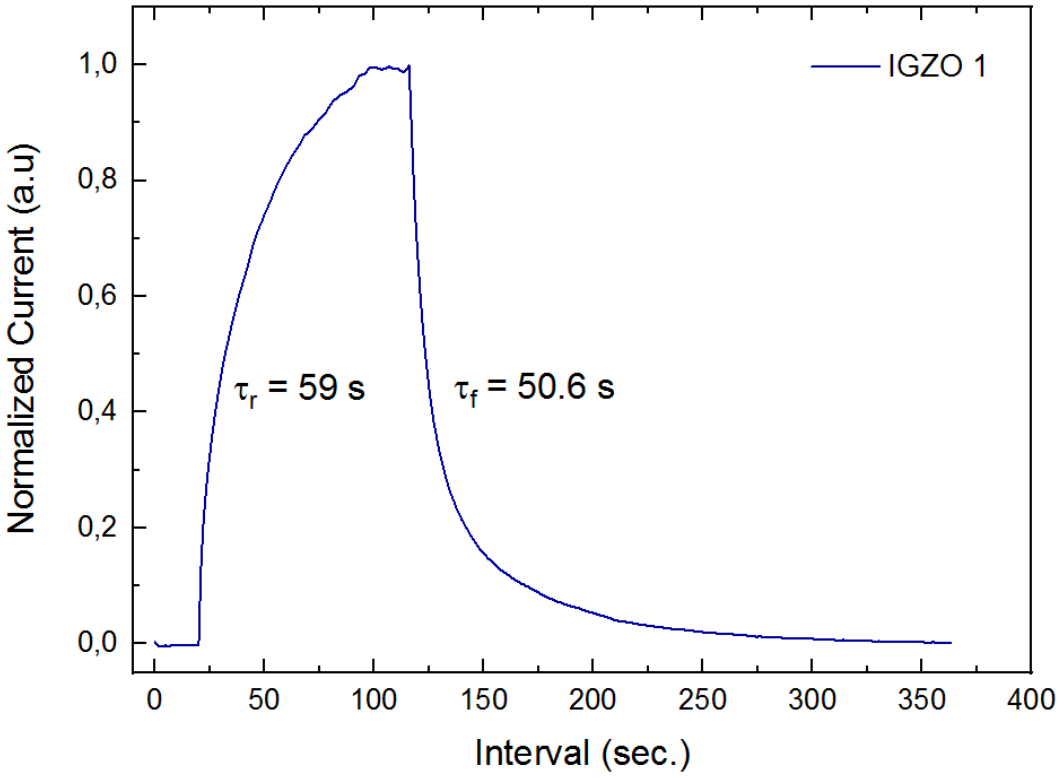

Figure 5.28. TPS plot of a-IGZO-1. The sample had a rise and fall time of 59 and 50.6 seconds respectively.

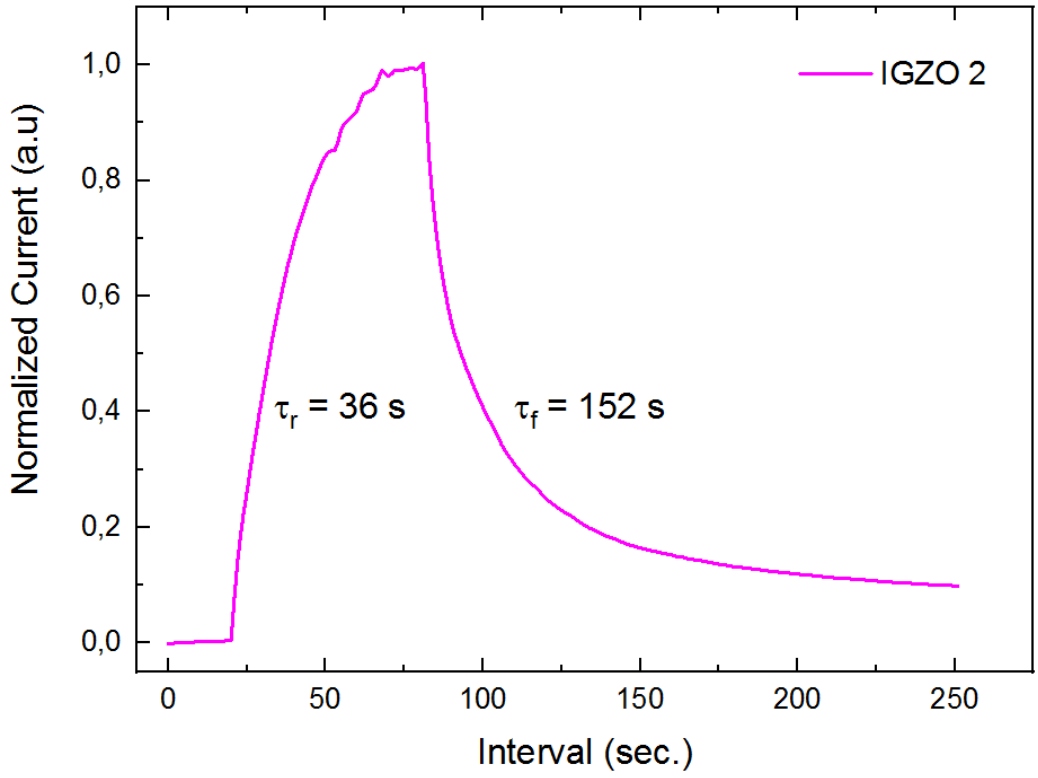

Figure 5.29. TPS plot of a-IGZO-2. The sample had a rise and fall time of 36 and 152 seconds respectively.

Again, there has been a significant improvement in response time for the IGZO-2 sample. This device had a nearly 25% lower rise time than the IGZO-1 device. But it had a nearly 3-times longer fall time with respect to the IGZO-1 device. By looking at the Hall effect measurement results, it can be inferred that the higher carrier concentration and lower mobility of this sample could be effective in the recombination process. The electron-hole pairs created under UV illumination which contributed the photocurrent recombines when the UV illumination is turned off. A higher trap density along with a higher carrier concentration may affect this recombination process by hindering the process by electron-electron scattering lowering the mean free path of carriers during the recombination process.

The IGZO-6 sample deposited under 10 W RF bias had significantly improved response times with respect to the unbiased samples covered in the previous sections. The sample had 14 sec. rise time under 500 mW 275 nm UV light irradiation. The fall time of the sensor was recorded approximately 9.4 sec. which is also a great improvement over the unbiased samples. These enhancements on the rise-fall times of the a-IGZO based devices can be attributed to reactive conditions and the gettering effect of RF biasing during depositions.

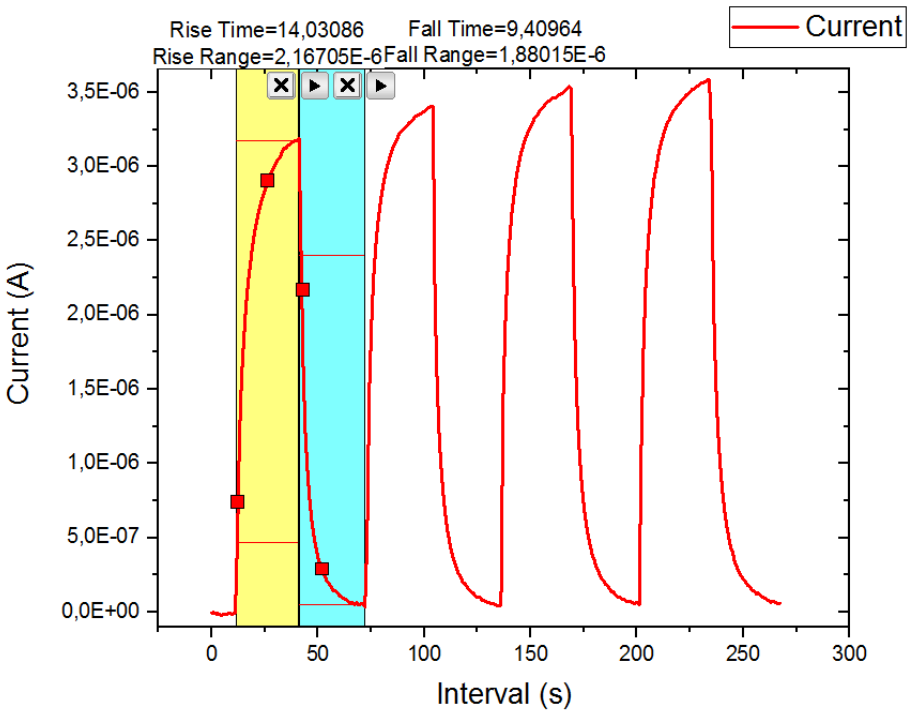

Figure 5.30. TPS plot of a-IGZO-6. The sample had a rise and fall time of 14 and 9.4 seconds respectively.

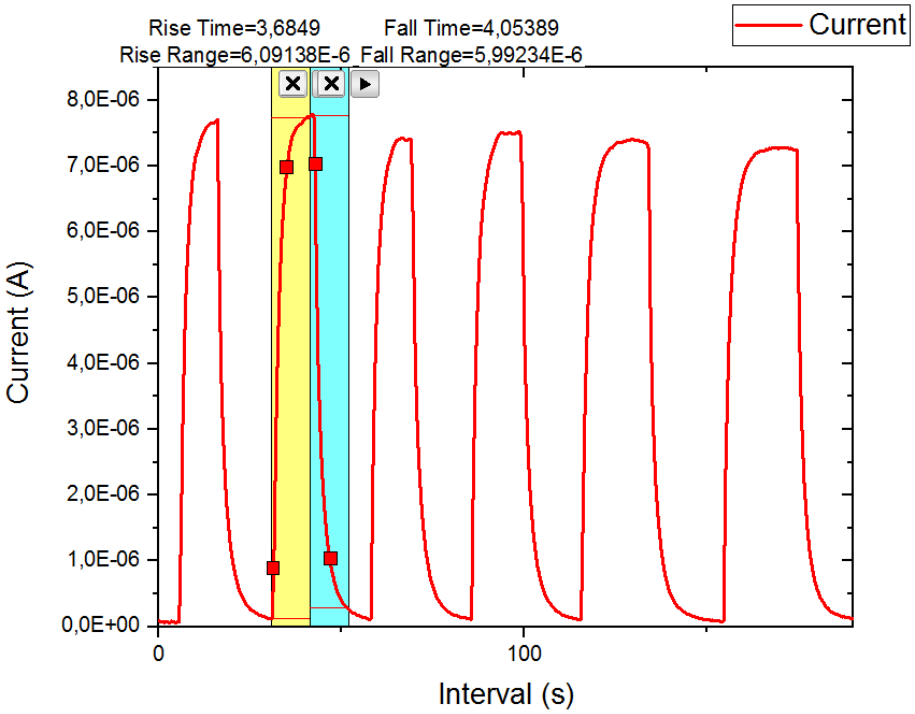

Figure 5.31. TPS plot of a-IGZO-8. The sample had a rise and fall time of 3.7 and 4 seconds respectively.

The IGZO-8 sample which was also deposited under 10 W RF bias was thermal treated under UV irradiation. It had improved response times with respect to the untreated samples. The sample achieved a rise time of 3.7 sec. under 500 mW 275 nm UV light irradiation. The fall time of the sensor was recorded approximately 4 sec. which is also a great improvement over the untreated samples. These enhancements on the rise-fall times of the a-IGZO based devices can be attributed to the rearrangement of elements in the as-deposited a-IGZO thin films as well as oxygenation of the thin film surface due to ozone formation during the process.

The IGZO-9 sample which was deposited under 3 SCCM oxygen flow had further reduced rise and fall times of 1.7 and 2.1 seconds, respectively. This indicates that the oxygen deficiency in the deposited films was further reduced by increasing oxygen flow rate under RF bias conditions. IGZO-9 attained a dark current of 54 nA and reached a photocurrent level of 2.5 µA with a photo-to-dark current ratio of 45, yielding a spectral response of 1223 A/W. The calculated external quantum efficiency for this device was 550000%.

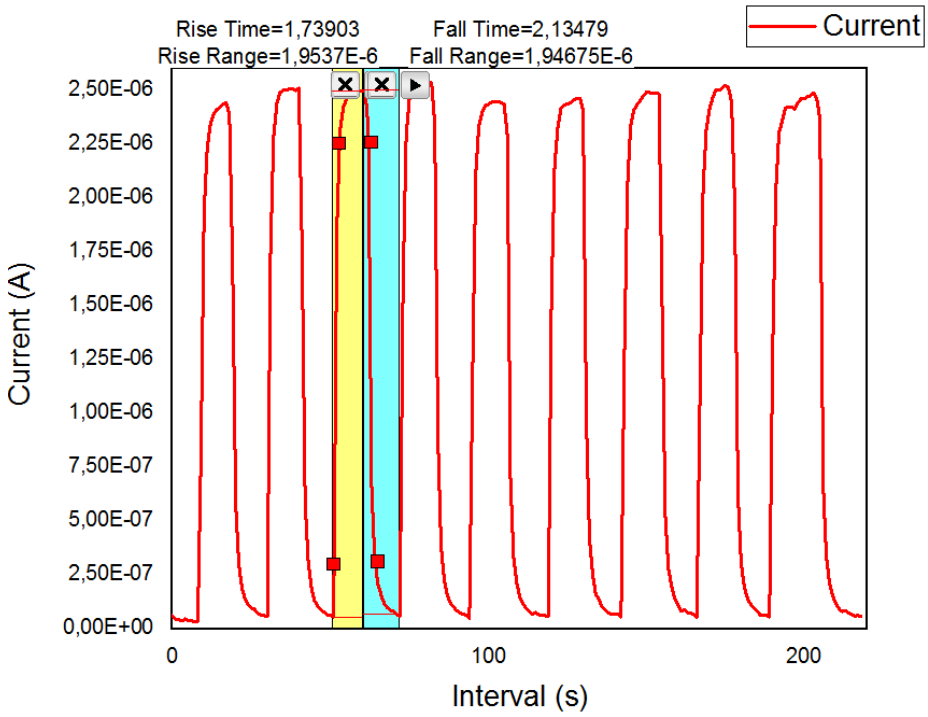

Figure 5.32. TPS plot of a-IGZO-9. The sample had a rise and fall time of 1.7 and 2.1 seconds respectively.

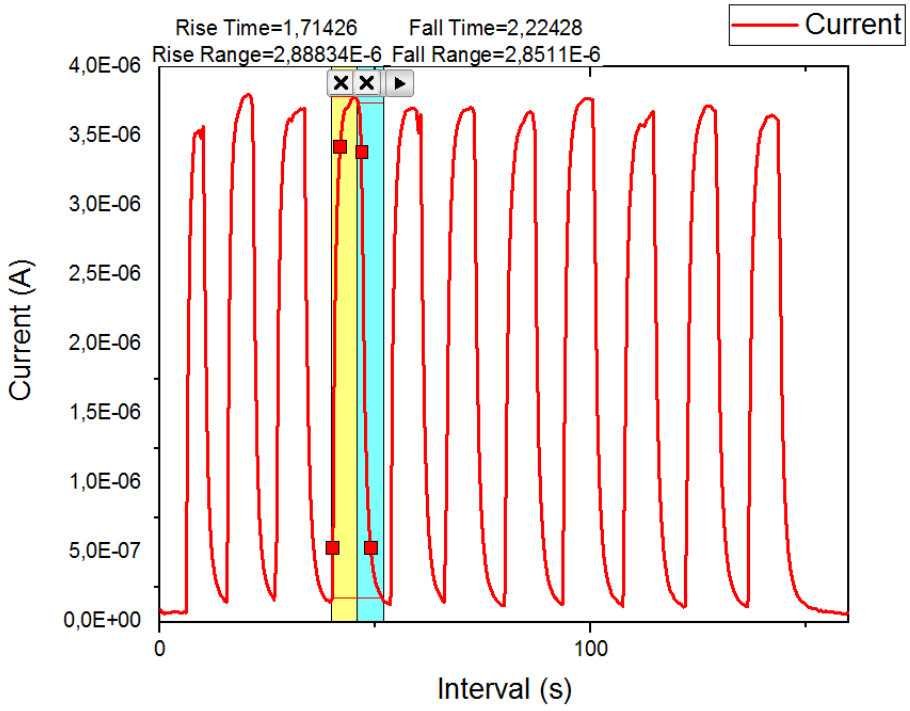

Figure 5.33. TPS plot of a-IGZO-10. The sample had a rise and fall time of 1.7 and 2.2 seconds respectively.

Finally, the IGZO-10 sample which was deposited under 4 SCCM oxygen flow had similar rise and fall times of 1.7 and 2.2 seconds as IGZO-9, respectively. But IGZO-10 attained a dark current of 140 nA and reached a photocurrent level of 3.8 µA with a photo-to-dark current ratio of 45, yielding a spectral response of 1830 A/W. The calculated external quantum efficiency for this device was 825000%.

CHAPTER 6

CONCLUSIONS

This thesis is focused on optimization of zinc oxide based metal - semiconductor junction interface properties and applications for optoelectronic devices. During the experimental stages, pristine, Al-doped and amorphous ZnO-based thin-films were deposited via RF and DC magnetron sputtering method on substrates decorated with metallic electrodes. The ZnO–metal junction interface was optimized by altering sputtering parameters, such as gas pressure, power, target-substrate distance and temperature at different thin film depositions. ZnO thin-film surfaces were passivated in-situ with inert dielectric encapsulation layers in order to isolate ZnO from ambient atmosphere to overcome the persistent photoconductivity effect. Structural, spectroscopic and electrical surveys were conducted to assess optimal film thickness, dopant amount and optoelectronic properties of the metal–ZnO thin-film interface to take advantage of the unique properties of the metal-semiconductor junction formed between metallic electrodes and ZnO. To determine the effects of energetic ion bombardment on the films' surface properties, biases ranging from 5 to 15 W were applied to the substrates during depositions. Furthermore, a thermal treatment under ultraviolet irradiation and was applied specifically to amorphous In-Ga-Zn-O thin films after device fabrication to improve their ultraviolet sensing capabilities

The intrinsic ZnO thin film produced at 50 W showed smooth and intact surfaces even at relatively high magnifications whereas the intrinsic ZnO thin film produced at 100 W showed coarsely grained and highly defective surfaces even at low magnifications. This observation revealed that at higher sputtering power film morphology tends to be more defective. EDX spectra showed nearly stoichiometric ZnO compositions for both thin films produced at 50 W and 100 W.

XRD analysis of the ZnO thin films revealed a highly (0002) oriented wurtzite ZnO crystal structure with a single strong reflection at 2θ angle of 34,3° for both films deposited at 50 W and 100 W. The Gaussian fits of the 2θ reflection peaks of the ZnO thin films deposited at 50 W and 100 W had a FWHM of 0,5933 and 0,6211 degrees, respectively. This indicated that the ZnO thin films are polycrystalline in nature and the crystallinity was found to be improved at the lower sputtering power of 50 W.

Step measurements via AFM between the ZnO thin film and substrate surface were made from different sharply masked sites on the surface of the film. The average thickness values of the ZnO thin films produced at 50 W (BZO 1) and 100 W (BZO 2) were found to be approximately 110 nm and 220 nm, respectively. Deposition time being taken constant for the two samples at 100 minutes, a linear correlation was found between sputtering power and resulting film thickness.

Optical bandgap energies of the undoped ZnO thin film samples were determined from Tauc plots extracted from UV-Vis measurements. Average optical bandgap values of the undoped ZnO thin film samples were about 3,26 eV which is consistent with single crystal data.

For the excitation energy of ~3,54 eV (350 nm) slightly above the ~3,36 eV (~370 nm) typical bandgap of ZnO, the photoluminescence spectra of the thin film samples fabricated with Ar–O_2 mixture (UZO-02, UZO-03, UZO-05) showed near-band emissions at 390 nm, 393 nm, and 392 nm, respectively. Whereas, the samples fabricated with pure Ar (UZO-01, UZO-04, UZO-06) showed emissions around 400 nm, 404 nm, and 404 nm, respectively. These observations in the photoluminescence spectra of the fabricated ZnO thin films indicate that, all of the samples contain defect states such as; V_0^*, Zn_i, O_i, V_{Zn} , and O_{Zn} to some extent. And those defects can be manipulated by varying the fabrication parameters during thin film deposition and post-processing.

I-V measurements revealed ohmic contacts for both samples. UZO-02 had a resistance of 3,2 kΩ whereas the SiO_2 encapsulated sample had a resistance of 2,3 kΩ. The reduction in resistance values is attributed to the passivation effect of the encapsulation layer. This layer partially prevents atmospheric adsorbates such as O_2 and water vapor molecules to get physisorbed and/or chemisorbed onto the thin films' surface by depleting the free conduction electrons. Therefore, there is a decrease in the resistance value of the encapsulated films which has fewer adsorbates on them.

Transient photocurrent spectroscopy measurements of undoped ZnO thin film sample UZO-02 and SiO_2 encapsulated sample UZO-02E under 1 V bias showed that SiO_2 encapsulation effectively suppressed the adsorbate induced persistent photoconductivity in n-type ZnO thin film samples to some extent. The decreased photocurrent fluctuations between illumination cycles indicates significantly lower adsorption affecting the charge carrier concentration of the ZnO thin films via the electron trapping process explained before.

According to conducted literature surveys and the aforementioned brief of relevant literature on AOSs and specifically a-IGZO, thin films from IGZO (1:1:1) at % were fabricated to suppress persistent photoconductivity effect.

a-IGZO thin films exhibited linear (ohmic) I-V behaviors. The slope of the I-V line tended to decrease with increasing sputtering pressure with the exception of IGZO-1 sample.

The IGZO-1 sample had significantly improved response times with respect to the ZnO based samples covered in the previous sections. The sample had 59 sec. rise time under 250 mW 254 nm UV light irradiation. The fall time of the sensor was recorded approximately 50 sec. which is also a great improvement over the ZnO samples. There has been a significant improvement in response time for the IGZO-2 sample. This device had a nearly 25% lower rise time than the IGZO-1 device. These enhancements on the rise-fall times of the a-IGZO based devices can be attributed to the lack of negative impacts of the polycrystalline nature of ZnO elaborated earlier.

The IGZO-6 sample deposited under 10 W RF bias had significantly improved response times with respect to the unbiased samples. Samples IGZO-8, IGZO-9 and IGZO-10 had steady improvements in their photo detection capabilities with increasing oxygen flows during depositions.

To summarize, a-IGZO offers favorable features such as high mobility, high uniformity, low process temperature, a wide flexibility of chemical composition, good controllability of carrier density, and transparency. Its lack of grain boundaries, which is the main issue with ZnO, dense and homogeneous structure, smooth surface, room temperature deposition and thermal stability at elevated temperatures makes a-IGZO an outstanding material to work with to characterize metal-semiconductor junction formations and their related optoelectronic properties. As a result, it is possible to utilize this material as a more robust and functional candidate instead of ZnO for general purpose photodetector devices.

REFERENCES

Ahn K.S., Y. Yan, M Al-Jassim. 2007. "Band gap narrowing of ZnO:N films by varying rf sputtering power in O2/N2 mixtures", *Journal of Vacuum Science & Technology*, B25, pp. 23-26.

Akazawa H., 2009. "Highly conductive, undoped ZnO thin films deposited by electron-cyclotron-resonance plasma sputtering on silica glass substrate", *Thin Solid Films*, 518, pp. 22–26.

Ali A., P. Morrow, R. Henda, R. Fagerberg. 2016. "Deposition of Cobalt Doped Zinc Oxide Thin Film Nano-Composites Via Pulsed Electron Beam Ablation", *MRS Advances*, 1, 06, pp. 433-439.

Chen Y., P. I. Reyes, Z. Duan. 2009. "Multifunctional ZnO-Based Thin-Film Bulk Acoustic Resonator for Biosensors", *Journal of Electronic Materials*, 38, 8, pp. 1605–1611.

Djurisic A. B., X. Chen, Y. H. Leung. 2012. "ZnO nanostructures: growth, properties and applications", *Journal of Materials Chemistry*, 22, 6526.

Djurisic A. B., Y. H. Leung. 2006, "Optical Properties of ZnO Nanostructures", *Small*, 2, No.8-9, 944–961.

Doyan A., Susilawati, S. A. Fitri, S. Azhan. 2017. "Crystal structure characterization of thin layer zinc oxide", 2017, *IOP Conf. Ser.: Mater. Sci. En.*, 196, 012004.

Eda G., M. Chhowalla. 2010. "Chemically Derived Graphene Oxide: Towards Large-Area Thin-Film Electronics and Optoelectronics", *Advanced Materials*, 22, pp. 2392-2415.

Gautam U., M. Imura, C. S. Rout. 2010. "Unipolar assembly of zinc oxide rods manifesting polarity-driven collective luminescence ", *PNAS*, 107, pp. 13588–13592.

Hosono H. 2018, "How we made the IGZO transistor", *Nature Electronics*, 1, 428.

Hosono H., N. Kikuchi, N. Ueda, H. Kawazoe. 1996, "Working hypothesis to explore novel wide band gap electrically conducting amorphous oxides and examples", *Journal of Non-Crystalline Solids*, 198:200.

Ide K., K. Nomura, H. Hosono, T. Kamiya. 2019. "Electronic Defects in Amorphous Oxide Semiconductors: A Review", *Physica Status Solidi A*, 216, pp. 1800372–28.

Ide K., K. Nomura, M. Orita, M. Hirano, K. Ueda, T. Suzuki, Y. Ikuhara, H. Hosono. 2003. “Single-Crystalline Films of the Homologous Series $InGaO_3(ZnO)_m$ Grown by Reactive Solid-Phase Epitaxy”, *Advanced Functional Materials*, 13, 2, 139–144.

Kamiya T., K.Nomura, H. Hosono. 2010. “Present status of amorphous In–Ga–Zn–O thin-film transistors”, *Science and Technology of Advanced Materials*, 11, 044305, 23 pp.

Khokhra R., B. Bharti1, H. Lee, R. Kumar. 2017, “Visible and UV photo-detection in ZnO nanostructured thin films via simple tuning of solution method”, *Scientific Reports*, 7:15032.

Kim B. J., C. Lee, M. A. Mastro. 2012. "Buried graphene electrodes on GaN-based ultra-violet light-emitting diodes", *Applied Physics Letters*, 101, pp. 1-4.

Kim B. J., C. Lee, Y. Jung. 2011. "Large-area transparent conductive few-layer graphene electrode in GaN-based ultra-violet light-emitting diodes", *Applied Physics Letters*, 99, pp. 1-3.

Klein A. 2012. "Energy band alignment at interfaces of semiconducting oxides: A review of experimental determination using photoelectron spectroscopy and comparison with theoretical predictions by the electron affinity rule, charge neutrality levels, and the common anion rule", *Thin Solid Films*, 520, pp. 3721–3728.

Lavrov E. V. 2009. "Hydrogen in ZnO", *Physica B*, 404, pp. 5075–5079.

Li X., B. Keyes, S. Asher. 2005. "Hydrogen passivation effect in nitrogen-doped ZnO thin films", *Applied Physics Letters*, 86, pp. 86-90.

Liu K., M. Sakurai, M. Aono. 2010. "ZnO-Based Ultraviolet Photodetectors", *Sensors*, 10, pp. 8604-35.

Liu M., H. K. Kim. 2004. " Ultraviolet detection with ultrathin ZnO epitaxial films treated with oxygen plasma", *Applied Physics Letters*, 84, pp. 173–175.

Lynch D. M., B.Zhu, D. A. Levin. D. A. Muller, R. G. Greene, M. O. Thompson. 2014. “Characterization of reactively sputtered c-axis aligned nanocrystalline $InGaZnO_4$”, *Applied Physics Letters*, 105, 262103-4.

Masuoka F., K. Ooba, H. Sasaki. 2006. " Applicability of ZnO single crystals for ultraviolet sensors", *Phys. Stat. Sol. (c)*, 4, pp. 1238–1241.

McCluskey M. D. and S. J. Jokela. 2009. "Defects in ZnO", *Journal of Applied Physics*", 106, pp. 1-10.

Moazzami K., T. E. Murphy, J. D. Phillips. 2006. " Sub-bandgap photoconductivity in ZnO epilayers and extraction of trap density spectra", *Semiconductor Science and Technology*, 21, pp. 717-723.

Muchuweni E., T. S. Sathiaraj, H. Nyakotyo. 2017. "Synthesis and characterization of zinc oxide thin films for optoelectronic applications", *Heliyon*, 3, Art. Nr. e00285.

Nistor M. 2012. "Doped Zinc Oxide Thin Films as Transparent Conductive Electrodes", *Romanian Reports in Physics*, 64, pp. 1313–1322.

Nistor M., N. B. Mandache, J. Perriere. 2008. "Pulsed electron beam deposition of oxide thin films", *Journal of Physics D: Applied Physics*, 41, pp. 1-11pp.

Nomura K., H. Ohta, A. Takagi, T. Kamiya, M. Hirano, H. Hosono. 2004, "Room-temperature fabrication of transparent flexible thin-film transistors using amorphous oxide semiconductors", *Nature*, 432, 488–492.

Nomura K., H. Ohta, K. Ueda, M. Orita, M. Hirano, H. Hosono. 2002. "Novel film growth technique for single crystalline $In_2O_3(ZnO)_m$ (m=integer) homologous compound". *Thin Solid Films*, 411:147–51.

Nomura K., H. Ohta, K. Ueda, T. Kamiya, M. Hirano, H. Hosono. 2003, "Thin-Film Transistor Fabricated in Single-Crystalline Transparent Oxide Semiconductor", *Science*, 300, 2169-2171.

Nomura K., H. Ohta, K. Ueda, T. Kamiya, M. Hirano, H. Hosono. 2004. "Growth mechanism for single-crystalline thin film of $InGaO_3(ZnO)_5$ by reactive solid-phase epitaxy", *Journal of Applied Physics*, 95, 10, 5532–5539.

Özgür Ü., Y. I. Alivov, C. Liu, A. Teke. 2005. "A comprehensive review of ZnO materials and devices", *Journal of Applied Physics*, 98, 1-103.

Pattini F., F. Annoni, F. Bissoli. 2015. "Comparative study about Al-doped zinc oxide thin films deposited by Pulsed Electron Deposition and Radio Frequency Magnetron Sputtering as Transparent Conductive Oxide for Cu(In,Ga)Se2-based solar cells", *Thin Solid Films*, 582, p. 317–322.

Quang P. H., N. D. Sang, D. Q. Ngoc. 2012. "Pulsed electron beam deposition of transparent conducting Al-doped ZnO films", Thin Solid Films, 520, pp. 6455–6458.

Rajendiran S., A.K. Rossall, A. Gibson, E. Wagenaars. 2014. "Modelling of laser ablation and reactive oxygen plasmas for pulsed laser deposition of zinc oxide", *Surface & Coatings Technology*, 260, pp. 417–423.

Rana A. K., Y. Kumar, N. Saxena. 2015, "Studies on the control of ZnO nanostructures by wet chemical method and plausible mechanism", *AIP Advances*, 5, 097118.

Ren Y., C. Zhu. 2012. "An Improved Method for Transferring Graphene Grown by Chemical Vapor Deposition", *NANO: Brief Reports and Reviews*, 7, pp. 1-6.

Schmidt O., P. Kiesel, C. G. van de Walle. 2005. “Effects of an Electrically Conducting Layer at the Zinc Oxide Surface”, *Japanese Journal of Applied Physics*, 44, pp. 7271-7274.

Seeman, J.M. 1966. "Bias sputtering: its techniques and applications". *Vacuum*, 3, Vol. 17, 129-137.

Serhane R., S. Abdelli-Messaci, S. Lafane. 2014. "Pulsed laser deposition of piezoelectric ZnO thin films for bulk acoustic wave devices", *Applied Surface Science*, 288, pp. 572–578.

Sheng J., T. H. Hong, H. M.Lee, K. R. Kim, M. Sasase, J. Kim, H. Hosono, J. S. Park. 2019. “Amorphous IGZO TFT with High Mobility of ~70 cm^2/Vs via Vertical Dimension Control using PEALD”, *ACS Applied Materials & Interfaces*, DOI: 10.1021/acsami.9b14310, 34 pp.

Shi, J., Zhang, J., Yang, L., Qu, M., Qi, D., Zhang, K.H.L. 2021. "Wide Bandgap Oxide Semiconductors: from Materials Physics to Optoelectronic Devices". *Advanced Materials*, 2006230, 33, 1-30.

Solookinejad G., A. S. H. Rozatian, M. H. Habibi. 2016. "Zinc Oxide Thin Films Characterization, AFM, XRD and X-ray Reflectivity", *Experimental Techniques*, 40, 4, pp. 1297–1306.

Tak, Y.J., Ahn, B.D., Park, S.P., Kim, S.J., Song, A.R., Chung, K., Kim, H.J. 2016. "Activation of sputter-processed indium–gallium–zinc oxide films by simultaneous ultraviolet and thermal treatments". *Scientific Reports*, 21869, 6, 1-11.

Tekcan B., C. Ozgit-Akgun, S. Bolat. 2014. "Metal-semiconductor-metal ultraviolet photodetectors based on gallium nitride grown by atomic layer deposition at low temperatures", *Optical Engineering*, 53, pp.10.

Tian C., D. Jiang, B. Li, J. Lin. 2014, “Performance Enhancement of ZnO UV Photodetectors by Surface Plasmons”, *ACS Applied Materials & Interfaces*, 6, 2162–2166.

Tricot S., C. B. Leborgne, M. Nistor. 2008. "Dynamics of a pulsed-electron beam induced plasma: application to the growth of zinc oxide thin films", *Journal of Physics D: Applied Physics*, 41, pp. 1-10.

Van der Pauw L. J. 1958. "A Method of Measuring Specific Resistivity and Hall Effect of Discs of Arbitrary Shape", *Philips Research Reports*, 13, pp. 1-9.

Van der Pauw L. J. 1958. "A Method of Measuring the Resistivity and Hall Coefficient on Lamellae of Arbitrary Shape", *Philips Technical Review*, 20, pp. 220-224.

Viezbicke B. D., S. Patel, B. E. Davis. 2015. "Evaluation of the Tauc method for optical absorption edge determination: ZnO thin films as a model system", *Phys. Status Solidi B*, 252, pp. 1700-1710.

Yarmolich D., P. Nozar, S. Gleizer. 2011. "Characterization of Deposited Films and the Electron Beam Generated in the Pulsed Plasma Deposition Gun", *Japanese Journal of Applied Physics*, 50, pp. 1-5.

Zhan P., Z. Li, Z. Zhang. 2011. "Preparation of Highly Textured ZnO Thin Films by Pulsed Electron Deposition", *Materials Transactions*, 52, pp. 1764-1767.

Zhang H., A. V. Babichev, G. Jacopin. 2013. "Characterization and modeling of a ZnO nanowire ultraviolet photodetector with graphene transparent contact", *Journal of Applied Physics*, 114, pp. 1-9.

Zhong H., K. Xu, Z. Liu. 2014. "Charge transport mechanisms of graphene/semiconductor Schottky barriers: A theoretical and experimental study", *Journal of Applied Physics*, 115, pp. 1-6.

Zhou J., Y. Gu, Y. Hu. 2009. “Gigantic enhancement in response and reset time of ZnO UV nanosensors by utilizing Schottky contact and surface functionalization”, *Applied Physics Letters*, 94, pp. 191103-1-3.

Znaidi L., T. Touam, D. Vrel. 2013. "AZO Thin Films by Sol-Gel Process for Integrated Optics", *Coatings*, 3, pp. 126–139.

VITA

Abdurrahman Halis GÜZELAYDIN

EDUCATION

2024, Ph.D. in Materials Science and Engineering, Graduate School of Engineering and Sciences, İzmir Institute of Technology, İzmir / Turkey
Thesis Title: Optimization of Zinc Oxide Based Metal - Semiconductor Junction Interface Properties and Applications for Optoelectronic Devices
Supervisor: Doç. Dr. Enver Tarhan

2014, M.Sc. in Materials Science and Engineering, Graduate School of Engineering and Sciences, İzmir Institute of Technology, İzmir / Turkey
Thesis Title: Investigation of Gas Sensing Properties of Nanoparticles Functionalized with Ferrocene Molecules
Supervisor: Prof. Dr. Salih Okur

2010, B.Sc. in Metallurgical and Materials Engineering, Faculty of Engineering, Dokuz Eylül University, İzmir / Turkey